Modelling the Spatial Extent of Medium Energy Electron Precipitation

Eldho Midhun Babu

Thesis for the degree of Philosophiae Doctor (PhD)
University of Bergen, Norway
2023

UNIVERSITY OF BERGEN

Modelling the Spatial Extent of Medium Energy Electron Precipitation

Eldho Midhun Babu

Thesis for the degree of Philosophiae Doctor (PhD)
at the University of Bergen

Date of defense: 22.09.2023

Year: 2023

Title: Modelling the Spatial Extent of Medium Energy Electron Precipitation

Name: Eldho Midhun Babu

Print: Skipnes Kommunikasjon / University of Bergen

Acknowledgements

I have a lot of people to thank. If you are in a rush, skip ahead.

I would not be here, for better or worse, without the importance of education instilled in me from my childhood by my parents Babu and Vincy, and my aunt Deepa.

The **P**(retty) **P**(owerful) group is without a doubt the best group at BCSS. This is an unbiased opinion. Hilde has been an incredible supervisor. She, along with my co-supervisors Christine and Ville have helped me learn the scientific process in the most fun way possible. Without them, I would still be a bunny in headlights. My PhD companions Jo(sephine) and (Just) Jone were a constant support and entertainment. You have got me stronger physically and mentally. I can finally do pull-ups and I will forever be unaffected by monster cans and milk cartons.

Synøve and Michael have been the best housemates I have ever had. Thank you for all the chill nights and cooking tips. Thank you, Margot (a.k.a. Mango) and Reham for being just fantastic human beings.

There have been many wonderful people here whom I could always seek help from. Thank you, Chris, for solving all my initial MATLAB struggles. Thank you, Spencer, for taking an interest in my work and helping me complete the 2nd project. Thank you, Cecilia, Norah, JT, Jone, Anders, and Kalle for all the interesting discussions about magnetospheric dynamics among other things.

To Ingrid, my partner (and unofficial therapist), you have motivated me to work harder every day without going insane. Thank you for fostering my weirdness and taking care of me.

Finally, I thank the pristine night sky I grew up under for my love for the final frontier. Without it, I might have ended up in a bank or something…

Outline

This thesis and the five papers included are submitted for the degree of Philosophiae doctor (PhD) in physics at the Department of Physics and Technology, University of Bergen.

The thesis consists of an introductory part and three published scientific papers and two papers currently under review in international peer-reviewed journals.

Papers I-III target the main objective of the thesis "Modelling Medium Energy Electron Precipitation Boundaries".

- **Paper I:** Babu, E. M., Tyssøy, H. N., Smith-Johnsen, C., Maliniemi, V., Salice, J. A., Millan, R. M., and Richardson, I. G. (2022). Determining Latitudinal Extent of Energetic Electron Precipitation Using MEPED On-Board NOAA/POES. Journal of Geophysical Research: Space Physics, 127, e2022JA030489. https://-doi.org/10.1029/2022JA030489

- **Paper II:** Babu, E. M., H. Nesse, S. M. Hatch, N. Olsen, J.A. Salice, and I. G. Richardson: An Updated Geomagnetic Index-based Model for Determining the Latitudinal Extent of Energetic Electron Precipitation, under review in Journal of Geophysical Research: Space Physics.

- **Paper III:** H.Nesse, E.M. Babu, J.A. Salice, and B. Funke: Energetic Electron Precipitation during Slot Region Filling Events, under review in Journal of Geophysical Research: Space Physics.

Papers IV and V study how the electron flux builds over time, as well as a stochastic analysis in order to achieve a realistic MEE parameterization.

- **Paper IV:** Nesse Tyssøy, H., N. Partamies, E. M. Babu, C. Smith-Johnsen and J. A. Salice (2021), The predictive capabilities of the Auroral Electrojet index for Medium Energy Electron Precipitation, Front. Astron. Space Sci., doi: 10.3389/fspas.2021.714146

- **Paper V:** Salice, J. A., Nesse, H., Babu, E. M., Smith-Johnsen, C., and Richardson, I. G. (2023). Exploring the predictability of the high-energy tail of MEE precipitation based on solar wind properties. Journal of Geophysical Research: Space Physics, 128, e2022JA031194. https://doi.org/10.1029/2022JA031194

Together the five papers provide key elements for future MEE parameterizations that go beyond the average picture, enabling realistic flux variability on both daily and decadal scales.

List of Abbreviations

EPP	Energetic Particle Precipitation
EEP	Energetic Electron Precipitation
MEE	Medium Energy Electron
ApEEP	Ap-based EEP model by *van de Kamp et al.* (2016)
IPCC	Intergovernmental Panel on Climate Change
CMIP	Coupled Model Intercomparison Project
HEPPA	High Energy Particle Precipitation in the Atmosphere
MEPED	Medium Energy Proton Electron Detector
NOAA	National Oceanic and Atmospheric Administration
EUMETSAT	European Organisation for the Exploitation of Meteorological Satellites
POES	Polar Orbiting Environmental Satellites
MetOp	Meteorological Operational satellite
MLT	Magnetic Local Time
CME	Coronal Mass Ejection
CIR	Corotating Interaction Region
HSS	High-speed Solar-wind Stream
Dst	Disturbance storm time (index)
RC	Ring Current (index)
IMF	Interplanetary Magnetic Field
BLC	Bounce Loss Cone
DLC	Drift Loss Cone
SAA	South Atlantic Anomaly
VLF	Very Low Frequency
ULF	Ultra Low Frequency
EMIC	Electromagnetic ion cyclotron (waves)
MHD	Magnetohydrodynamics
LEO	Low Earth Orbit
TSI	Total Solar Irradiance
SSI	Solar Spectral Irradiance
PAD	Pitch Angle Distribution
IGRF	International Geomagnetic Reference Field
AACGM	Altitude-Adjusted Corrected Geomagnetic
CGMLat	(altitude adjusted) Corrected Geomagnetic Latitude
NH	Northern Hemisphere
SH	Southern Hemisphere

Contents

Chapter 1

Introduction

The Earth's magnetosphere works as a giant shield against the incessant stream of charged particles from space. Most of it originates from our Sun as solar wind and the rest from outside our solar system as cosmic rays. A portion of these alien particles get trapped in the magnetosphere and form the Earth's radiation belts. The magnetosphere also consists of a co-rotating region populated with ions and electrons from the Earth's ionosphere, called the plasmasphere. These trapped particles have been a cause of interest since their discovery in 1958 for two important reasons. One, they pose ionising radiation hazards to astronauts and spacecraft in near-Earth space. Two, some of the trapped plasma showers down to the Earth's atmosphere in a process known as Energetic Particle Precipitation (EPP), which impacts the atmospheric chemistry and dynamics.

The precipitating electrons of energies <30 keV from the plasmasheet (as seen in Figure 1.1) result in a dazzling display of lights in the polar sky called the aurora. This mainly happens above 100 km, which marks the Kármán line, the beginning of space. Precipitating electrons with energies from 30 keV to 1 MeV can penetrate further down into the atmosphere reaching upper stratospheric altitudes (≈50 km). This is called Medium Energy Electron (MEE) precipitation. They are microscopic canon balls that knock out the orbital electrons from atmospheric gases, thus ionising them. As illustrated in the right side of Figure 1.1, these ionised gases can further produce odd nitrogen (NO_x: N, NO, NO_2) and odd hydrogen (HO_x: H, OH, HO_2), which has the potential to disrupt stratospheric and mesospheric ozone balance, consequently influencing atmospheric dynamics that can impact surface-level climate.

The effect of particle precipitation on the climate is a relatively new subject of debate. As of 2022, the International Panel for Climate Change (IPCC) has not included the effect of particle precipitation in its reports assessing climate change. However, the link between EPP, ozone destruction, and atmospheric dynamics has been well established. The Coupled Model Intercomparison Project Phase 6 (CMIP6) solar input recommendations have included EPP as one of its parameters. To fully understand the extent of Sun-Earth interaction on the Earth's climate, we require a complete knowledge of the EPP's frequency, flux, and geographic location. This can be done through observations of particles from satellites in orbit or computer models of trapped particles in the radiation belt. Both of these techniques have their limitations. The objective of my thesis has been to develop a model that predicts the geographic extent of MEE precipitation. MEE are typically not found in the solar wind. The magnetosphere catches

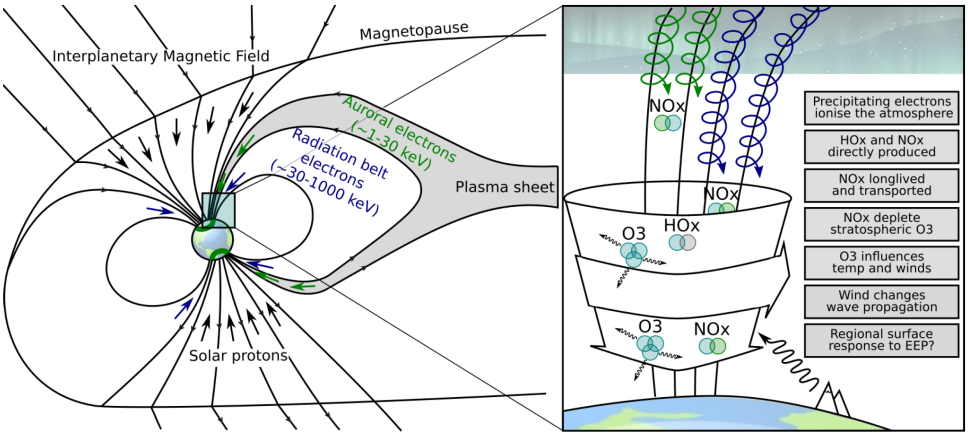

Figure 1.1: (left) Schematic view of important zones of electron precipitation in the magnetosphere. (right) A zoomed-in view illustrating how the precipitating electrons (auroral electrons represented as green spirals and radiation belt electrons as the blue spirals) affect the atmosphere through a chain of processes. Source: Adaptation of Thorne (1980) and Seppälä et al. (2014) by Linn-Kristine Glesnes Ødegaard and Christine Smith-Johnsen.

electrons from the solar wind and accelerates them to >30 keV inside the magnetosphere through different processes that are not fully understood. Also, the Sun goes through 11-year cycles generating different solar wind characteristics. This imposes a variable forcing in near-Earth space that influences the population growth and depletion of radiation belt electrons. Therefore, the solar cycle and the magnetosphere's response to different solar wind characteristics are important factors for understanding the nature of MEE.

The Medium Energy Proton Electron Detector (MEPED) on board the National Oceanic and Atmospheric Administration (NOAA) Polar Orbiting Environmental Satellites (POES) and the European Space Agency (ESA) Meteorological Operational (MetOp) Satellites have been measuring electrons and protons in the radiation belt from 1978, covering nearly four solar cycles. This makes it a potential candidate for investigating precipitating MEE. The MEPED instrument has a 0° and a 90° telescope that have been used to estimate precipitating particles, determine the spatial extent of MEE, and develop atmospheric ionisation models of MEE precipitation. However, the 0° and the 90° detectors are known to underestimate and overestimate precipitating fluxes, respectively. This leads to discrepancies between models that calculate the impact of EPP on the atmosphere, consequently affecting climate models that include particle precipitation. Therefore, we combine observations from the MEPED 0° and 90° detectors with the theory of pitch angle diffusion by wave-particle interaction to obtain a more realistic flux estimate of precipitating MEE.

1.1 Objective

The objective of this thesis and the included research papers has been to provide key elements for an MEE precipitation model and add to the scientific understanding of

the nature of MEE precipitation. This thesis is based on three main papers, that target the primary objective of this PhD work; modelling the geographical extent of the MEE precipitation. The exploration of MEE precipitation boundaries adds to our collective understanding of the physical processes of the inner magnetosphere governed by different plasma regimes. The last two papers highlight different approaches to understanding and modelling the MEE flux variation.

- **Paper I:** The equatorward extent of MEE precipitation over a full solar cycle from 2004 to 2014 using MEPED data was identified. We investigated which solar wind parameter and/or geomagnetic index provides the highest predictability for the equatorward boundaries. The pressure-corrected Dst index, Dst*, best correlated with the variation of equatorward boundaries for different electron energies and Magnetic Local Time (MLT) sectors and formed the basis of a linear regression model. The highest accuracy was found during periods dominated by Corotating Interaction Regions (CIRs)/High-speed Solar wind Streams (HSSs). The model exhibited, however, a systematic solar cycle bias, exaggerating the equatorward movement of the MEE precipitation region during solar minimum.

- **Paper II:** This study improved the accuracy of the first model by resolving the systematic solar cycle bias. This resolution is achieved through a multiple linear regression model with pressure-corrected Dst and pressure-corrected Ring Current (RC) indices. This model depends on the type of solar wind structure dominating the near-Earth space. We extend this model to the Southern Hemisphere as well.

- **Paper III:** Paper I and II also demonstrate the frequent occurrence of energetic electrons crossing the equatorward boundaries and filling the slot region. The ensuing MEE from within the plasmasphere cause precipitation long after the geomagnetic activity subsides, and can therefore not be easily modelled by geomagnetic indices. Paper III investigates the general solar wind and geomagnetic characteristics important for the occurrence of slot region filling events. Moreover, it explores the duration and associated NO production in the mesosphere. This demonstrates the importance of including slot region MEE when assessing the EPP impact on the atmosphere.

- **Paper IV:** This study explores the capability of the AE index to predict MEE precipitation and demonstrates that simple AE-based MEE-proxies can explain 72-82% of the identified MEE precipitation variance on a daily scale. The results will lay the foundations for a more accurate MEE model, especially the $\gtrsim$300 keV end of MEE precipitation, that can be used to study the atmospheric impacts of EEP.

- **Paper V:** This study investigates the high energy tail of the MEE precipitation ($\gtrsim$300 keV) relative to the $\gtrsim$30 keV electron precipitation with respect to maximum flux response, peak flux timing and duration. The results indicate that the epsilon coupling function has the best correlation (0.84) with the peak flux of $\gtrsim$300 keV electron precipitation. The peak timing of the high-energy tail is influenced by solar wind speed. Also, the $\gtrsim$300 keV precipitation lasts 2-3 days

longer than the $\gtrsim$30 keV precipitation. Moreover, paper V offers a pathway for developing a parameterization of MEE precipitation including a stochastic factor.

Together, Papers I-III constitute an important step towards a better understanding of the geographic extent of the MEE precipitation. The model can also be applied to examine the importance of the location of the plasmapause in moderating wave-particle interactions that lead to precipitation and how the precipitation boundaries might relate to the inner edge of the outer radiation belts. Alongside predictions of the intensity of the MEE fluxes in Paper IV, the geomagnetic index-based model will be a key element for constructing a realistic estimate of EEP variability to be applied in atmosphere climate models. Moreover, Paper V highlights the need for implementing a stochastic element to an MEE parameterization accounting for the range of possible flux responses, delay, and duration, allowing to represent the full range of EPP scenarios and hence variability. This is particularly important in order to include the impact of the high-energy tail of the MEE spectrum. Together the five papers provide the necessary features for a future MEE parameterization that goes beyond the average picture, enabling realistic flux variability on both daily and decadal scales.

1.2 Synopsis

Chapter 2 introduces the basic Sun-Earth interactions and the Earth's magnetospheric dynamics that are pre-requisite for particle precipitation. Chapter 3 describes the basic processes that initiate the precipitation of trapped particles in the magnetosphere. In Chapter 4, the atmospheric impact of the Sun-Earth interaction through EPP is discussed. This chapter also gives an overview of current precipitation models and how they compare. Chapter 5 describes the data and methodologies used to obtain the results of the papers included in this thesis. Chapter 6 shortly summarises the five papers. Chapter 7 offers concluding remarks, introduces some unpublished results, and highlights future prospects. Finally, all papers are included in Chapter 8.

Chapter 2

Sun and the Near-Earth Space

This chapter establishes an introductory theoretical framework required to understand the Sun-Earth interactions that lead to EPP: the solar activity, the solar-wind-magnetospheric coupling through the Dungey cycle, trapped particle motion in the magnetosphere, wave-particle interactions, and the relevant regions of Earth's magnetosphere.

2.1 Solar Activity

The Sun is an unexceptional type of star in our galaxy. Yet, it is the only star in our solar system, and it holds all the planets and non-planetary bodies together in its gravitational pull. The Sun is made of a state of matter called plasma. Although uncommon on Earth, plasma constitutes more than 99.9% of the ordinary matter in our Universe.

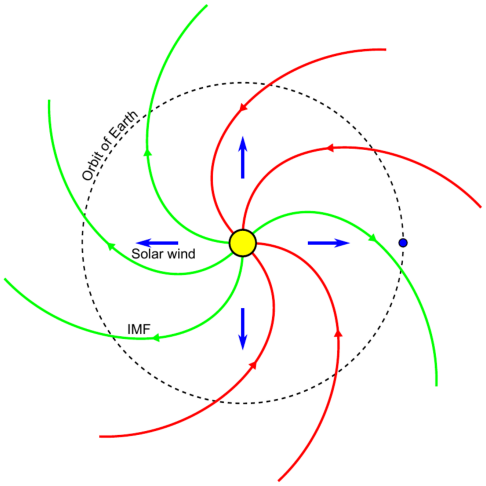

Figure 2.1: A simplified representation of Parker Spiral and the orbit of the Earth. The green field lines point away from the Sun, and the red field lines towards the Sun. The figure is an adaptation of Parker (1963) by Anders Ohma

Solar plasma escapes the surface of the Sun and fills the entire solar system as the solar wind. The supersonic solar wind can range from 300 km/s to more than 800 km/s.

Since the magnetic field is frozen in with the plasma, the footpoint of the solar wind remains anchored to the Sun. These magnetic field lines are called the Interplanetary Magnetic Field (IMF), and they spiral outward with the rotation of the Sun, forming the Parker Spiral shown in Figure 2.1.

Since the Sun is not a rigid body, different latitudinal regions of the Sun rotate at different speeds, with the polar regions taking around 10 additional days to complete a rotation with respect to the equatorial region. This is known as differential rotation. This causes the magnetic field lines on the solar surface to get tangled. Over time, these tangled field lines build up energy like a rubber band stretching and eventually break, releasing solar masses of the order of $\approx 10^{12}$ kg. This colossal event is known as a Coronal Mass Ejection (CME), shown on the right side of Figure 2.2. The broken field lines often accelerate solar plasma back into the Sun to relativistic energies releasing immense energy in the form of electromagnetic radiation, called a solar flare. Regions on the Sun that are slightly cooler and denser than the surroundings can lead to open magnetic field lines through which plasma flows at 800 km/s. These regions are called coronal holes, shown on the left side of Figure 2.2, and the fast plasma flows they produce are called High-speed Solar wind Streams (HSSs). As the HSSs catch up with the slow solar wind, compression regions form, known as Co-rotating Interaction Regions (CIRs) (*Richardson*, 2018).

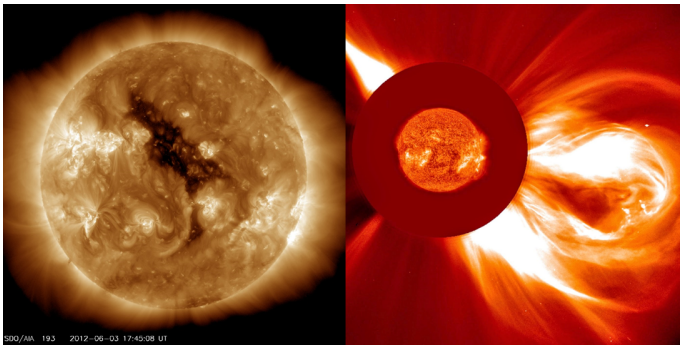

Figure 2.2: [Left] Coronal holes on the solar surface appear as dark regions in the X-ray images. [Right] A Coronal Mass Ejection (CME) erupting from the solar surface. Credits: NASA/ESA/SOHO

The Sun undergoes cyclic flipping of its poles every 11 years, called a solar cycle. A visible indicator of this cycle is the number of observable planet-sized dark spots on its surface, called sunspots. Sunspots have a temperature of $\approx$4000K and, therefore, are only relatively darker than the other regions on the solar surface. Sunspots are strongly correlated with CMEs and solar flares since these relatively darker regions are a source of disturbed and tangled magnetic field lines on the solar surface. As a result, the number of sunspots is an indicator of how active the Sun is with relevance to near-Earth space. The solar wind is often divided into three main categories(*Liou et al.*, 2018; *Schwenn*, 2006); slow/ambient, HSS, and CME. The slow ambient wind occurs in all phases of the solar cycle illustrated by the green line in Figure 2.3). Also, the coronal holes tend to appear more frequently during the solar minima, especially around the polar regions of the Sun. This results in an increased presence of HSSs during the solar minima, as shown by the blue lines in Figure 2.3. CMEs and HSSs are

significant for the near-Earth space and EPP. This will be discussed in Chapter 3.

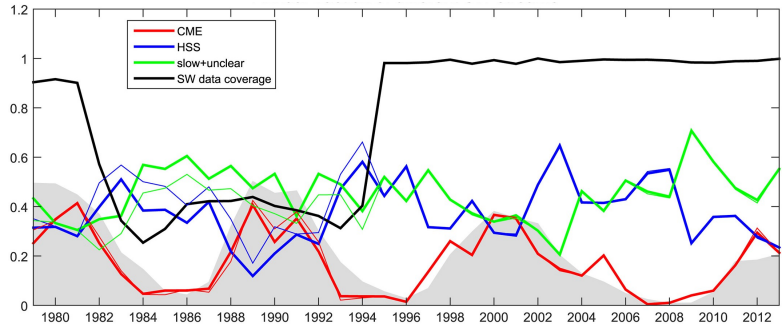

Figure 2.3: A plot with annual fractions of CMEs (red), HSSs (blue), and slow or unclear solar wind types. The grey shading is the sunspot number for each year, indicating the solar cycle. Source: Asikainen and Ruopsa (2016)

The supersonic solar plasma is powerful enough to strip the atmosphere from any terrestrial object in the solar system. Fortunately, the Earth generates a magnetic field in its core that acts as a shield against the solar wind. This geomagnetic field is approximately dipolar and forms closed loops directing into the north pole and coming out of the south pole. Its shape is predominantly determined by the solar wind. On the dayside, the magnetosphere gets compressed by the solar wind pressure, and on the nightside, it is stretched outwards due to the tangential drag of the solar wind and can extend even past the orbit of the Moon. When the IMF embedded in the solar wind meets the geomagnetic field, it leads to large-scale reconnection of field lines and the convection of plasma. This process was first explained by *Dungey* (1961) and is often called the Dungey cycle.

2.2 The Dungey cycle

The solar wind IMF can have any direction by the time it reaches the Earth's orbit. The magnetised solar wind cannot directly penetrate the geomagnetic field lines (*Baumjohann and Treumann*, 2012), but if the IMF has a southward component (numbered 1 in Figure 2.4), it connects with the geomagnetic field lines pointing northward on the Earth's dayside (numbered 1 inside the grey region of Figure 2.4). This initiates the Dungey cycle. From here, every number addressed in this section will refer to the numbers shown in Figure 2.4. The reconnected geomagnetic field line will have one end connected to the Earth and the other to the Sun through the solar wind (numbered 2). Solar wind transports the reconnected field lines towards the nightside (numbered 3 to 6) to distances of around 200 R_E where they meet the other half of the open geomagnetic field lines and lead to nightside reconnections (numbered 7). Thus, the solar wind detaches from the geomagnetic field and continues away from the Earth (numbered 8). The magnetic tension of the geomagnetic field lines brings the nightside reconnected field lines back towards the Earth like a rubber band (numbered 7 to 8 in the grey region). Under equilibrium, these field lines return to the dayside, filling the lost field lines in that region and completing the Dungey cycle. The important aspect of this

cycle is that the plasma is frozen in with the field lines, representing large-scale circulation and injection of plasma. The consequences of this are discussed in the subsequent sections.

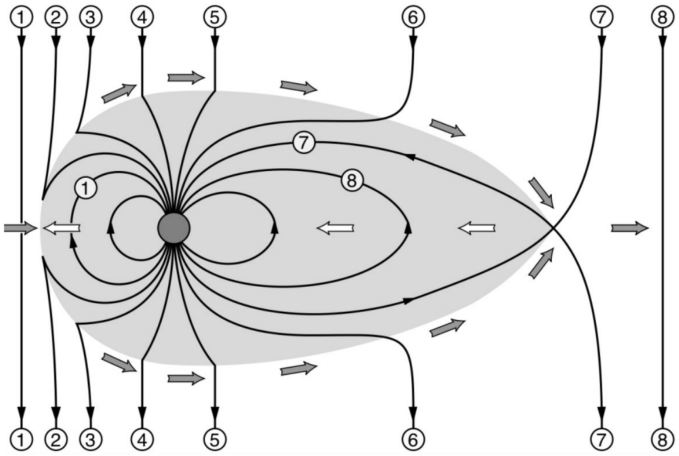

Figure 2.4: The Dungey cycle shows the interaction of the solar wind with the geomagnetic field. Source:Baumjohann and Treumann (2012)

The Dungey cycle is a very simplistic representation of the geomagnetic interaction with the solar plasma. In reality, this process is far more complex and yet to be completely comprehended.

2.3 Trapped Particles

The physics of trapped plasma in the Earth's magnetosphere is determined by the electromagnetic force (or Lorentz force) represented by the Equation 2.1:

$$m\frac{d\mathbf{v}}{dt} = q(\mathbf{E} + \mathbf{v} \times \mathbf{B}) \tag{2.1}$$

where m is the mass of the particle, q its charge, v its velocity, E the electric field and B the magnetic field.

However, this equation is only valid for homogeneous electromagnetic field lines. Earth's magnetic field lines are not homogeneous as they vary spatially and temporally. This results in the trapped particles drifting through the magnetosphere. A detailed description of these magnetic drifts and their governing equations can be found in *Baumjohann and Treumann* (2012) and *Koskinen and Kilpua* (2022).

As a result of the magnetic drifts, the trapped particles exhibit three quasi-periodic motions in the magnetosphere. The magnetic moment of these particles in ideal conditions can be treated as a constant since they change on timescales that are much longer than the timescales of particle motion in the magnetosphere. Therefore, these motions are collectively called adiabatic invariants. The first adiabatic invariant is the gyro motion of the trapped particle around the field lines in a spiral motion, as seen in Figure

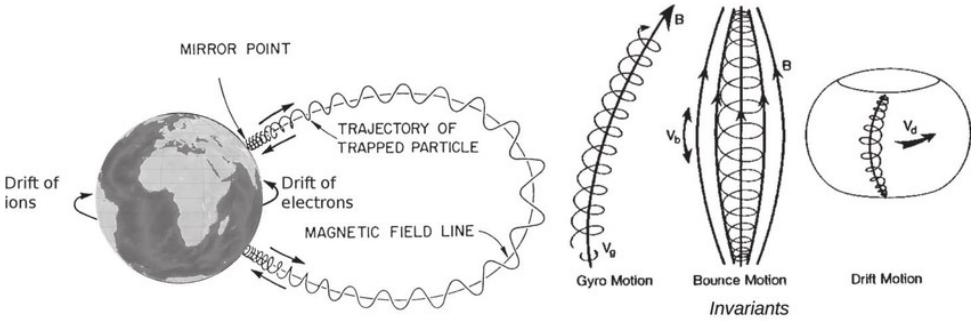

Figure 2.5: Motion of trapped particles along the magnetic field lines. Source: Adaptation from Baumjohann and Treumann (1996)

2.5. The second is the bounce motion which happens when the spiralling particle encounters a higher density of magnetic field near the poles and bounces back towards the equator. They reach the other pole and repeat the process. The point at which the particles change their trajectory is called a mirror point (Figure 2.5). If the mirror point is $<$100 km, they encounter the atmospheric gases and are assumed to be 'lost' to the atmosphere. The third adiabatic invariant is the drift motion of particles around the Earth in closed orbits, as seen in Figure 2.5. This is caused by the variation of the magnetic field strength with distance from the Earth, resulting in a force perpendicular to both the magnetic field and the particle's velocity. Due to the opposite charge, the ions will drift westward and the electrons eastward, thus generating a current around the Earth called the ring current. The drift periods vary with particle energy and distance from the Earth. $>$30 keV to 1 MeV electrons complete multiple orbits around the Earth within a day (*Horne et al.*, 2005). The mirror point and the ring current are highly relevant to this thesis and will be continuously referenced from hereon.

2.4 Regions of the Magnetosphere

This section provides a brief overview of the magnetospheric system with reference to Figure 2.6. The different regions are characterised by varying plasma densities and temperatures and large-scale currents generated by the motion of plasma. The boundary between the magnetosphere and the solar wind marks the magnetopause. The solar wind will compress this region on the dayside and elongate it on the nightside. The dynamic pressure of the solar wind will be equalised at this region by the Earth's magnetic pressure. When the solar plasma enters the denser magnetosphere, the electron and ions get directed in opposite directions, inducing currents on the magnetopause, sometimes called the Chapman-Ferraro currents (*Chapman and Ferraro*, 1931). On the nightside, these currents close as the tail current.

Inside the magnetopause are regions marked by open field lines connected to the Earth at high latitudes on one end and to the IMF on the other. The first boundary layer going inward from the magnetopause is the plasma mantle, a thin transition region where plasma from inside and outside the magnetosphere interact. Then there are lobes, an expansive region composed of rarefied plasma, extending towards the magnetopause

in both hemispheres. There are also two holes in the magnetosphere on either pole of the Earth where the solar plasma is funnelled downward directly into the atmosphere. These holes are called polar cusps.

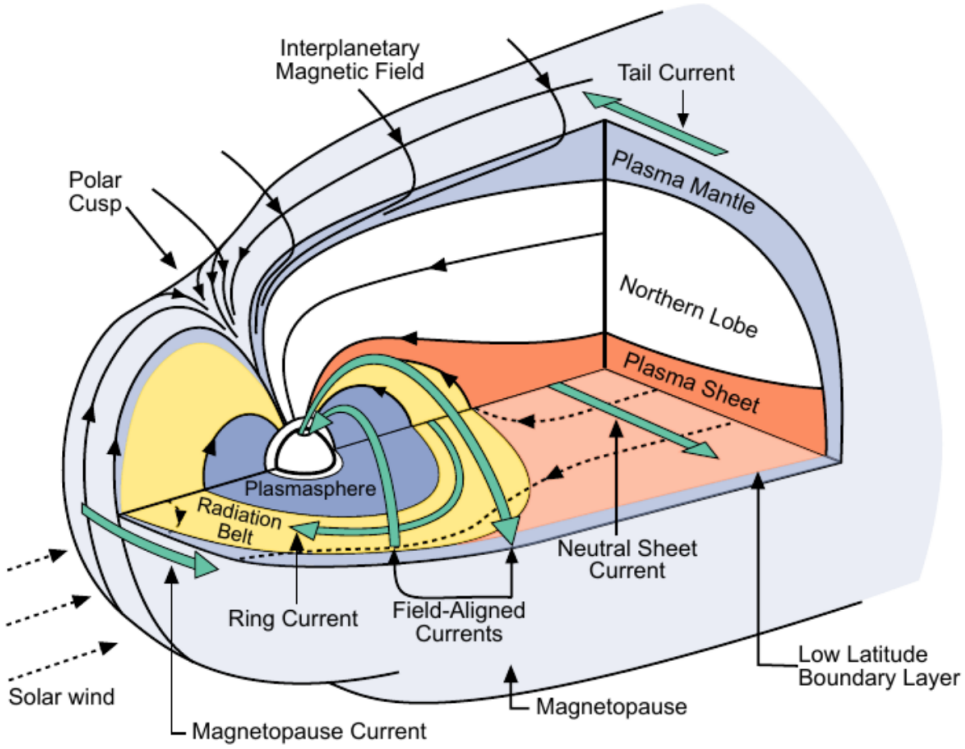

Figure 2.6: The magnetospheric system with the representation of different regions and large-scale current systems. Source: Adaptation by Anders Ohma from Kivelson and Russell (1995)

The remaining regions described in this section contain magnetic field lines that are not connected to the IMF and form closed loops on the Earth. The first and the most important of these are the radiation belts, where particles are accelerated to ultra-relativistic kinetic energies and pose severe hazards to astronauts and spacecraft in near-Earth space. More importantly, they carry the ring current and are the source of Medium Energy Electron (MEE) precipitation. The radiation belt and particle precipitation are discussed in detail in Chapter 3. At the tail-end of the radiation belt, the magnetic field lines get stretched into a sheet-like form and are populated with hot dense plasma. This area is called the plasma sheet. Then there is the plasmasphere, a region that co-rotates with the Earth and is populated with cold dense plasma originating from the Earth's ionosphere and can be considered as an extension of the Earth's ionosphere. The plasmasphere is separated from hotter rarefied plasma in the outer regions by a boundary layer called the plasmapause. Plasmapause plays an important role in particle precipitation, which will be discussed in the next chapter.

Chapter 3

Energetic Particle Precipitation

This chapter gives a brief overview of different types of particle precipitation. The main focus is on EPP associated with the trapped electron population in the inner magnetosphere, often referred to as MEE. Here processes in the radiation belt can accelerate electrons to relativistic energies and change their mirror point such that the electron is lost to the atmosphere. Their high energies ionise and change the chemical components directly throughout the mesosphere and potentially the upper stratosphere. Finally, as these processes are ultimately driven by the solar wind, characteristics of CME and HSS/CIR are shortly discussed.

3.1 EPP origins

The term EPP refers to the deposition of kinetic energy in the Earth's atmosphere by any particle from space. Generally, they are from the following processes:

- Cusp aurora, caused by solar wind plasma funnelling directly down through the cusp regions into the atmosphere. Also, the homogeneous plasma flux from open field lines precipitating in the polar region is called the polar rain [see *Newell et al.* (2009) for more details]. The typical energy ranges are several 100 eV electrons and 2-10 keV protons (*Dang et al.*, 2018; *Xiao et al.*, 2013).

- Precipitation from the plasmasphere and the plasma sheet population. Electrons and protons of energies $<$30 keV and $<$10 keV, respectively, that precipitate in the polar region around 100 km, forming two oval regions centred around the geomagnetic poles. This precipitation forms the aurora [for details, see *Swift* (1981), *Thorne et al.* (2010) and *Akasofu* (2023)].

- Cosmic ray precipitation from outside our solar system. The IMF embedded in the solar wind prevents most alien particles from penetrating our solar system. But often high energy particles ($\approx$300 MeV and higher when reaching the Earth) generated from galactic and extra-galactic processes such as supernovae, quasars, and gamma-ray bursts penetrate into the Earth's atmosphere and create a cascade of secondary particles that can reach the surface of the Earth.

- Radiation belt electron precipitation of $>\approx$30 keV is caused by trapped electrons which undergo acceleration and pitch angle scattering changing their mirror point such that they are lost to the atmosphere. Radiation belt protons of energy $>\approx$1 MeV are also lost to the atmosphere through similar processes. The high energies of both electrons

and protons cause energy deposition deep into the atmosphere below the altitudes of the observable aurora.

Radiation belt electron precipitation forms the backbone of this thesis, and its causes and effects are explored in detail in the subsequent sections.

3.2 Atmospheric Loss Cone

The concept of pitch angle and atmospheric loss cone is a key terminology in the realm of radiation belt particle precipitation. The pitch angle of a trapped particle undergoing bounce motion along the field line is defined as the angle between its velocity vector and the local magnetic field line, as seen in Figure 3.1. They are generally referenced with respect to the geomagnetic equator and can be expressed as:

$$\sin^2 \alpha_{eq} = \frac{B_{eq}}{B_m} = \frac{\cos^6 \lambda_m}{\sqrt{(1+3\sin^2 \lambda_m)}} \tag{3.1}$$

where α_{eq} is the equatorial pitch angle, B_{eq} the equatorial magnetic field strength, B_m magnetic field strength at the mirror point and λ_m the geomagnetic latitude of the particle's mirror point.

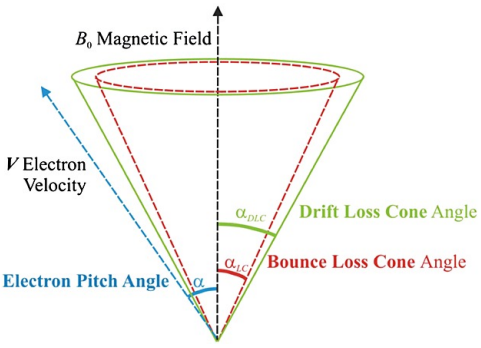

Figure 3.1: Illustration of the atmospheric loss cone, including the electron pitch angles that form bounce loss cone and drift loss cone. Source: Rodger et al. (2013)

A particle with 90° equatorial pitch angle will have no velocity component parallel to the local magnetic field line and, therefore, will remain stationary as its mirror point will be the equator. As the particle's pitch angle decreases, the mirror point is found at higher latitudes and lower altitudes. Mirror points less than ≈100 km, implies that the electrons are likely to collide with atmospheric gases and lose their energy to the atmosphere.

Trapped particles with equatorial pitch angles corresponding to mirror points below 100 km are said to be inside the Bounce Loss Cone (BLC). Therefore, particles with $\alpha < \alpha_{BLC}$ get precipitated within a few bounces. As Equation 3.1 implies, the pitch angles at the mirror point, and hence the loss cone's size, depend on the magnetic field strength. Therefore, the size of the BLC changes across both latitude and longitude in the Earth's imperfect dipole field. The change of BLC across longitude is relevant for the drift motion of particles around the Earth. Over one drift period, the BLC with the largest angular width is known as the Drift Loss Cone (DLC) with pitch angle α_{DLC}. Both BLC and DLC are represented in Figure 3.1. Particles with pitch angle $\alpha_{BLC} < \alpha < \alpha_{DLC}$ will theoretically mirror just above ≈100 km and

thus drift around the Earth until they encounter a weaker magnetic fields strength such as e.g. the South Atlantic Anomaly (SAA) (*Rodger et al.*, 2013), a region in the southern hemisphere where the radiation belts come closest to the Earth's surface. There the mirror points will be deeper than the rest of the radiation belt, and therefore, these particles get lost over the SAA. Hence, the SAA region is known to cause high radiation exposure to spacecraft and life in near-Earth orbits. Most instruments need to be turned off while passing over the SAA. It also creates problems for the study of precipitation fluxes and their geomagnetic distribution. This will be covered in Chapter 5.

3.3 The Radiation Belts

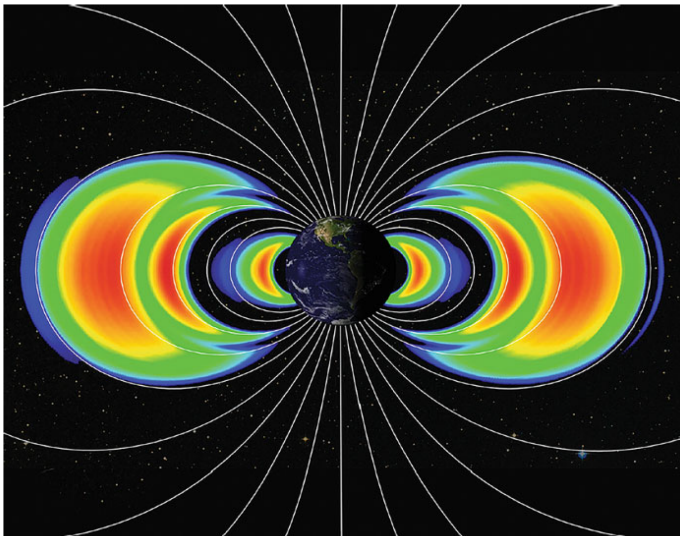

Figure 3.2: An illustration of the radiation belts showing the inner radiation belt closest to the Earth, the empty slot region, and the outer radiation belt farthest from the Earth. Source: NASA/APL

As mentioned in the previous sections, trapped solar wind electrons and protons are accelerated to relativistic energies in the radiation belts. The same processes affect the electron's pitch angles causing MEE precipitation. The radiation belts are also known as the Van Allen belts, after James Van Allen, who first discovered this magnetospheric region in 1958 using data from the U.S. Explorer I and Explorer III spacecraft (*Van Allen*, 1959). The radiation belts have a highly complex structure but can be broadly divided into two main regions: the inner radiation belt, which extends from about $1.1 - 2\ R_E$, and the outer radiation belt, which extends from about $3 - 10\ R_E$ at the equatorial plane. The inner radiation belt is primarily composed of electrons (of energy $\approx$100 keV) and extremely energetic protons ($\approx$100 MeV) and is relatively stable on daily timescales, while the outer radiation belt is primarily composed of high-energy protons (1-100 keV) and highly energetic electrons (0.1-10 MeV) and is prone to rapid changes in its particle population in a matter of hours to days (*Li and Temerin*, 2001; *Li et al.*, 2015). The radiation belt population has two sinks: the first is precipitation into the atmosphere, and the second is back into the solar wind through magnetopause shadowing. Magnetopause shadowing happens when the outer radiation belt population gets exposed to

the solar wind while they drift around the Earth. This is a result of the solar wind pressure rapidly compressing the dayside magnetopause earthward and revealing trapped particles into the solar wind. As seen in Figure 3.2, a slot region exists between the two radiation belts. This space is usually empty of energetic electrons, resulting from a balance between radial transport from ultra-low frequency (ULF) waves and atmospheric loss through plasmaspheric hiss waves and lightning-generated whistler waves (*Kim et al.*, 2011). During moderate to high geomagnetic activity they get filled and tend to gradually decay away through atmospheric precipitation in a process that can take weeks (*Kavanagh et al.*, 2018).

3.4 The Loss Process

As mentioned in Chapter 2 Section 2.3, trapped particles in the radiation belts undergo three quasi-periodic motions (gyro, drift, and bounce). When one or more of the associated adiabatic invariants get violated, the radiation belt particles experience acceleration and/or changes in the pitch angle. Pitch angle diffusion towards the bounce loss cone will result in the loss of the particles to the atmosphere. The primary reason for this violation and loss of particles to the atmosphere is magnetospheric waves. They are a result of magnetospheric perturbations from temperature and density gradients, plasma instabilities, and pitch-angle anisotropy (see *Millan and Thorne* (2007) for a comprehensive description). When a trapped particle encounters a magnetospheric plasma wave, the wave exerts a force on the particle, causing it to rotate or "pitch" its velocity vector. This changes the initial direction of the particle motion, and this mechanism is called pitch angle scattering. The magnitude of this scattering is a function of the amplitude and frequency of the plasma wave and the velocity and mass of the particle. These wave-particle interactions also change the particle's pitch angle distribution, called pitch angle diffusion. When the trapped particles undergoing pitch angle scattering find themselves in the atmospheric loss cone, they precipitate. Pitch angle scattering can also increase the kinetic energy of the particles. This is responsible for the acceleration of radiation belt electrons to much higher energies than what is found in the solar wind. As a consequence, some particles are also bumped up to higher L-shells, a portion of which gets lost through magnetopause shadowing.

Figure 3.3 shows the spatial distribution of dominant plasma waves in the inner magnetosphere. The significant waves responsible for pitch angle scattering in the radiation belts are the following (*Millan and Thorne*, 2007; *Ripoll et al.*, 2020; *Thorne*, 2010, & references therein):

- **ULF Waves**

  ULF stands for Ultra-low Frequency waves of frequencies between 1 mHz and 10 Hz. They are magnetohydrodynamic (MHD) waves generated from either plasma instabilities or originating from the solar wind through interactions with the magnetosphere. ULF waves are responsible for acceleration and loss of electrons in the range of a few keV to tens of keV. They are found in the inner and the outer radiation belts (*Thorne*, 2010).

- **VLF Waves**

  The Very Low Frequency (VLF) waves of the kHz frequency range, originating from ground-based transmitters, are a known source of precipitation of electrons of energy $\approx$500 keV. These electron lifetimes get reduced by a factor of 10 around the outer regions of the inner radiation belt at L$\approx$1.8. However, the VLF waves are inefficient at

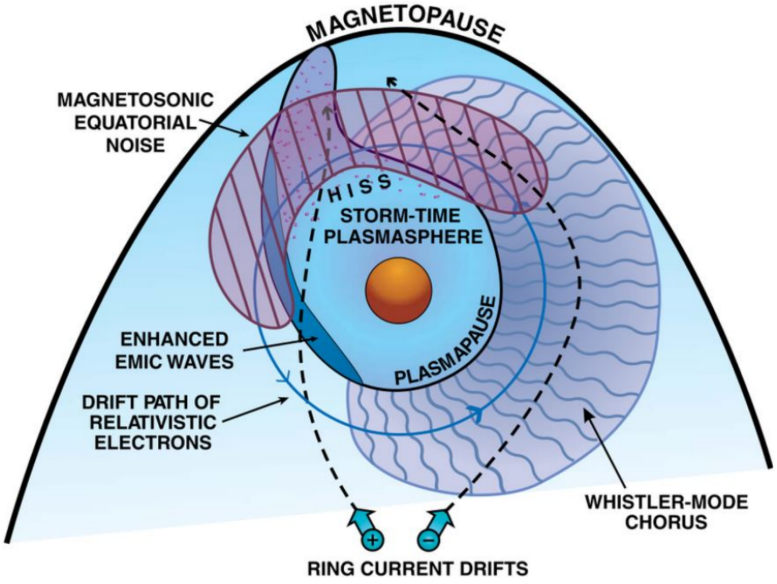

Figure 3.3: An illustration of the spatial distribution of important plasma waves responsible for pitch angle scattering and diffusion in the inner magnetosphere. The magnetopause is facing the direction of the Sun. The figure also shows the plasmapause, a region that marks an abrupt change in the density of the medium in which the waves propagate. The Earth is shown as the bronze ball in the centre. Source: Thorne (2010)

precipitating <2 MeV electrons from the inner radiation belt or the slot region (*Millan and Thorne*, 2007; *Ripoll et al.*, 2020).

- **Lightning-Generated Whistlers**

  Lightning-generated whistlers are electromagnetic waves in the VLF frequency domain. They are generated by lightning discharges in the Earth's atmosphere (mainly cloud to ground). They are called "whistlers" because of their characteristic "whistling" sound that can be heard when they are received by a radio receiver. Once generated, they travel along the magnetic field lines and cause resonant interactions with the trapped electrons in the inner radiation belt, resulting in their precipitation (*Millan and Thorne*, 2007; *Ripoll et al.*, 2020).

- **Whistler Mode Hiss Waves**

  Whistler mode hiss waves are electromagnetic waves with a broad frequency range (50 Hz to 2 kHz). They are found in the inner magnetosphere from around L$\approx$2 to the location of the plasmapause. They produce a "hissing" sound when heard by a radio receiver. Although postulated to originate from chorus emissions, their origin remains a matter of debate. The whistler mode hiss waves are detected in geomagnetically quiet and active conditions and are the main source of the slot region formation and the double-belt structure of the Van Allen belts (*Millan and Thorne*, 2007; *Ripoll et al.*, 2020).

- **EMIC Waves** The Electromagnetic Ion Cyclotron (EMIC) waves are plasma waves generated by ions' interaction with the magnetosphere's electromagnetic field. They are

observed in multiple frequency bands both inside and outside the plasmasphere. EMIC waves are very efficient in precipitating relativistic electron energies since they meet the wave-particle resonance condition for easy transfer of energy and momentum from these waves to electrons of relativistic energies. These waves are observed to intensify during the main phase of a geomagnetic storm due to the injection of anisotropic ring current ions into the inner magnetosphere. EMIC waves are extremely powerful, but their efficiency in precipitating electrons is limited due to their short duration and low spatial extent, covering only one or few Magnetic Local Time (MLT) sectors (*Fraser et al.*, 2010; *Jordanova et al.*, 2010; *Thorne*, 2010).

- **Whistler Mode Chorus Waves**

  Whistler mode chorus waves are electromagnetic waves generated from the interaction of energetic electrons with plasma waves such as whistler mode waves. Due to their characteristic frequency modulation, they are heard as "chirping" sounds on a radio receiver, hence their name. They have frequencies between 100s of Hz to a few kHz and are observed from outside the plasmasphere to beyond geostationary orbits. Whistler mode chorus waves are capable of severe energising of electrons, accelerating 10s of keV electrons to several MeVs. They dominate the electron scattering process outside the plasmasphere and cause precipitation from the outer radiation belt region (*Millan and Thorne*, 2007).

Although not a wave, microbursts are intense, short-timescale (≈10 millisecond) precipitation events observed in the morning sector that is closely linked with wave activity. They generally have energies from 10s to 100s of keV. The origin of microbursts is a matter of discussion but can be postulated to be driven by chorus waves and EMIC waves (*Ripoll et al.*, 2020).

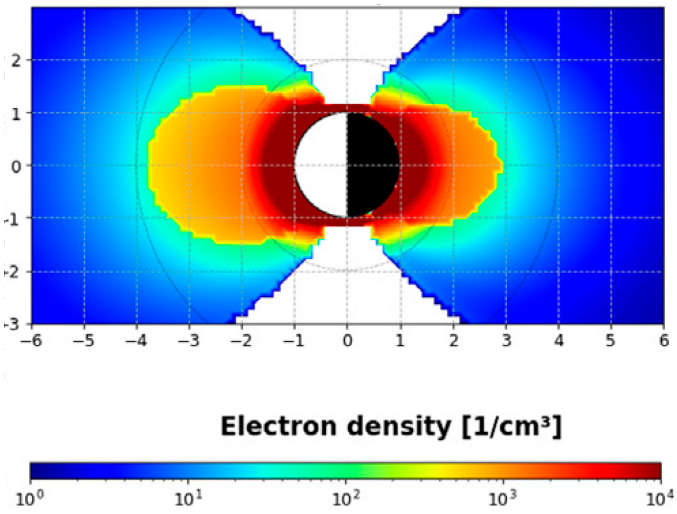

Figure 3.4: A distribution of electron number density in the meridian plane of the Earth. The region in colours red, orange, and yellow marks the plasmasphere. The electron number density bar below indicates the sharp change of plasma density going from the plasmasphere to the blue region. This boundary marks the plasmapause. Source: Pierrard et al. (2021)

As mentioned in Chapter 2 Section 2.4, the plasmapause indicates the boundary between the plasmasphere and the plasma-poor outer magnetosphere. This difference can be of the order of 10^4 particles per cm^3, as seen in Figure 3.4. Since the characteristics of the plasma and electromagnetic waves propagating in the magnetosphere depend on the medium it travels, the plasmapause will mark a change in their characteristics. Therefore, the plasmapause location is considered to play an important role in determining the L-shells corresponding to precipitating particles. The plasmapause location can vary significantly with geomagnetic activity ($\approx 7\ R_E$ during quiet conditions to $\approx 2\ R_E$ during active conditions), therefore, changing the boundaries of precipitation as well. *Grebowsky* (1970) theorises that during geomagnetically active periods, the increased tail-side reconnections enhance the flow of plasma from the outer magnetosphere to the inner magnetosphere thus decreasing the L-value of plasmapause location. Conversely, under steady-state conditions, the magnitude of the dawn-dusk electric field decreases, driving the plasmapause to higher L-values. *Moldwin et al.* (2002) and *O'Brien and Moldwin* (2003) developed an Ap-index-based model that predicts the location of the plasmapause. This model has been used by *van de Kamp et al.* (2016) and *van de Kamp et al.* (2018) to model the precipitation boundaries of MEE ($> 30\ keV$) precipitation. We will come back to this in the following chapters.

3.5 CME and CIR Driven Storm Influences

As discussed in Chapter 2, the two main solar storms with relevance to the radiation belt population are CME- and CIR-driven storms. Both storms generate different responses to the Earth's magnetosphere in terms of particle population in the radiation belt and particle precipitation to the atmosphere, some of which are seen in Figure 3.5 and Table 3.6.

The primary component of a CME is the ejecta, the vast mass emanating from the solar surface that carries plasma and the magnetic field embedded in it towards the interplanetary space. A CME storm typically manifests in three layers (*Kilpua et al.*, 2017). First is the interplanetary shock, which is a result of the ejecta travelling faster than the ambient solar wind, making the structure supersonic. The second layer is the sheath region of compressed solar wind where the plasma is turbulent. The third layer is the ejecta itself, which may contain a magnetic cloud, a large-scale coherent magnetic field surrounded by plasma of relatively low proton temperature. The associated geomagnetic storm is driven by the strong magnetic field in the ejecta and the sheath, while the interplanetary shock results in various observable effects in the Earth's magnetic field and in the radiation belts (*Borovsky and Denton*, 2006). CIRs are compression regions due to HSSs pushing the ambient solar wind. A CIR-triggered geomagnetic storm can be driven by either the compression regions, HSSs or both. CIR storms exhibit a 27-day periodicity towards the beginning of a solar minimum and tend to dominate storms in that time window (*Mursula and Zieger*, 1996; *Richardson et al.*, 2001).

Dst index represents the strength of the magnetospheric ring current (*Malin and Barraclough*, 1991; *Sugiura*, 1964). The Dst index is a function of the density and temperature of the plasmasheet and the strength of the magnetospheric convection (*Kozyra and Liemohn*, 2003; *Thomsen et al.*, 1998). CMEs are observed to have more of all the above-mentioned factors than CIR-driven storms. Therefore, CMEs have been found by *Denton et al.* (2006); *Yermolaev and Yermolaev* (2002) to be responsible for stronger ring currents and hence, more powerful Dst values. Although not as powerful as the CME-driven storms, *Dmitriev et al.* (2005); *Kataoka and Miyoshi* (2006) found CIRs to be more efficient at enhancing radiation belt flux enhancements at geosynchronous orbit. This is associated with their long-lasting nature and continuous electric field fluctuations associated with the turbulence found in coronal

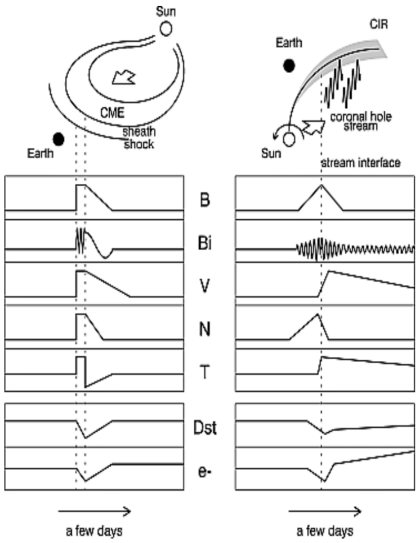

Figure 3.5: An illustration of characteristic differences and magnetospheric responses of CME and CIR driven storms. From top to bottom: the IMF strength B, Bx or Bi component of the IMF, solar wind speed v, plasma number density N, plasma temperature T, Dst index, and >2 MeV electron flux at geosynchronous orbit. Source: Kataoka and Miyoshi (2006)

Phenomenon	CME-Driven Storms	CIR-Driven Storms
Phase of the solar cycle when dominant	solar maximum	declining phase
Occurrence pattern	irregular	27-day repeating
Calm before the storm	sometimes	usually
Solar energetic particles (SEP)	sometimes	none
Storm sudden commencement (SSC)	common	infrequent
Mach number of the bow shock	moderate	high
β of magnetosheath flow	low	high
Plasma-sheet density	very superdense	superdense
Plasma-sheet temperature	hot	hotter
Plasma-sheet O^+/H^+ ratio	extremely high	elevated
Spacecraft surface charging	less severe	more severe
Ring current (Dst)	stronger	weaker
Global sawtooth oscillations	sometimes	no
ULF pulsations	shorter duration	longer duration
Dipole distortion	very strong	strong
Saturation of polar-cap potential	sometimes	no
Fluxes of relativistic electrons	less severe	more severe
Formation of new radiation belts	sometimes	no
Convection interval	shorter	longer
Great aurora	sometimes	rare
Geomagnetically induced current (GIC)	sometimes	no

Figure 3.6: A table of summary of characteristic differences between CME-driven storms and CIR-driven storms. Source: Borovsky and Denton (2006)

hole streams (*Kataoka and Miyoshi*, 2006; *Kilpua et al.*, 2017). However, *Yuan and Zong* (2012) found CMEs produce higher relativistic electron flux in the entire outer radiation belt compared to CIRs. This is consistent with *Asikainen and Ruopsa* (2016); *Salice et al.* (2023), which suggests CME storms produce more >100 keV electron enhancements in the radiation belts than CIR-driven storms. A statistical study of the radiation belt evolution during CME and CIR storms using the Van Allen Probes by *Shen et al.* (2017) concludes that the flux en-

hancements are heavily dependent on the L-values and the energy of the electrons, with CMEs and CIRs being equally efficient at increasing electron fluxes at different regions in the radiation belt for different electron energies. Furthermore, *Asikainen and Ruopsa* (2016); *Zhang et al.* (2008) indicate a combination of CME and CIR are more potent at MEE flux enhancements in the radiation belts compared to isolated CMEs or CIRs.

Chapter 4

Atmospheric Impact

EEP is a major source of energy deposition from space. The type of particle, the energy and the pitch angle govern the ionisation throughout the atmosphere. The ensuing consequences in terms of electrodynamics, chemistry, and neutral dynamics depend on the background atmosphere, geographical location, and when the precipitation takes place. While the MEEs mainly deposit their energy throughout the mesosphere, the subsequent extent may extend deeper into the atmosphere. This chapter covers the basic structure of the Earth's atmosphere, its important regions relevant to EPP and how the Sun affects the Earth's climate. The last part of this chapter covers recent research that predicts the impact of MEE precipitation on the atmosphere with a focus on *van de Kamp et al.* (2016) that has been included in The Coupled Model Intercomparison Project Phase 6 (CMIP6) climate model.

4.1 Basic Structure

To understand the effects of EPP on the Earth's atmosphere, it is important to know its structure and composition. The atmosphere can be divided into four layers based on the variation of temperature with altitude, as seen in Figure 4.1. From the ground up, the troposphere extends to $\approx$10 km dependent on season and latitude. It is primarily heated by solar photons in the visible wavelength range. The temperature is inversely proportional to altitude in the troposphere, and most weather phenomena take place here. It is the source of gravity waves and planetary waves which strongly govern the layers above. The edge of the troposphere is called tropopause. Above, in the stratosphere, the temperature increases with altitude to $\approx$50 km. This is due to the solar ultraviolet (UV) absorption of abundant ozone (O_3) molecules present here. This process also shields the harmful UV radiation from reaching ground level and causing significant health risks to life. The termination layer of the stratosphere marks the stratopause. Above the stratopause, in the mesosphere, the temperature decreases rapidly with height up to $\approx$85–100 km dependent on the season and geographic latitudes (*Brasseur and Solomon*, 2005). The infra-red (IR) radiative cooling by CO_2, H_2O, and O_3 molecules in the mesosphere is responsible for its sharp decreasing temperature profile. This region also contains O_3 molecules to a lesser extent than in the stratosphere. Above the mesopause, in the thermosphere, the temperature gradient turns positive due to the dominant presence of solar UV and X-rays that energise the molecules. Auroras and many satellites in Low Earth Orbit (LEO) are found in the thermosphere.

Based on its composition, the atmosphere is often divided into two layers: the homosphere and the heterosphere. The homosphere is from ground level up to $\approx$100 km. Here 78% of the atmospheric mass consists of nitrogen, 21% oxygen, and the rest of argon, carbon dioxide,

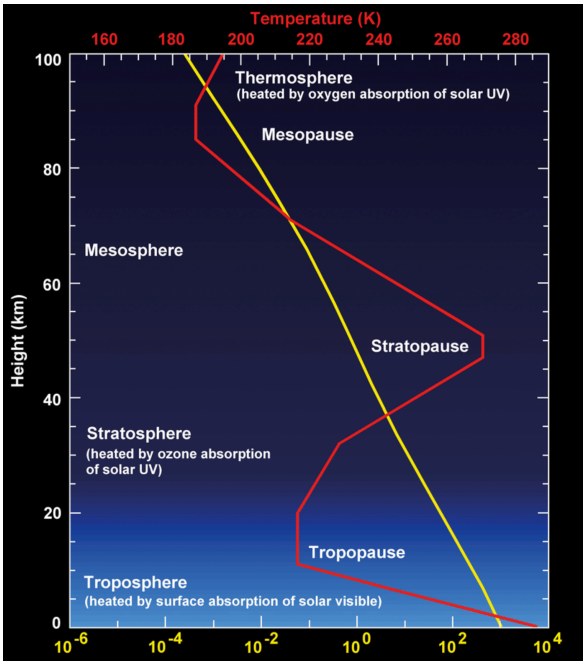

Figure 4.1: Basic structure of the Earth's atmosphere with its different regions and variation of temperature and pressure with altitude. The red line represents temperature, and the yellow line represents pressure. Source: U.S. Standard Atmosphere (1976)

and other minority gases. The density in the homosphere generates sufficient collision rates to support the mixing of gases, thus enabling a uniform distribution of molecules. Above 100 km, in the heterosphere, the gaseous composition is a function of altitude. Lighter gases (e.g. hydrogen and helium) have higher thermal velocities to move to higher altitudes because of their lower gravitational influence compared to heavier gases (e.g. nitrogen and oxygen). Here, the density is very low, the interaction between molecules is rare, and mixing is minimal. The density of gases in this region is a function of solar photon flux (day-night cycle), solar cycle, and geomagnetic activity (*Jacchia*, 1965).

4.2 Solar Forcing

The term "solar forcing" is used in atmospheric science to indicate the influence of the Sun on the Earth's atmosphere. This section covers the atmospheric effects of solar photons and energetic particle precipitation.

4.2.1 Solar Radiative Forcing

Solar radiative forcing refers to electromagnetic radiation. It is considered the main driver of atmospheric chemistry and weather systems. Solar radiative forcing is often divided into Total Solar Irradiance (TSI) or Solar Spectral Irradiance (SSI). TSI is the primary driver of the climate systems (*Mironova et al.*, 2015; *Seppälä et al.*, 2014; *Ward et al.*, 2021). The process

begins with the oceans absorbing solar radiation, leading to evaporation and precipitation, thereby influencing winds and oceanic and atmospheric circulations. This direct solar impact on the Earth's atmosphere is known as a bottom-up mechanism since it starts from the Earth's surface.

In contrast, SSI refers to the atmospheric impact predominantly from solar UV rays (*Seppälä et al.*, 2014; *Ward et al.*, 2021). As discussed before, O_3 is a source of heat generation in the middle atmosphere through the absorption of solar UV rays. This creates temperature gradients that are stabilised through winds that affect lower atmospheric layers. Thus, the effect of SSI starts from the top and affects the surface level and, therefore, is called a top-down mechanism. SSI is a function of the solar cycle and has been included in CMIP6 along with TSI and particle forcing as input for the model runs (*Ward et al.*, 2021).

4.2.2 Solar Particle Forcing

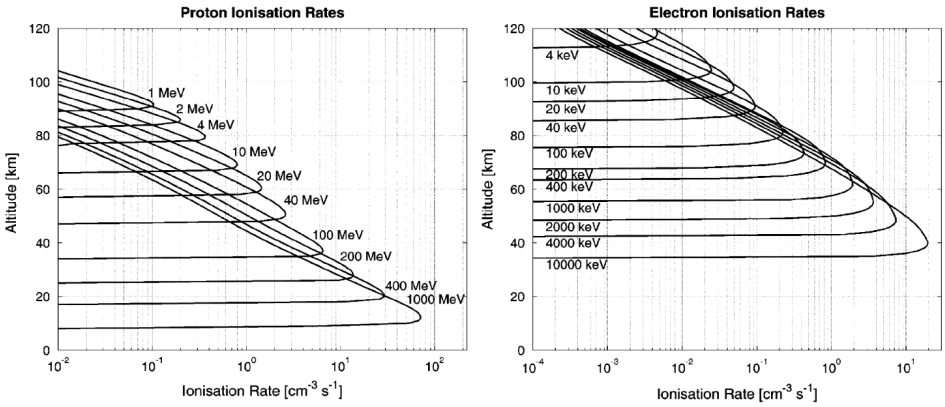

Figure 4.2: Atmospheric ionisation heights of protons (left) and electrons (right) with the variation of its energy. Notice the depth of penetration is a function of the particle's energy. Source: Turunen et al. (2009)

In addition to solar photons, EPP is a major source of energy deposition in the upper and middle atmosphere (*Fang et al.*, 2008; *Mironova et al.*, 2015; *Nesse Tyssøy et al.*, 2022). A typical EPP profile consists of auroral and radiation belt protons of energy 1 MeV to 100s MeV and electrons of energy 1 keV to 1 MeV (*Turunen et al.*, 2009). As seen in Figure 4.2, the higher the energy of the precipitating particle, the deeper it reaches in the atmosphere. Solar Proton Events (SPEs) associated with CMEs are one of the main sources of proton precipitation. They have been linked with strong chemical changes and direct heating of the Earth's upper atmosphere and have been extensively studied (*Cane et al.*, 2003; *Jackman et al.*, 2014; *Nesse Tyssøy and Stadsnes*, 2015; *Sinnhuber et al.*, 2012). In contrast, electron precipitation regions are more structured, varying with geomagnetic latitude and magnetic local time(*Rodger et al.*, 2010; *Tyssøy et al.*, 2019). Until recently most of the focus on understanding electron precipitation effects on the atmosphere has been directed towards auroral electron (≈1–30 keV) precipitation (*Garcia et al.*, 2007; *Lummerzheim*, 1992; *Roble and Ridley*, 1987). Lately, understanding the intensity and morphology of the radiation belt electron precipitation, as well as its subsequent atmospheric impact has received increased attention (*Babu*

et al., 2022; *Nesse Tyssøy et al.*, 2022; *Pettit et al.*, 2019; *Salice et al.*, 2023; *Smith-Johnsen et al.*, 2017, 2018; *Zawedde et al.*, 2016, 2019; *Zúñiga López et al.*, 2022).

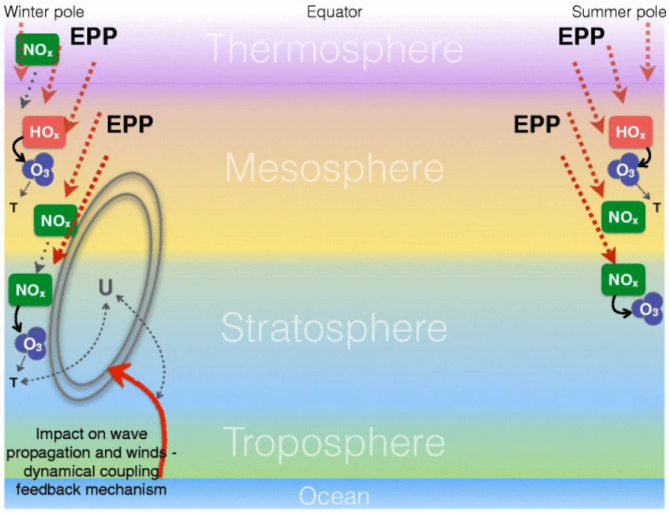

Figure 4.3: An illustration of direct and indirect impacts of EPP on the atmosphere. Note that the polar regions are the hot spots for the production and transport of NO_x and HO_x gases that catalytically destroy ozone. Direct chemical impacts are the black arrows, while transport processes are grey dotted lines, and coupling mechanisms are grey dashed lines. Source: Seppälä et al. (2014)

Atmospheric impact of MEE precipitation is not well understood and inadequately represented in current climate models (*Andersson et al.*, 2014; *Nesse Tyssøy et al.*, 2022; *Rozanov et al.*, 2012; *Seppälä et al.*, 2014; *Szelag et al.*, 2022; *Tyssøy et al.*, 2019; *Ward et al.*, 2021). Precipitating MEE affects the atmosphere through local production amplification of odd nitrogen ($NO_x : N, NO, NO_2$) and odd hydrogen ($HO_x : H, OH, HO_2$). This is called the direct effect of EEP. HO_x are produced at the mesospheric altitudes and have the potential to create imbalances in the ozone distribution there (*Andersson et al.*, 2012; *Verronen et al.*, 2011; *Zawedde et al.*, 2019; *Zúñiga López et al.*, 2022). NO_x are produced by auroral particles and MEE in the lower thermosphere and lower mesosphere. Due to its long lifetime in the absence of photolysis, it can be transported down to the stratosphere by the residual winter circulation (*Funke et al.*, 2014; *Rozanov et al.*, 2012) where it destroys ozone, which plays a vital role in the thermal profile of the stratosphere as seen in Section 4.1. This influence on the atmosphere through transport is called the indirect effect of EEP. Several studies (*Damiani et al.*, 2016; *Maliniemi et al.*, 2021; *Randall et al.*, 1998, 2005; *Solomon et al.*, 1982) have found strong links between MEE and regional destruction of stratospheric ozone. Temperature gradients created by the change in ozone concentration affect atmospheric dynamics and these effects might map down to the troposphere and affect surface-level climate (*Baumgaertner et al.*, 2011; *Maliniemi et al.*, 2019; *Seppälä et al.*, 2009). However, the lower atmospheric impacts of MEE precipitation are only observed so far during the winter season and the surface impacts on regional scales. The spatial extent of radiation belt precipitation and its magnitude are still not quantified accurately (*Nesse Tyssøy et al.*, 2022). The objective of this thesis is to make an important step towards a more realistic incorporation of the MEE in climate models.

4.3 The ApEEP Model

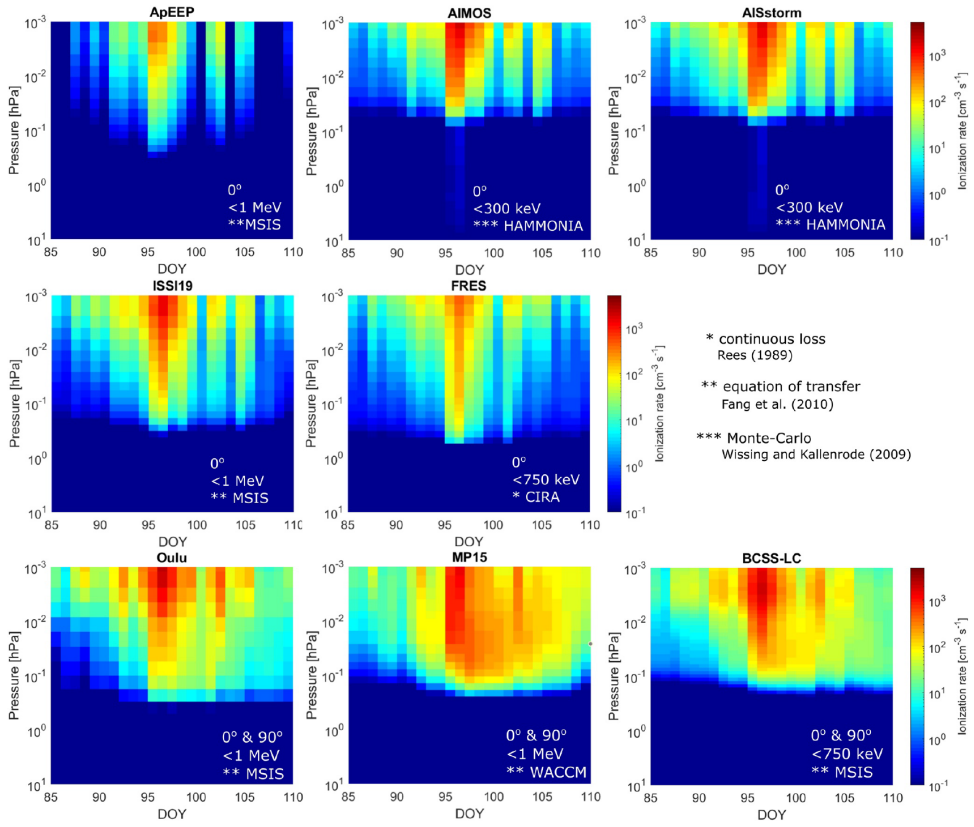

Figure 4.4: A comparison by Nesse Tyssøy et al. (2022) of atmospheric ionisation rates of MEE precipitation predicted by different models. Notice the difference in intensity and duration of atmospheric ionisation between models that use only the 0° MEPED detector and models that use a combination of 0° and 90° MEPED detectors.

van de Kamp et al. (2016) and the updated study *van de Kamp et al.* (2018) have used the nominal >30 keV flux measurements from the MEPED 0° electron detector to develop an atmospheric ionisation model from MEE precipitation. They modelled >30 keV integral electron flux as a function of L-shells and Ap index. The Ap index represented the location of the plasmapause (*Moldwin et al.*, 2002; *O'Brien and Moldwin*, 2003), an important location for wave activity in the magnetosphere as discussed in Section 3.4. The L-shell values are related to magnetic latitudes as,

$$\cos^2 \lambda = L^{-1} \tag{4.1}$$

where λ is the magnetic latitude and L is the L-shell value (*Baumjohann and Treumann*, 1996).

Shekhar et al. (2017) and *Gasque et al.* (2021) also used the MEPED 0° electron telescope measurement to study the spatial extent of >800 keV electron precipitation. However, *van de*

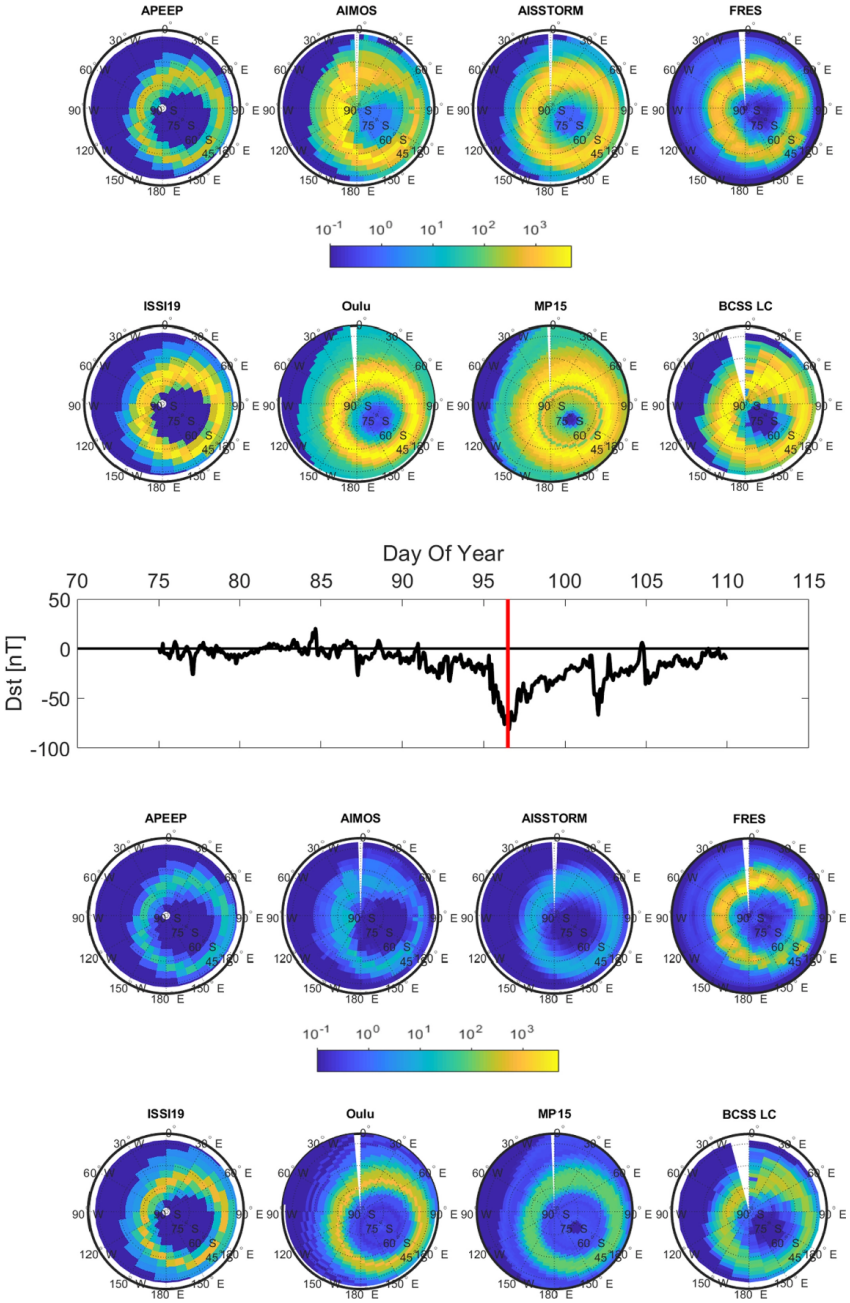

Figure 4.5: A comparison by Nesse Tyssøy et al. (2022) of the spatial extent of atmospheric ionisation rates of MEE precipitation predicted by different models during a main storm phase (April 6, 2010). The top and bottom panels represent pressure levels 0.01 hPa (≈80 km) and 0.1 hPa (≈64 km), respectively. The geomagnetic activity level is represented by the red vertical arrow across the Dst plot in the middle panel. The spatial extent of the ApEEP model is noticeably lower than the BLC data used in this thesis.

Kamp et al. (2016)'s Ap-based model (referred to as ApEEP model from hereon) remains the first and only MEE ionisation model to be included in CMIP6 to account for solar particle forcing (*Matthes et al.*, 2017; *Nesse Tyssøy et al.*, 2022).

It is, however, debated to what extent the ApEEP model gives a realistic representative MEE flux level (*Clilverd et al.*, 2020; *Mironova et al.*, 2019; *Nesse Tyssøy et al.*, 2022; *Pettit et al.*, 2019; *Sinnhuber et al.*, 2022; *Tyssøy et al.*, 2019). Figures 4.4 and 4.5 show a comparison of different MEE atmospheric ionisation models in the High Energy Particle Precipitation in the Atmosphere (HEPPA) III-based intercomparison study by *Nesse Tyssøy et al.* (2022). The study found that the ApEEP model predicts a narrower extent of MEE precipitation and resulting atmospheric ionisation levels compared to other models, including the Birkeland Centre for Space Science's Loss Cone (BCSS-LC) data used in this thesis. As seen in Figure 4.4, models that rely solely on the MEPED 0° detector, especially the ApEEP model show weaker ionisation rates than the models that utilise both 0° and 90° MEPED detectors, such as the BCSS-LC. Furthermore, Figure 4.5 illustrates the narrower spatial extent of the ApEEP model during the main phase of a geomagnetic storm, compared to the BCSS-LC model. Figures 6 and 8 in *Nesse Tyssøy et al.* (2022) show the narrower extent of the ApEEP model remains during the pre-storm and post-storm phases as well. The HEPPA III intercomparison study, therefore, suggests the differences in MEE energy deposition are not just dependent on the variation in intensity and duration of MEE events, but also due to the underestimation of precipitating MEE fluxes and the spatial extent of MEE precipitation.

Chapter 5

Data and Methodology

This chapter introduces geomagnetic indices, solar wind parameters, and the Medium Energy Proton Electron (MEPED) detector onboard the Polar Orbiting Environmental Satellites (POESs) of the National Oceanographic and Atmospheric Administration (NOAA) and the Meteorological Operational (MetOp) satellites of the European Organisation for the Exploitation of Meteorological Satellites (EUMETSAT). The MEPED detector has two telescopes, both having limitations on how accurately they quantify particles inside the atmospheric loss cone. This chapter introduces a newly derived method of estimating precipitating MEE and how this data can be used to identify the spatial extent of MEE precipitation.

5.1 Geomagnetic Indices

Geomagnetic indices are measurements of the Earth's magnetic field perturbations resulting from interaction with the solar wind and the IMF. The geomagnetic indices are estimated from ground-based magnetometers. The most relevant geomagnetic indices (for this thesis) are as follows:

- **Planetary K (Kp) Index**

  The Kp index has a quasi-logarithmic scale from 0 to 9, 0 being calm and 9 indicating an extreme geomagnetic storm. It is estimated from measurements of the horizontal component of the Earth's magnetic field. It is calculated by performing a 3-hour mean of the measured K-values from 13 different mid-latitude magnetometer stations. The Kp index is considered a measure of magnetospheric convection (*Thomsen*, 2004). Another widely used K-index is the **Ap index**, which is derived from Kp by converting it to a linear scale and taking the daily mean. Both Kp and Ap indices are widely used in modelling auroral ovals (e.g. *Elliott et al.*, 2013) and to predict the location of the plasmapause (*Moldwin et al.*, 2002; *O'Brien and Moldwin*, 2003), which forms the basis for the ApEEP model as discussed in Section 4.3.

- **AE Index**

  The Auroral Electrojet (AE) index is a measure of the changes in the horizontal component of the Earth's magnetic field due to magnetic activity in the auroral zone arising from amplified ionospheric currents (*Davis and Sugiura*, 1966). The AE magnetometer stations are located in the northern hemisphere; therefore, the index represents the activity only in the northern hemisphere. This index is calculated by the following steps: First, the mean value of the 5 quietest days in a month for each station (10-13 stations

in total) is determined. Second, this base value is subtracted from the 1-minute data at each station during that month. This calculation's largest and smallest result gives the **AU** and **AL** indices, respectively, expressed in nT. Finally, we get the AE index as $AE = AU - AL$. AU represents the strongest current intensity of the electroject flowing eastward, and AL represents the same for the electroject flowing westward. AE is considered a representation of both.

- **Dst Index**

  The Disturbance storm-time (Dst) index, as its name suggests, is a measure of disturbance in the horizontal component of the Earth's magnetic field due to enhancement of the ring current (mentioned in the description of Figure 2.6). The four magnetometer stations that measure the H-component are located at low latitudes to minimise interference from auroral and equatorial electrojets. The Dst index is calculated by performing a weighted average of the H-component's hourly deviation from its quiet level. The unit is in nT, the same as the AE index.

  Geomagnetic storms are often classified in terms of the Dst index. If the hourly $Dst < -50\ nT$, it is a weak storm, if $-50\ nT \leqslant Dst < -100\ nT$, a moderate storm, if $-100\ nT \leqslant Dst < -200\ nT$, a strong storm, if $-200\ nT \leqslant Dst < -350\ nT$, a severe storm and in rare cases, $Dst \leqslant -350\ nT$ that corresponds to great storms (*Loewe and Prölss*, 1997). There are also extremely scarce events like the 1859 Carrington event that wreaked havoc across the planet, which had a $Dst < -1000\ nT$ (*Siscoe et al.*, 2006; *Tsurutani et al.*, 2003).

  A geomagnetic storm can be divided into three phases based on the Dst index. The initial phase, also known as the storm sudden commencement (SSC), marks the compression of the magnetopause from a sudden increase in the dynamic pressure of the solar wind. The Dst index turns positive in this phase. This is followed by the main phase of the storm, during which the Dst reaches a maximum negative value, and finally, the recovery phase, which lasts several hours to several days, during which the Dst returns to its baseline/quiet-time value. The three phases are represented in Figure 5.1. However, the SSC doesn't always mark the beginning of a geomagnetic storm (*Curto et al.*) as solar wind dynamic pressure can increase without creating a geomagnetic storm.

  The Dst index often includes contributions from other currents in the magnetosphere, such as the magnetopause current and the tail current. The pressure-corrected Dst index (**Dst***) removes the magnetopause current induced by the solar wind dynamic pressure (P) and gives a more accurate representation of the ring current (*Burton et al.*, 1975):

$$Dst^* = Dst - (15.8 \times P^{0.5}) + 20 \tag{5.1}$$

- **RC Index**

  Although the Dst index is the commonly used representation of the ring current and geomagnetic storm strength, its baseline is known to change with the solar cycle (*Lühr and Maus*, 2010; *Olsen et al.*, 2005; *Temerin and Li*, 2015). This can lead to the Dst index underestimating or overestimating geomagnetic activity with the solar cycle, which makes it difficult to use in quantitative modelling on decal scales. In such instances, the Ring Current (RC) index can be used as an alternative indicator of the Dst index (*Lüehr et al.*, 2016).

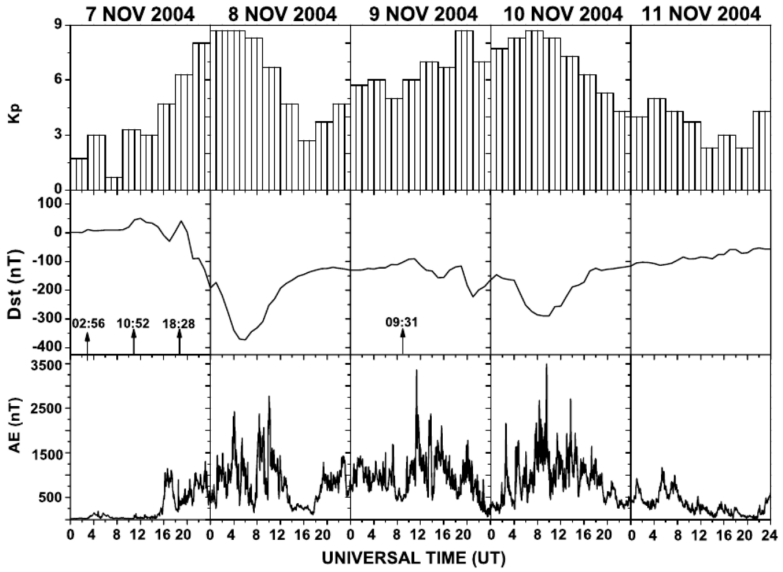

Figure 5.1: A comparison of variations of Kp, Dst, and AE indices during 7th to 11th of November 2004. The vertical arrows with timestamps on the middle panel represent the sudden storm commencement times. Source: Sahai et al. (2009)

The RC index was introduced by *Olsen et al.* (2014) to represent quiet-time contributions of the magnetosphere when modelling the Earth's magnetic field. It is derived from an hourly spherical harmonic analysis of measurements from around 14 magnetometer stations in mid and low latitudes around the world (see the Data section in Paper II for a complete description of its derivation).

5.2 Solar Wind Parameters

Solar wind parameters are quantities that are used to describe the properties of the solar wind. They are typically measured by spacecraft (such as the ACE, SOHO, Wind, and Parker Solar Probe) monitoring the Sun and the solar wind orbiting around the Earth or in interplanetary space. Some of the relevant (to this thesis) solar wind parameters are the following:

- **Flow Speed**: Speed of the solar wind plasma, measured in km/s.
- **Density**: Solar wind proton density, measured in n/cc.
- **Pressure**: Solar wind flow pressure, measured in nPa.
- **Temperature**: Solar wind proton temperature, measured in K.
- **IMF**: The IMF is a vector quantity containing 3 components when expressed in Geocentric Solar Ecliptic (GSE) and the Geocentric Solar Magnetic (GSM) coordinate systems. B_x, the magnetic field directed along the x-axis aligned with the Sun-Earth line, B_z, the magnetic field pointing north along the Earth's dipole axis, and B_y, the magnetic field pointing perpendicular to both B_x and B_z, completing a right-handed Cartesian coordinate system. All IMF components used in this thesis are expressed in GSM coordinates.

- **Electric Field**: Solar wind electric field E_y, measured in mV/m. E_y is a derived quantity, calculated as the product of IMF B_z and the solar wind speed.

5.3 MEPED Instrument

As mentioned in Section 4.2.2, the accurate quantification of MEE precipitation remains elusive since most particle detectors to date in orbit have inadequate pitch angle resolution to measure precipitating MEE accurately (*Nesse Tyssøy et al.*, 2016, 2022; *Rodger et al.*, 2013). The MEPED instrument is a part of the Space Environment Monitor (SEM) package that also contains the Total Energy Detector (TED) that measures 0.5–20 keV electrons and protons in the auroral energy range (*Evans and Greer*, 2000). The SEM package has been measuring particles since 1978. As of 2023, it is still operational, covering a bit over 4 solar cycles, making it the longest observation of trapped radiation belt particles from space. This large coverage makes the instrument ideal for studying MEE precipitation and its dependence on solar activity. The first generation SEM-1 instrument was upgraded in 1998 with the launch of NOAA-15. From NOAA-15 onwards, the second generation SEM-2 remains the main instrument to date.

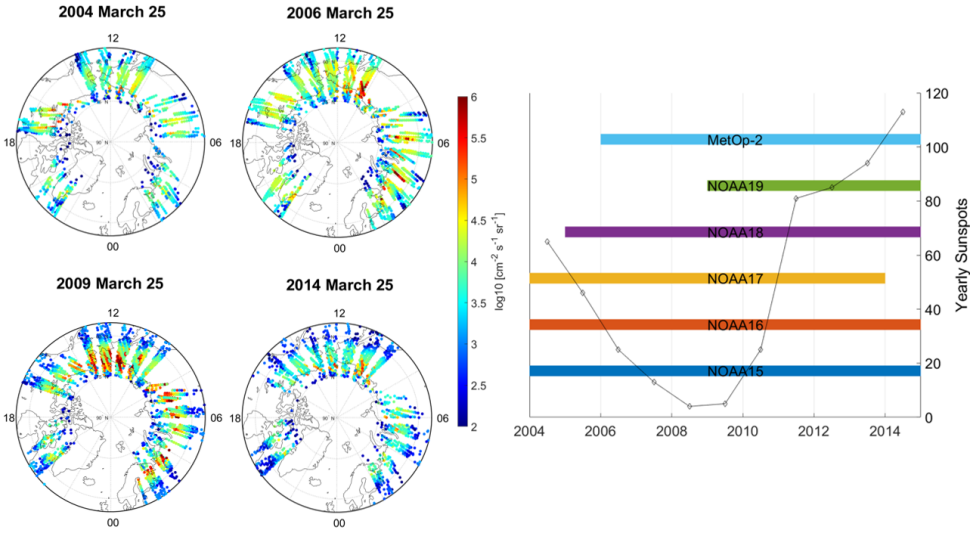

Figure 5.2: (left) Satellite ground-track with daily MEPED BLC flux measurements of >43 keV electrons during 25th of March 2004, 2006, 2009 and 2014. (right) Satellites operational during 2004–2014, the 11-year solar cycle period of the investigation that forms this thesis. Sunspot numbers are the grey dotted line indicated on the right side y-axis. This figure was published in Paper I (Babu et al., 2022) and Paper IV (Tyssøy et al., 2021).

The POES and MetOp series are Low Earth Orbit (LEO) satellites at 800–850 km from the surface of the Earth. They have a circular sun-synchronous polar orbit with an orbital period of ≈102 minutes (*Evans and Greer*, 2000). Their ground tracks remain fairly steady except for NOAA-15 and NOAA-16, which exhibited drift in their orbital plane during their operational time (*Sandanger et al.*, 2015). The satellites have a stabilised spatial orientation that allows them to monitor trapped and precipitating radiation belt particles near the foot of the field lines (*Nesse Tyssøy et al.*, 2016; *Rodger et al.*, 2010). The MEPED instrument consists of an

omnidirectional system that measures protons of energy >16 MeV, a two-directional proton detector, and a two-directional electron detector. This thesis concerns only the two-directional electron detector, and the reader may find more information about the two-directional proton instrument and the omnidirectional instrument in *Evans and Greer* (2000); *Nesse Tyssøy et al.* (2016); *Sandanger et al.* (2015); *Yando et al.* (2011) *and references therein*.

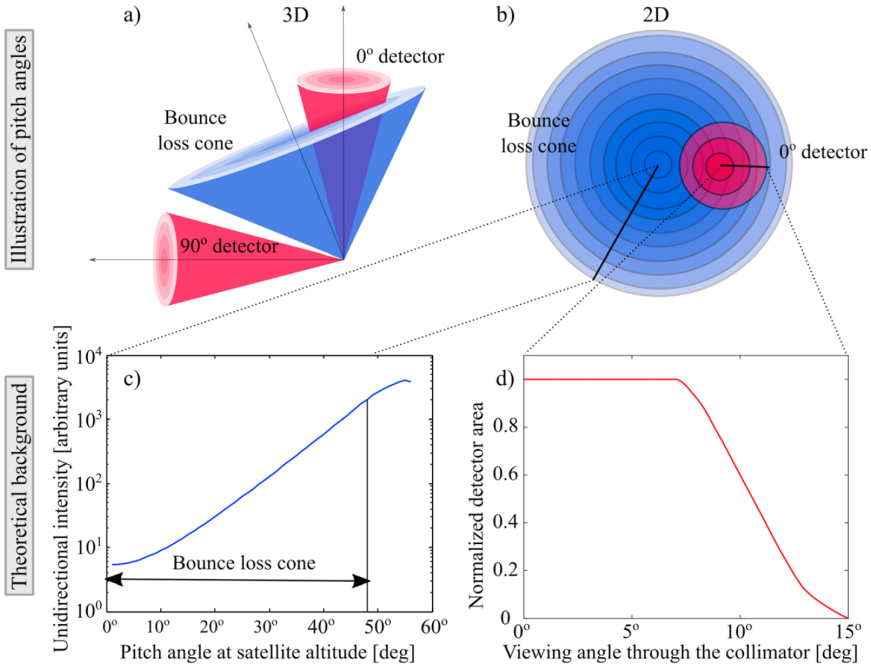

Figure 5.3: Nesse Tyssøy et al. (2016)'s illustration of the two-directional part of the MEPED detector. (a) A 3D view of the electron telescopes with respect to the atmospheric bounce loss cone. The line passing through the centre of the loss cone is the local magnetic field line. (b) A 2D view of the same, showing how much of the bounce loss cone the 0° telescope covers at high latitudes. (c) Theoretical pitch angle distribution inside the bounce loss cone based on the Fokker-Planck equation for particles. (d) The detector's output signal vs viewing angle of the radiation passing through the detector collimator.

The MEPED electron telescopes consist of three energy channels to measure the integral flux of MEE. They are E1, E2, and E3 measuring nominal energy values >30 keV, >100 keV and >300 keV, respectively. However, the detector efficiency depends on the incident electron spectrum (*Yando et al.*, 2011). *Ødegaard et al.* (2017) estimate new effective integral energy limits > 43, > 114, and > 292 keV and associated geometric factors based on a series of realistic power law and exponential spectra applying *Yando et al.* (2011)s modelled detector response. Additionally, electron telescopes are known to respond to 210–2600 keV protons (*Evans and Greer*, 2004; *Yando et al.*, 2011). Moreover, the solid-state detectors exhibit noticeable degradation of the proton detection efficiency after 2–3 years of operation due to radiation damage (*Asikainen and Mursula*, 2011; *Galand and Evans*, 2000; *Sandanger et al.*, 2015). The false proton detection rate is removed from the electron measurements using the proton telescope readings, and the detector degradation is accounted for by using correction factors obtained by *Sandanger et al.* (2015) and *Ødegaard et al.* (2016). A detailed explanation of both procedures

is given in *Nesse Tyssøy et al.* (2016).

The MEPED electron detector consists of a 0° telescope and a 90° telescope as seen in Figure 5.3(a). The 0° telescope is mounted to point toward the local zenith at any point during the satellite's orbit, and it measures electrons towards the centre of the BLC at higher latitudes as seen in Figure 5.3(b). The 90° detector is mounted perpendicularly to the 0° detector and antiparallel to the spacecraft's velocity vector. The 90° detector measures trapped radiation belt electrons inside and outside the BLC (*Evans and Greer*, 2000; *Meredith et al.*, 2011; *Nesse Tyssøy et al.*, 2016; *Rodger et al.*, 2010).

As discussed in Section 3.2, the pitch angle of a trapped radiation belt particle determines if it gets lost to the atmosphere or not. The spatial distribution of pitch angles or the Pitch Angle Distributions (PADs) varies with particle energy, location, and geomagnetic activity. In the main phase of storms, strong pitch angle diffusion may cause instances of isotropic PADs. Then both the 0° and 90° detectors observe the same level of MEE fluxes (*Nesse Tyssøy et al.*, 2016). However, PADs are commonly anisotropic with decreasing fluxes towards the centre of the BLC, causing the 0° detector to underestimate and the 90° detector to overestimate the precipitating fluxes. Therefore, the use of either a 0° or 90° detector alone for a precipitating MEE study may lead to inaccurate results. In this thesis, the BLC fluxes obtained by *Nesse Tyssøy et al.* (2016) are used to achieve more realistic estimates: The fluxes from both the 0° and the 90° telescopes are combined with the electron PADs from the theory of wave-particle interactions in the magnetosphere. The Fokker-Planck equation for particle diffusion is solved (*Kennel and Petschek*, 1966; *Theodoridis and Paolini*, 1967) for a range of diffusion coefficients (*Nesse Tyssøy et al.*, 2016). The solutions are then transformed to the altitude of the satellite and stored in a lookup table. Then, knowing the detectors pointing direction relative to the magnetic field the ratio between the fluxes detected by the 0° and 90° detectors are calculated, and the corresponding ratio for the theoretical solution is determined. The determination of the PAD is done for each energy channel as the level of particle diffusion varies with energy. The size of the BLC is predicted based on the International Geomagnetic Reference Field (IGRF) model. More information about this method can be found in *Nesse Tyssøy et al.* (2016). The BLC reading of >43 keV electrons and the operational satellites carrying the MEPED instrument during 2004–2014 are shown in Figure 5.2.

5.4 Boundary Identification using BLC Data

Papers I, II, and III use latitude boundaries of precipitating MEE identified from MEPED BLC electron fluxes. This section describes the procedure for boundary identification. The process is the same for the Northern Hemisphere (NH) and the Southern Hemisphere (SH).

The process starts off by binning daily resolved BLC fluxes into 180° latitudes and 8 Magnetic Local Time (MLT) sectors, resulting in 1° latitudinal and 3 hr MLT resolution. We use the International Geomagnetic Reference Field (IGRF)'s Altitude-Adjusted Corrected Geomagnetic (AACGM) coordinate system, which will be denoted as CGMLat throughout this thesis. Then we define a background flux threshold of mean plus two standard deviations of fluxes in 50°– 60° CGMLat region during ambient/slow solar wind conditions. This threshold value is calculated separately for the E1, E2, and E3 energy channels. The fluxes are then fitted with a smoothing spline, and the local maxima and minima are identified. The minima and maxima are used as reference points to find the CGMLat at which the spline crosses the threshold with a positive gradient. The point of crossing is stored as the equatorward boundary (marked by the blue arrow in Figure 5.4). During moderate to high geomagnetic activity days, we observed multiple peaks over the threshold, indicated by the black box in Figure 5.4 and

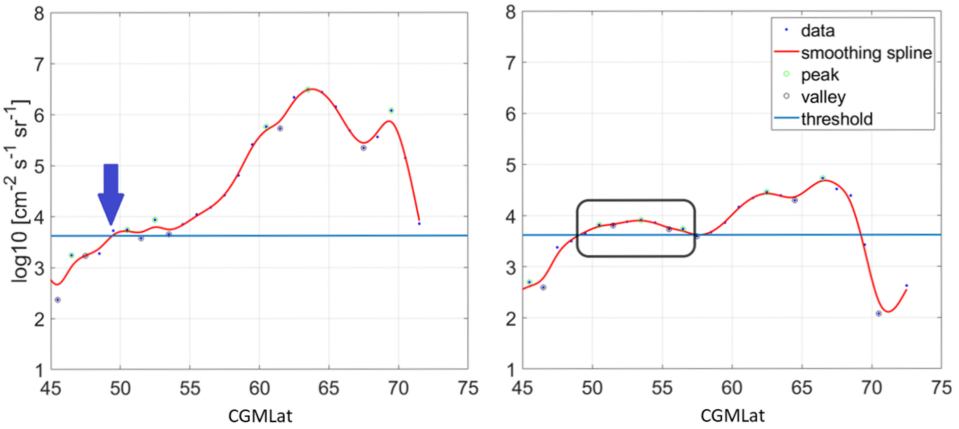

Figure 5.4: (left) BLC electron flux in NH for a sample day with one peak above the threshold. The blue arrow marks the latitude of the threshold crossing. (right) The same plot for a different day in the NH with a double peak over the threshold. The black box indicates a slot region filling event. This figure is used in Paper I (Babu et al., 2022)

5.5. These peaks observed at lower latitudes correspond to *Kavanagh et al.* (2018)'s slot region filling events discussed in Section 3.3. The slow decay of slot region electrons is not well correlated with any geomagnetic indices or solar wind parameters. Therefore, we do not consider them as a part of dynamic MEE boundaries. The days following slot region filling events usually consist of conditions where it is difficult to separate the dynamic boundary from the CGMLats corresponding to the slot region in the radiation belt and are therefore removed from the data set. A table of these ambiguous days observed in both hemispheres is given in Appendix A.2 and A.1. They account for 12% of the total days during 2004–2014 in the NH and 16% of the total days during the same period in the SH.

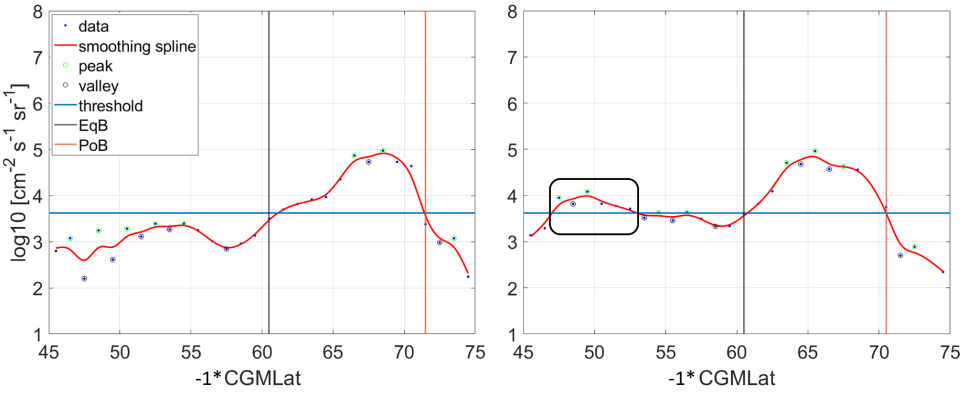

Figure 5.5: BLC electron fluxes in the SH. (left) A sample day with one peak over the threshold and (right) a sample day with a dual peak over the threshold. The grey vertical lines mark the equatorward boundary (EqB), and the orange vertical lines mark the poleward boundary (PoB) in both plots. The black box on the right figure represents a slot region filling event.

The BLC flux data has a sharp cut-off at 75° CGMLat in both the NH and SH as the PAD

transformation from the equator is challenging at high L-shells based on the IGRF model. This makes it difficult to identify the poleward boundary. However, the algorithm identifies poleward boundaries for days when the smoothing spline crosses the threshold after the equatorward boundary latitude with a negative gradient. The orange vertical lines in Figure 5.5 represent the poleward boundaries.

Chapter 6

Summary of Papers

This chapter provides the summaries of five papers that form this thesis. Papers I-III address the primary objective of modelling the spatial extent of the MEE precipitation. These three papers initiate an essential step towards a better understanding of radiation belt precipitation and the underlying mechanisms. Papers IV and V add knowledge on the intensity, flux response, timing, and duration of MEE precipitation. Together, the five papers constitute an overall picture necessary for an accurate MEE parameterization that can be implemented in future climate models to quantify a more realistic atmospheric response to particle precipitation.

Paper I: **Determining Latitudinal Extent of Energetic Electron Precipitation Using MEPED On-Board NOAA/POES**

Authors: Eldho Midhun Babu, Hilde Nesse Tyssøy, Christine Smith-Johnsen, Ville Maliniemi, Josephine Alessandra Salice, Robyn M. Millan, Ian G. Richardson. Year: 2022, Journal: JGR Space Physics, Volume 127

Paper I develops a geomagnetic index-based model that predicts the spatial extent of MEE precipitation using the daily resolved BLC flux data. The BLC flux data have been developed by *Nesse Tyssøy et al.* (2016) combining measurements of the 0° and 90° electron telescopes of the MEPED instrument onboard the POES/MetOp satellites of NOAA/EUMETSAT.

To achieve the objective, we investigate BLC flux data during 2004–2014, covering a full solar cycle. Equatorward boundaries are identified in the northern hemisphere from the BLC data using the methods described in Chapter 5 Section 5.4. We investigate which geomagnetic index or solar wind parameter gives the best correlation with the identified boundaries. Out of pressure-corrected Dst (Dst*), Kp, AE, Ap, Bz, By, Ey, solar wind flow pressure, and solar wind flow speed, Dst* gave the best correlation. The equatorward boundary was parameterized by fitting least squares regression on Dst*. This model was able to predict the equatorward boundary for >43 keV, >114 keV and >292 keV electron precipitation in Magnetic Local Time (MLT) sectors 0–18.

The Dst* model exhibited high accuracy with 80% of the residuals (*model – identified boundaries*) falling within $\pm 2.2°$ geomagnetic latitude. However, we observed a solar cycle bias in the model resulting from quiet time baseline variation of the Dst index (*Temerin and Li*, 2015). We also observed that the model produced the highest accuracy during days in which High-Speed solar wind Streams (HSSs)/Corotating Interaction Regions(CIRs) dominated the near-Earth space compared to days with Coronal Mass Ejections (CMEs) and slow/ambient solar winds conditions. The modelled equatorward boundaries showed minimal variations across

different MLT sectors and we speculated the MEE completing multiple orbits around the Earth in a day is the reason for this minimal variation. A comparison with *Moldwin et al.* (2002)'s plasmapause location (L_{pp}) shows the >43 keV electron precipitation boundary deviates greatest from L_{pp} during days with CMEs and deviates the least during days with slow/ambient solar wind conditions.

Paper II: **An Updated Geomagnetic Index-based Model for Determining the Latitudinal Extent of Energetic Electron Precipitation**

Authors: Eldho Midhun Babu, Hilde Nesse, Spencer Mark Hatch, Nils Olsen, Josephine Alessandra Salice, Ian G. Richardson. Year: 2023, Journal: JGR Space Physics

Paper II improves the accuracy of the Dst* model from Paper I that predicts the equatorward extent of >43 keV, >114 keV and >292 keV electron precipitation. The same daily resolved BLC flux data developed by *Nesse Tyssøy et al.* (2016) has been used in this analysis. The solar cycle bias that existed in the Dst* model has been removed by the multiple linear regression (MLR) model with Dst* and pressure-corrected Ring Current (RC) index, RC*, as the predictor variables. The RC* index mitigated the baseline variation of Dst* index with the solar cycle. The MLR model depending on whether the near-Earth space is dominated by CME, HSS/CIR or slow/ambient solar wind outperformed the MLR model independent of the solar wind conditions. The error estimate has been reduced from approximately $\pm 2.24^{\circ}$ CGMLat in the Dst* model to eighty percent of the residuals lying within 1.80° CGMLat to -1.77° CGMLat in the solar wind structure dependent MLR model.

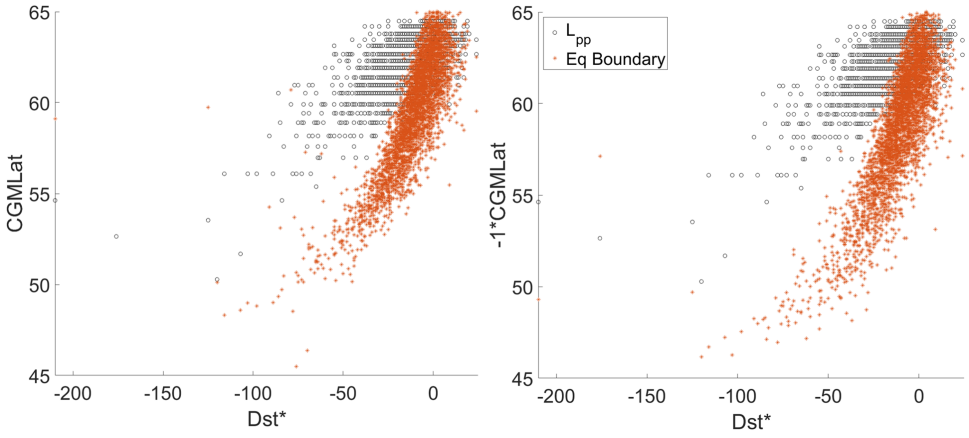

Figure 6.1: A comparison of Moldwin et al. (2002)'s plasmapause location (L_{pp}), marked as black circles, and the equatorward boundary of >43 keV precipitation from the BCSS-LC, marked as orange asterisks. (left) Northern Hemisphere and (right) Southern Hemisphere. Pressure-corrected Dst index on the x-axis of both plots is a proxy to the level of geomagnetic activity.

The MLR model is then extended to the Southern Hemisphere (SH) after removing MEPED data between 270° and 50° geomagnetic longitude, the region of South Atlantic Anomaly (SAA). Similar to the northern hemisphere, RC* index gave the best correlation with identified boundaries, followed by Dst*, Kp, and AE indices, respectively. The solar wind-dependent MLR model gave a slightly lower accuracy in the SH with eighty percent of

the residuals lying within 1.99° CGMLat to −1.98° CGMLat.

Figure 6.1 is a comparison of the Ap-based plasmapause location (L_{pp}) used in the ApEEP model with the equatorward boundaries of >43 keV precipitation obtained from the MLR model. This figure illustrates the greater spatial extent of MEE precipitation as predicted by the MLR model in both the NH and SH. Additionally, *Laundal et al.* (2017) found a significant deviation of the Earth's magnetic dipole field structure at ionospheric heights resulting in hemispheric asymmetries on how the magnetosphere is coupled with the ionosphere and the thermosphere. *Kilifarska* (2017) also found that the inter-hemispheric asymmetries lead to a different atmospheric response to particle precipitation. These two studies imply that an independent model predicting the spatial extent of MEE precipitation is necessary for accurate quantification of global atmospheric response to MEE precipitation. If implemented in atmospheric climate models such as CMIP, a model that predicts the spatial extent of MEE precipitation on both hemispheres using the BCSS-LC would output a higher impact of solar particle forcing on the Earth's atmosphere.

Paper III: **Energetic Electron Precipitation during Slot Region Filling Events**

Authors: Hilde Nesse, Eldho Midhun Babu, Josephine Alessandra Salice, and Bernd Funke. Year: 2023, Journal: JGR Space Physics

Paper III investigates the occurrence rate, duration, and local time dependence of slot region filling events using Bounce Loss Cone (BLC) flux observations from the NOAA/POES over a full solar cycle from 2004 to 2014. The slot region is located between the inner and outer radiation belts and is usually empty during geomagnetically quiet periods. This region marks the equatorward boundary of the energetic electron precipitation (EEP) but often gets filled during moderate to high geomagnetic activity. EEP from the slot region is a missing energy input in the current precipitation estimates scaled by geomagnetic indices. The objective of this study is to examine the spatial extent, energy dependence, frequency, duration, and the atmospheric response of EEP associated with slot region filling events.

The study finds the occurrence rate of slot region filling events to be energy dependent with 65, 56, and 32 identified events associated with >43 keV, >114 keV, and >292 keV MEEs, respectively. The occurrence rate is also solar cycle-dependent, with minimal slot region filling events observed during the solar minimum. The indicated drivers for these events are CMEs and/or CIRs/HSSs with >292 keV events most likely associated with CMEs. A superposed epoch analysis of identified slot region filling events reveals that the solar wind speed, IMF Bz, and Ey are quiet before a strong geomagnetic deflection associated with the slot region filling events. This tendency is potentially important for preconditioning the magnetosphere for the following mass convection observed during the storm. Reformation of the slot region happens more efficiently closer to the plasmapause resulting in distinct double EEP bands throughout the recovery period. Maximum flux below 57° CGM latitude (or L< 3) decreases to 25% of the initial level after 13, 14 and 17 days for the >43 keV, >114 keV, and >292 keV BLC fluxes, respectively. The study also indicates a strong MLT dependence with slot region precipitation maximising around the noon to afternoon/evening sector. This is consistent with the pitch angle scattering into the loss cone from plasmaspheric hiss and lightning-induced whistler mode waves.

A superposed epoch analysis of Nitric Oxide (NO) volume mixing ratio (vmr) at 60-70 km altitude from the Michelson Interferometer for Passive Atmospheric Sounding (MIPAS) instrument on board the Envisat satellite was performed to evaluate the potential impact of slot

region precipitation on the atmosphere. The analysis shows that the NO density increases during summer and winter at low latitudes where slot region precipitation dominates. The NO density remains elevated for at least four days after the onset of slot region precipitation independent of the season. It is, however, difficult to determine to which extent the weak precipitating MEE fluxes beyond four days are contributing to the NO production. The study suggests that more research is required to evaluate the potential impact of slot region precipitation on the atmosphere.

Paper IV: The Predictive Capabilities of the Auroral Electrojet Index for Medium Energy Electron Precipitation

Authors: Hilde Nesse Tyssøy, Noora Partamies, Eldho Midhun Babu, Christine Smith-Johnsen, and Josephine Alessandra Salice. Year: 2021, Journal: Frontiers in Astronomy and Space Sciences

Paper IV utilises the same BLC electron flux estimates as papers I-III over the full solar cycle 2004–2014. The fluxes are daily averages weighted equally between the different MLT regions. The fluxes are, however, now averaged over a fixed CGM latitude band from 55° to 70° . The goal is to explore the predictive capability of the AE index on a daily scale in regard to MEE precipitating fluxes. Out of the International Association of Geomagnetism and Aeronomy (IAGA) recognized magnetic indices, the Auroral Electrojet (AE) index best corresponds to substorm activity. Hence, it adds to our understanding of the causal connection between magnetospheric processes and the MEE acceleration and loss in the plasma sheet and radiation belts.

To investigate potential energy dependency, each of the MEPED energy channels, >43, >114, and >292 keV are evaluated independently. Applying a linear regression model, we find a strong correlation between the daily resolved AE index and >43 keV fluxes. Similarly, we find a strong coherence between the daily AE index and the daily number of substorms. Electrons in the respective energy range will be part of the source and seed particles directly injected during substorms. As such, there is a potential physical link between the AE intensity and >43 keV fluxes, even though the >43 keV electrons are expected to play a minor role in the intensity of the electrojets.

The daily AE index is, however, a poor predictor for the >292 keV electrons, where only 22% of the flux variability is described by the daily AE variability. As pointed out below, Paper V shows that these higher energy electrons typically peak 1-2 days after the onset of a geomagnetic storm. The delay suggests that it takes time to accelerate the injected seed electrons into several hundred keV. It will also require a continuous acceleration mechanism, which could be provided during repeated substorm activity. The source particles will fuel VLF waves and the injected seed particles can be energised as they drift across the substorm-induced electric field on the nightside. This implies that MEE precipitation of >292 keV fluxes is a result of both the ongoing and preceding substorm activity. Hence, in Paper IV we examine the link between daily MEE fluxes and the accumulated AE index. We create new AE-based MEE proxies by accumulating the AE activity over multiple days including an e-folding lifetime.

The results indicate that AE-based proxies can predict 72-86% of the detected MEE precipitation variance of on a daily scale at the energies > 43, >114, and >292 keV. 90% of the modelled flux values deviate less than a factor of 2.5 from the observed NOAA/POES MEPED fluxes over the full solar cycle. The independent estimates of the different energies allow for a realistic description of the time-dependent energy spectrum. However, as demonstrated in Pa-

per I-III, the MEEs do not precipitate over a fixed latitude band. However, a refined AE model of the flux intensity combined with the updated MLR model for determining the latitudinal extent, can form a base for a new MEE precipitation model.

Paper V: **Exploring the Predictability of the High-Energy Tail of MEE Precipitation Based on Solar Wind Properties**

Authors: Josephine Alessandra Salice, Hilde Nesse, Eldho Midhun Babu, Christine Smith-Johnsen, Ian G. Richardson. Year: 2023, Journal: JGR Space Physics

Paper V further explores the nature of the high energy tail of MEE ($\geqslant$300 keV). It compares the $>$292 keV to $>$43 keV electron flux variability to better understand the energy spectrum. Using the same data of daily and latitudinal averaged fluxes for the period 2004–2014 as applied in Paper IV, the MEE precipitation is explored in the context of solar wind drivers CIR/HSSs and CMEs, alongside their associated solar wind properties. Three key aspects of $>$292 keV electron fluxes are examined:

- The maximum flux response
- The timing of the maximum flux response
- The duration of the flux enhancement

The goal is to identify parameters that can better represent the flux variability than a model based on purely an averaged response. The listed key aspects are therefore evaluated in terms of the likelihood of a specific outcome.

Unlike Paper IV, which assesses a continuous flux response, Paper V explores the flux response in terms of events. We identify 249 events from 2004 to 2014: 34 CMEs, 181 HSSs, 17 CME + HSSs, and 17 HSS + CMEs. We explore the nature of the fluxes both in superposed epoch analysis, as well as the individual responses.

Linear regression gives a correlation coefficient of 0.89 between the peak fluxes of $>$292 keV and $>$43 keV electrons. Higher correlation with linear regression model targeting the specific solar wind drivers. The epsilon coupling function, however, has a correlation coefficient with the $>$292 keV peak flux of 0.84, independent of solar wind structure. As pointed out above, the $>$292 keV flux peaks 0-3 days after the $>$43 keV flux peaks, where there is the highest probability for a 1-day delay. Interestingly, the predictive capabilities increase when accounting for solar wind speed. The wind speed limits are different for CMEs compared to HSSs. The duration of the $>$292 keV flux enhancement has the highest probability of lasting four days independent of the solar wind driver being CMEs or HSSs.

Previous parametrisations for MEE precipitations are developed based on averaged responses. This implies that if the dependent variable such as a geomagnetic index has a wide range of possible flux responses, an average representation underestimates strong precipitation events and overestimates weak precipitation events. On decadal scales, this might dampen the overall precipitating flux variability. The results of Paper V offer a pathway for developing a parameterisation of MEE precipitation including a stochastic factor. The results could add to the accuracy of a new MEE model.

Chapter 7

Conclusions and Future Prospects

7.1 Conclusions

The overarching objective of this project has been to provide key elements for an MEE precipitation model and add to the scientific understanding of the nature of MEE precipitation. A realistic MEE precipitation model is a key component in understanding the influence of the Sun on the Earth's climate. The primary research work (Papers I-III) of this project was focused on the spatial extent of MEE precipitation. Papers I and II find that the equatorward extent of MEE precipitation (>43 keV, >114 keV and >292 keV) is highly correlated with the indices that represent the ring current (Dst^* and RC^*). A multiple linear regression model with Dst^* and RC^* indices as the independent or predictor variables was able to model the daily equatorward boundaries of MEE precipitation in both the northern and southern hemispheres. The model also depended on whether the near-Earth space was dominated by CME, HSS/-CIR or slow/ambient solar wind conditions. In the northern hemisphere, eighty percent of the residuals were within 1.80° CGMLat to -1.77° CGMLat, while it was within 1.99° CGMLat to -1.98° CGMLat in the southern hemisphere. Paper III investigated the MEE precipitation associated with slot region filling events, which is a missing piece in geomagnetic index-based precipitation models. The study shows that the likelihood of a slot region filling event occurrence is strongly dependent on the solar cycle. It indicates that CMEs are the most probable drivers of slot region filling events for the high-energy tail of the MEE spectrum. However, independent of the solar wind drivers, a pronounced calm before the storm and similar geomagnetic signatures was shown to be a common denominator for the events. The associated precipitation typically lasts from 13 to 17 days depending on the energy, and the low fluxes are sufficiently strong to produce a measurable NO enhancement at low CGM latitudes. Thus, Paper III provides information about the solar wind and geomagnetic characteristics as well as the duration of slot region filling events and the associated MEE precipitation, which could be applied in a future MEE parametrization.

Papers IV and V tackled the challenge of modelling the flux response, duration, and timing of the high energy tail (>292 keV) of MEE precipitation. Both papers highlight the potential time delay of the >292 keV fluxes with respect to >43 keV fluxes. The delay implies that it takes time to accelerate the injected seed electrons into several hundred keV. As such, the AE-based proxies developed in Paper IV are achieved by accumulating the AE activity over multiple days including an e-folding lifetime. This approach was able to predict 72-86% of the detected daily MEE precipitation variance. Paper V finds that the solar wind ε-parameter can predict the peak flux of >292 keV electron precipitation with a Pearson correlation coefficient of 0.84. This study also finds that on average, precipitation of >292 keV electrons last 2-3

days longer than the >43 keV electron precipitation and the high energy tail of MEE precipitation has the highest probability of lasting 4 days during days with CMEs and HSSs/CIRs. Moreover, Paper V provides key variables that increase the predictability for a specific flux response, delay or duration. It paves the way for a stochastic MEE parametrization, which goes beyond the average MEE response, enabling a more realistic flux variability on both daily and decadal scales.

Together, these five papers represent a comprehensive approach to improve the current capabilities of MEE parameterization that can be applied in chemistry-climate models to better answer: What are the effects of EPP on the atmospheric system?

7.2 Future Prospects

7.2.1 The Poleward Boundary

As mentioned in Section 5.4, the boundary identification algorithm detected poleward boundaries when the BLC flux data is available at high latitude and the smoothing spline crosses the threshold with a negative gradient after the equatorward boundary. This corresponds to 77% and 84% of the total days between 2004 and 2014 in the NH and SH, respectively. In contrast, the algorithm identifies equatorward boundaries in 93% and 90% of the total number of days between 2004 and 2014 in the NH and SH, respectively. Both estimates are for >43 keV electron precipitation. Since the BLC flux data have a cut-off at 80° geographic latitude, the higher detection rate of poleward boundary in the SH could be attributed to the offset of the Earth's magnetic dipole field, resulting in more available BLC flux at high latitude SH than in the NH.

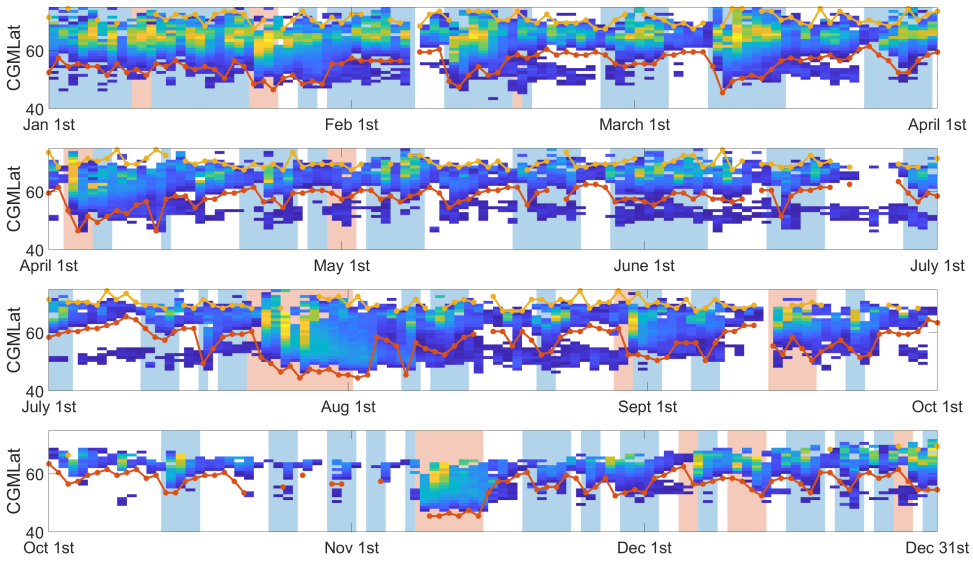

Figure 7.1: Identified equatorward (red) and poleward (yellow) boundaries for >43 keV electron precipitation in the Northern Hemisphere in 2004. Light red bars represent days with CMEs, light blue bars are days with CIRs/HSSs and white bars are days with ambient/slow solar wind conditions. The heat map represents fluxes above the threshold (described in Chapter 5 Section 5.4).

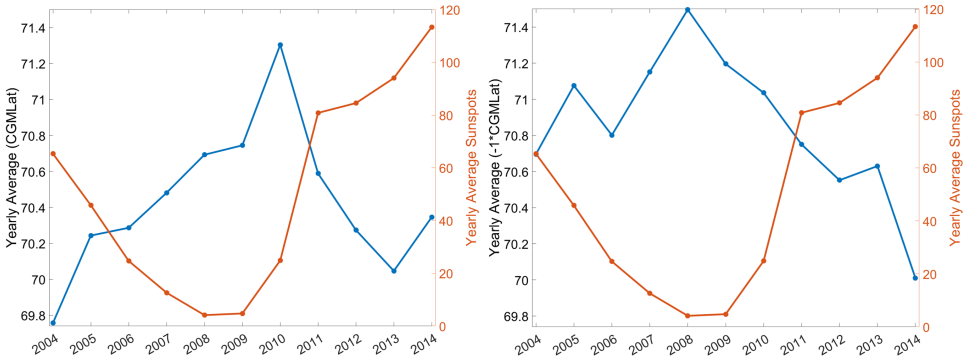

Figure 7.2: Variation of the yearly mean poleward boundary with respect to solar activity (represented by sunspot numbers on the right y-axis). [left] Northern Hemisphere and [right] Southern Hemisphere.

As seen in Figure 7.1, the poleward boundaries (yellow dotted line) show minimal variation compared to the equatorward boundaries (red dotted line) regardless of the solar wind conditions. The poleward boundaries also do not exhibit any strong correlations with any geomagnetic indices/solar wind parameters, including Dst* and Kp indices, which gave the highest predictability for the equatorward boundaries. Studies on the auroral boundaries such as *Carbary* (2005) and *Milan et al.* (2008) have found a strong correlation between the poleward boundaries and the Kp and Dst indices. However, these studies were conducted in hourly resolutions and therefore, respond to substorms which may be averaged out or damped under daily timescales. A future study could investigate the poleward boundary variations of MEE precipitation on a higher temporal resolution or around the onset of substorms to investigate if the poleward boundary is as dynamic as the equatorward boundary or if the poleward boundaries can be better modelled using one or more geomagnetic indices/solar wind parameters.

Figure 7.2 shows the variation of the yearly mean of the poleward boundary of >43 keV electron precipitation with solar activity in both hemispheres. Although the poleward boundaries move towards higher latitudes during the solar minimum with respect to active solar years, the difference between the minimum and the maximum is only about 2° CGMLat, further implying the poleward boundary is not as dynamic as the equatorward boundaries in daily timescales.

7.2.2 A New MEE Parameterization for Precipitating Fluxes

The natural step forward is to tie the key findings provided by the five papers together to develop a new MEE parametrization capable of estimating flux intensity, precipitation regions, and a realistic energy spectrum on both daily and decadal scales. As a first step, the varying equatorward boundary determined in Papers I and II should be implemented to revise the AE MEE proxy developed in Paper IV. Secondly, the flux distribution over the precipitation region should be explored, so that the flux intensity as a function of CGM latitudes is given a realistic representation. Thirdly, an average-based model, where the flux intensity is scaled by AE and the equatorward boundary is scaled by pressure-corrected RC and Dst, can be developed. The estimated fluxes and distribution should then be validated independent of the data made to establish the MEE parametrization. This can be done by estimating the MEE flux intensity and distribution for the period after 2015. Next, the discrepancies should be evaluated with

respect to solar wind drivers, solar wind and solar wind parameters. Then, the implementation of the probability assessment from Paper V should be explored and tested to see if they would give an overall better representation. Finally, the characteristics of the slot region events can be implemented to account for the additional MEE drizzle after the geomagnetic activity subsides.

These steps would allow us to create a novel and solid MEE parametrization that realistically represent the MEE forcing on the atmosphere over the entire period where relevant solar wind parameters and geomagnetic indices are available.

Bibliography

(1976), *U.S. Standard Atmosphere, 1976*, NOAA - SIT 76-1562, National Oceanic and Amospheric [sic] Administration. 4.1

Akasofu, S.-I. (2023), A new understanding of why the aurora has explosive characteristics, *Monthly Notices of the Royal Astronomical Society*, *518*(3), 3286–3300, doi:10.1093/mnras/stac3187. 3.1

Andersson, M. E., P. T. Verronen, S. Wang, C. J. Rodger, M. A. Clilverd, and B. R. Carson (2012), Precipitating radiation belt electrons and enhancements of mesospheric hydroxyl during 2004-2009, doi:10.1029/2011JD017246. 4.2.2

Andersson, M. E., P. T. Verronen, C. J. Rodger, M. A. Clilverd, and A. Seppälä (2014), Missing driver in the sun–earth connection from energetic electron precipitation impacts mesospheric ozone, *Nature Communications*, *5*(1), 5197, doi:10.1038/ncomms6197. 4.2.2

Asikainen, T., and K. Mursula (2011), Recalibration of the long-term noaa/meped energetic proton measurements, *Journal of atmospheric and solar-terrestrial physics*, *73*(2-3), 335–347. 5.3

Asikainen, T., and M. Ruopsa (2016), Solar wind drivers of energetic electron precipitation, *Journal of Geophysical Research: Space Physics*, *121*(3), 2209–2225, doi:10.1002/2015JA022215. 2.3, 3.5

Babu, E. M., H. N. Tyssøy, C. SmithJohnsen, V. Maliniemi, J. A. Salice, R. M. Millan, and I. G. Richardson (2022), Determining Latitudinal Extent of Energetic Electron Precipitation Using MEPED OnBoard NOAA/POES, *Journal of Geophysical Research: Space Physics*, *127*(9), doi:10.1029/2022ja030489. 4.2.2, 5.2, 5.4

Baumgaertner, A. J., A. Seppälä, P. Jöckel, and M. A. Clilverd (2011), Geomagnetic activity related NOx enhancements and polar surface air temperature variability in a chemistry climate model: Modulation of the NAM index, *Atmospheric Chemistry and Physics*, *11*(9), 4521–4531, doi:10.5194/acp-11-4521-2011. 4.2.2

Baumjohann, W., and R. A. Treumann (1996), *Basic Space Plasma Physics*, PUBLISHED BY IMPERIAL COLLEGE PRESS AND DISTRIBUTED BY WORLD SCIENTIFIC PUBLISHING CO., doi:10.1142/p015. 2.5, 4.3

Baumjohann, W., and R. A. Treumann (2012), *Basic space plasma physics (revised edition)*, 1–479 pp., Imperial College Press, doi:10.1142/P850. 2.2, 2.4, 2.3

Borovsky, J. E., and M. H. Denton (2006), Differences between CME-driven storms and CIR-driven storms, *Journal of Geophysical Research: Space Physics*, *111*, doi:https://doi.org/10.1029/2005JA011447. 3.5, 3.6

Brasseur, G., and S. Solomon (2005), *Aeronomy of the Middle Atmosphere: Chemistry and Physics of the Stratosphere and Mesosphere*, doi:10.1007/1-4020-3824-0. 4.1

Burton, R., R. McPherron, and C. Russell (1975), An empirical relationship between interplanetary conditions and Dst, *Journal of Geophysical Research: Space Physics*, *80*, doi:https://doi.org/10.1029/JA080i031p04204. 5.1

Cane, H. V., T. T. von Rosenvinge, C. M. S. Cohen, and R. A. Mewaldt (2003), Two components in major solar particle events, *Geophysical Research Letters*, *30*(12), doi:https://doi.org/10.1029/2002GL016580. 4.2.2

Carbary, J. F. (2005), A kp-based model of auroral boundaries, *Space Weather*, *3*(10), doi:https://doi.org/10.1029/2005SW000162. 7.2.1

Chapman, S., and V. C. A. Ferraro (1931), A new theory of magnetic storms, *Terrestrial Magnetism and Atmospheric Electricity*, *36*(3), 171–186, doi:https://doi.org/10.1029/TE036i003p00171. 2.4

Clilverd, M. A., C. J. Rodger, M. van de Kamp, and P. T. Verronen (2020), Electron precipitation from the outer radiation belt during the st. patrick's day storm 2015: Observations, modeling, and validation, *Journal of Geophysical Research: Space Physics*, *125*(2), e2019JA027,725, doi:https://doi.org/10.1029/2019JA027725, e2019JA027725 2019JA027725. 4.3

Curto, J. J., T. Araki, and L. F. Alberca (), Evolution of the concept of Sudden Storm Commencements and their operative identification, *Earth, Planets and Space*, doi:https://doi.org/10.1186/BF03352059. 5.1

Damiani, A., B. Funke, M. López-Puertas, M. L. Santee, R. R. Cordero, and S. Watanabe (2016), Energetic particle precipitation: A major driver of the ozone budget in the Antarctic upper stratosphere, *Geophysical Research Letters*, *43*(7), 3554–3562, doi:10.1002/2016GL068279. 4.2.2

Dang, T., B. Zhang, M. Wiltberger, W. Wang, R. Varney, X. Dou, W. Wan, and J. Lei (2018), On the relation between soft electron precipitations in the cusp region and solar wind coupling functions, *Journal of Geophysical Research: Space Physics*, *123*(1), 211–226, doi:https://doi.org/10.1002/2017JA024379. 3.1

Davis, T. N., and M. Sugiura (1966), Auroral electrojet activity index ae and its universal time variations, *Journal of Geophysical Research (1896-1977)*, *71*(3), 785–801, doi:https://doi.org/10.1029/JZ071i003p00785. 5.1

Denton, M. H., J. E. Borovsky, R. M. Skoug, M. F. Thomsen, B. Lavraud, M. G. Henderson, R. L. McPherron, J. C. Zhang, and M. W. Liemohn (2006), Geomagnetic storms driven by ICME- and CIR-dominated solar wind, *Journal of Geophysical Research (Space Physics)*, *111*(A7), A07S07, doi:10.1029/2005JA011436. 3.5

Dmitriev, A. V., N. B. Crosby, and J. K. Chao (2005), Interplanetary sources of space weather disturbances in 1997 to 2000, *Space Weather*, *3*(3), S03001, doi:10.1029/2004SW000104. 3.5

Dungey, J. W. (1961), Interplanetary magnetic field and the auroral zones, *Phys. Rev. Lett.*, *6*, 47–48, doi:10.1103/PhysRevLett.6.47. 2.1

Elliott, H. A., J.-M. Jahn, and D. J. McComas (2013), The Kp index and solar wind speed relationship: Insights for improving space weather forecasts, *Space Weather*, *11*(6), 339–349, doi:10.1002/swe.20053. 5.1

Evans, D., and M. Greer (2000), *Polar orbiting environmental satellite space environment monitor-2: Instrument description and archive data documentation.*, Boulder, Colo. : U.S. Dept. of Commerce, National Oceanic and Atmospheric Administration, Oceanic and Atmospheric Research Laboratories, Space Environment Center ; [Springfield, Va] : [For sale by the National Technical Information Service], [2000]. 5.3, 5.3, 5.3

Evans, D., and M. Greer (2004), *Polar Orbiting Environmental Satellite Space Environment Monitor - 2: Instrument Descriptions and Archive Data Documentation*, Boulder, Colo. : U.S. Dept. of Commerce, National Oceanic and Atmospheric Administration, Oceanic and Atmospheric Research Laboratories, Space Environment Center. 5.3

Fang, X., C. E. Randall, D. Lummerzheim, S. C. Solomon, M. J. Mills, D. R. Marsh, C. H. Jackman, W. Wang, and G. Lu (2008), Electron impact ionization: A new parameterization for 100 eV to 1 MeV electrons, *Journal of Geophysical Research: Space Physics*, *113*(9), doi:10.1029/2008JA013384. 4.2.2

Fraser, B. J., R. S. Grew, S. K. Morley, J. C. Green, H. J. Singer, T. M. Loto'aniu, and M. F. Thomsen (2010), Storm time observations of electromagnetic ion cyclotron waves at geosynchronous orbit: GOES results, *Journal of Geophysical Research: Space Physics*, *115*(A5), doi:https://doi.org/10.1029/2009JA014516. 3.4

Funke, B., M. López-Puertas, G. Stiller, and T. Von Clarmann (2014), Mesospheric and stratospheric NOy produced by energetic particle precipitation during 2002–2012, *Journal of Geophysical Research: Atmospheres*, *119*(7), 4429–4446. 4.2.2

Galand, M., and D. S. Evans (2000), Radiation damage of the proton MEPED detector on POES (TIROS/NOAA) satellites. 5.3

Garcia, R. R., D. R. Marsh, D. E. Kinnison, B. A. Boville, and F. Sassi (2007), Simulation of secular trends in the middle atmosphere, 19502003, *Journal of Geophysical Research: Atmospheres*, *112*(D9), doi:https://doi.org/10.1029/2006JD007485. 4.2.2

Gasque, L. C., R. M. Millan, and S. Shekhar (2021), Statistically Determining the Spatial Extent of Relativistic Electron Precipitation Events Using 2-s Polar-Orbiting Satellite Data, *Journal of Geophysical Research: Space Physics*, *126*, doi:https://doi.org/10.1029/2020JA028675. 4.3

Grebowsky, J. M. (1970), Model study of plasmapause motion, *Journal of Geophysical Research*, *75*(22), 4329–4333, doi:https://doi.org/10.1029/JA075i022p04329. 3.4

Horne, R. B., R. M. Thorne, S. A. Glauert, J. M. Albert, N. P. Meredith, and R. R. Anderson (2005), Timescale for radiation belt electron acceleration by whistler mode chorus waves, *Journal of Geophysical Research: Space Physics*, *110*(A3). 2.3

Jacchia, L. G. (1965), Density Variations in the Heterosphere, *SAO Special Report*, *184*. 4.1

Jackman, C., C. Randall, V. Harvey, S. Wang, E. Fleming, M. López-Puertas, B. Funke, and P. Bernath (2014), Middle atmospheric changes caused by the January and March 2012 solar proton events, *Atmospheric Chemistry and Physics*, *14*(2), 1025–1038. 4.2.2

Jordanova, V. K., R. M. Thorne, W. Li, and Y. Miyoshi (2010), Excitation of whistler mode chorus from global ring current simulations, *Journal of Geophysical Research: Space Physics*, *115*(A5), doi:https://doi.org/10.1029/2009JA014810. 3.4

Kataoka, R., and Y. Miyoshi (2006), Flux enhancement of radiation belt electrons during geomagnetic storms driven by coronal mass ejections and corotating interaction regions, *Space Weather*, *4*(9), doi:https://doi.org/10.1029/2005SW000211. 3.5, 3.5

Kavanagh, A. J., N. Cobbett, and P. Kirsch (2018), Radiation Belt Slot Region Filling Events: Sustained Energetic Precipitation Into the Mesosphere, *Journal of Geophysical Research: Space Physics*, *123*, doi:https://doi.org/10.1029/2018JA025890. 3.3, 5.4

Kennel, C. F., and H. E. Petschek (1966), Limit on Stably Trapped Particle Fluxes, *Tech. rep.* 5.3

Kilifarska, N. A. (2017), Hemispherical Asymmetry of the Lower Stratospheric O3 Response to Galactic Cosmic Rays Forcing, *ACS Earth and Space Chemistry*, *1*(2), 80–88, doi:10.1021/acsearthspacechem.6b00009. 6

Kilpua, E. K. J., A. Balogh, R. von Steiger, and Y. D. Liu (2017), Geoeffective properties of solar transients and stream interaction regions, *Space Science Reviews*, *212*(3), 1271–1314, doi:10.1007/s11214-017-0411-3. 3.5, 3.5

Kim, K.-C., Y. Shprits, D. Subbotin, and B. Ni (2011), Understanding the dynamic evolution of the relativistic electron slot region including radial and pitch angle diffusion, *Journal of Geophysical Research: Space Physics*, *116*(A10), doi:https://doi.org/10.1029/2011JA016684. 3.3

Kivelson, M., and C. Russell (1995), *Introduction to Space Physics*, Cambridge University Press, doi:10.1017/9781139878296. 2.6

Koskinen, J., and E. Kilpua (2022), *Physics of Earth's Radiation Belts*, Springer, doi:https://doi.org/10.1007/978-3-030-82167-8. 2.3

Kozyra, J. U., and M. W. Liemohn (2003), Ring Current Energy Input and Decay, *SSR*, *109*(1), 105–131, doi:10.1023/B:SPAC.0000007516.10433.ad. 3.5

Laundal, K. M., I. Cnossen, S. E. Milan, S. E. Haaland, J. Coxon, N. M. Pedatella, M. Förster, and J. P. Reistad (2017), North-South Asymmetries in Earth's Magnetic Field, *Space Science Reviews*, *206*(1-4), 225–257, doi:10.1007/s11214-016-0273-0. 6

Li, X., and M. A. Temerin (2001), The electron radiation belt, *Space Science Reviews*, *95*(1-2), 569–580. 3.3

Li, X., R. S. Selesnick, D. N. Baker, A. N. Jaynes, S. G. Kanekal, Q. Schiller, L. Blum, J. Fennell, and J. B. Blake (2015), Upper limit on the inner radiation belt MeV electron intensity, *Journal of Geophysical Research: Space Physics*, *120*(2), 1215–1228, doi:https://doi.org/10.1002/2014JA020777. 3.3

Liou, K., T. Sotirelis, and I. Richardson (2018), Substorm occurrence and intensity associated with three types of solar wind structure, *Journal of Geophysical Research: Space Physics*, *123*(1), 485–496, doi:https://doi.org/10.1002/2017JA024451. 2.1

Loewe, C. A., and G. W. Prölss (1997), Classification and mean behavior of magnetic storms, *Journal of Geophysical Research: Space Physics*, *102*(A7), 14,209–14,213, doi:https://doi.org/10.1029/96JA04020. 5.1

Lüehr, H., C. Xiong, N. Olsen, and G. Le (2016), Near-Earth Magnetic Field Effects of Large-Scale Magnetospheric Currents, *Space Science Reviews*, doi:10.1007/s11214-016-0267-y. 5.1

Lühr, H., and S. Maus (2010), Solar cycle dependence of magnetospheric currents and a model of their near-earth magnetic field, *Earth, Planets and Space*, *62*, 843848, doi:10.5047/eps.2010.07.012. 5.1

Lummerzheim, D. (1992), *Comparison of energy dissipation functions for high energy auroral electron and ion precipitation*, Geophysical Institute, University of Alaska Fairbanks Fairbanks. 4.2.2

Malin, S. R. C., and D. R. Barraclough (1991), Humboldt and the Earth's Magnetic Field, *Quarterly Journal of the Royal Astronomical Society*, *32*, 279. 3.5

Maliniemi, V., T. Asikainen, A. Salminen, and K. Mursula (2019), Assessing North Atlantic winter climate response to geomagnetic activity and solar irradiance variability, *Quarterly Journal of the Royal Meteorological Society*, *145*(725), 3780–3789, doi:10.1002/qj.3657. 4.2.2

Maliniemi, V., H. Nesse Tyssøy, C. Smith-Johnsen, P. Arsenovic, and D. R. Marsh (2021), Effects of enhanced downwelling of NOx on Antarctic upper-stratospheric ozone in the 21st century, *Atmospheric Chemistry and Physics*, *21*(14), 11,041–11,052, doi:10.5194/acp-21-11041-2021. 4.2.2

Matthes, K., B. Funke, M. E. Andersson, L. Barnard, J. Beer, P. Charbonneau, M. A. Clilverd, T. Dudok de Wit, M. Haberreiter, A. Hendry, C. H. Jackman, M. Kretzschmar, T. Kruschke, M. Kunze, U. Langematz, D. R. Marsh, A. C. Maycock, S. Misios, C. J. Rodger, A. A. Scaife, A. Seppälä, M. Shangguan, M. Sinnhuber, K. Tourpali, I. Usoskin, M. van de Kamp, P. T. Verronen, and S. Versick (2017), Solar forcing for CMIP6 (v3.2), *Geoscientific Model Development*, *10*(6), 2247–2302, doi:10.5194/gmd-10-2247-2017. 4.3

Meredith, N. P., R. B. Horne, M. M. Lam, M. H. Denton, J. E. Borovsky, and J. C. Green (2011), Energetic electron precipitation during high-speed solar wind stream driven storms, *Journal of Geophysical Research: Space Physics*, *116*(5), doi:10.1029/2010JA016293. 5.3

Milan, S. E., P. D. Boakes, and B. Hubert (2008), Response of the expanding/contracting polar cap to weak and strong solar wind driving: Implications for substorm onset, *Journal of Geophysical Research: Space Physics*, *113*(A9), doi:https://doi.org/10.1029/2008JA013340. 7.2.1

Millan, R., and R. Thorne (2007), Review of radiation belt relativistic electron losses, *Journal of Atmospheric and Solar-Terrestrial Physics*, *69*, doi:https://doi.org/10.1016/j.jastp.2006.06.019. 3.4, 3.4

Mironova, I. A., K. L. Aplin, F. Arnold, G. A. Bazilevskaya, R. G. Harrison, A. A. Krivolutsky, K. A. Nicoll, E. V. Rozanov, E. Turunen, and I. G. Usoskin (2015), Energetic particle influence on the earth's atmosphere, *Space Science Reviews*, *194*(1), 1–96, doi:10.1007/s11214-015-0185-4. 4.2.1, 4.2.2

Mironova, I. A., A. A. Artamonov, G. A. Bazilevskaya, E. V. Rozanov, G. A. Kovaltsov, V. S. Makhmutov, A. L. Mishev, and A. V. Karagodin (2019), Ionization of the Polar Atmosphere by Energetic Electron Precipitation Retrieved From Balloon Measurements, *Geophysical Research Letters*, *46*(2), 990–996, doi:https://doi.org/10.1029/2018GL079421. 4.3

Moldwin, M. B., L. Downward, H. Rassoul, R. Amin, and R. Anderson (2002), A new model of the location of the plasmapause: CRRES results, *Journal of Geophysical Research: Space Physics*, *107*, doi:https://doi.org/10.1029/2001JA009211. 3.4, 4.3, 5.1, 6, 6.1

Mursula, K., and B. Zieger (1996), The 13.5-day periodicity in the Sun, solar wind, and geomagnetic activity: The last three solar cycles, *Journal of Geophysical Research*, *101*(A12), 27,077–27,090, doi:10.1029/96JA02470. 3.5

Nesse Tyssøy, H., M. I. Sandanger, L. K. Ødegaard, J. Stadsnes, A. Aasnes, and A. E. Zawedde (2016), Energetic electron precipitation into the middle atmosphere-Constructing the loss cone fluxes from MEPED POES, *Journal of Geophysical Research: Space Physics*, *121*(6), 5693–5707, doi:10.1002/2016JA022752. 5.3, 5.3, 5.3, 6

Nesse Tyssøy, H., M. Sinnhuber, T. Asikainen, S. Bender, M. A. Clilverd, B. Funke, M. Kamp, J. M. Pettit, C. E. Randall, T. Reddmann, C. J. Rodger, E. Rozanov, C. SmithJohnsen, T. Sukhodolov, P. T. Verronen, J. M. Wissing, and O. Yakovchuk (2022), HEPPA III Intercomparison Experiment on Electron Precipitation Impacts: 1. Estimated Ionization Rates During a Geomagnetic Active Period in April 2010, *Journal of Geophysical Research: Space Physics*, *127*(1), doi:10.1029/2021JA029128. 4.2.2, 4.2.2, 4.4, 4.5, 4.3, 5.3

Nesse Tyssøy, H., and J. Stadsnes (2015), Cutoff latitude variation during solar proton events: Causes and consequences, *Journal of Geophysical Research: Space Physics*, *120*(1), 553–563, doi:https://doi.org/10.1002/2014JA020508. 4.2.2

Newell, P. T., K. Liou, and G. R. Wilson (2009), Polar cap particle precipitation and aurora: Review and commentary, *Journal of Atmospheric and Solar-Terrestrial Physics*, *71*(2), 199–215, doi:https://doi.org/10.1016/j.jastp.2008.11.004. 3.1

O'Brien, T., and M. Moldwin (2003), Empirical plasmapause models from magnetic indices, *Geophysical Research Letters*, *30*(4). 3.4, 4.3, 5.1

Ødegaard, L.-K. G., T. H. Nesse, J. Sandanger, Marit Ireneand Stadsnes, and F. Søraas (2016), Space Weather impact on the degradation of NOAA POES MEPED proton detectors, *Journal of Space Weather and Space Climate*, *6*, doi:https://doi.org/10.1051/swsc/2016020. 5.3

Ødegaard, L.-K. G., T. H. Nesse, F. Søraas, J. Stadsnes, and M. I. Sandanger (2017), Energetic electron precipitation in weak to moderate corotating interaction region-driven storms, *Journal of Geophysical Research: Space Physics*, *122*, doi:https://doi.org/10.1002/2016JA023096. 5.3

Olsen, N., T. J. Sabaka, and F. Lowes (2005), New parameterization of external and induced fields in geomagnetic field modeling, and a candidate model for IGRF 2005, *Earth, Planets and Space*, *57*, 1141–1149. 5.1

Olsen, N., H. Lühr, C. C. Finlay, T. J. Sabaka, I. Michaelis, J. Rauberg, and L. Tøffner-Clausen (2014), The CHAOS-4 Geomagnetic Field Model, *Geophysical Journal International*, *197*, 815 – 827, doi:https://doi.org/10.1093/gji/ggu033. 5.1

Parker, E. N. (1963), *Interplanetary Dynamical Processes*, 1–272 pp., UMI. 2.1

Pettit, J. M., C. E. Randall, E. D. Peck, D. R. Marsh, M. van de Kamp, X. Fang, V. L. Harvey, C. J. Rodger, and B. Funke (2019), Atmospheric effects of >30-kev energetic electron precipitation in the southern hemisphere winter during 2003, *Journal of Geophysical Research: Space Physics*, *124*(10), 8138–8153, doi:https://doi.org/10.1029/2019JA026868. 4.2.2, 4.3

Pierrard, V., E. Botek, J. F. Ripoll, S. A. Thaller, M. B. Moldwin, M. Ruohoniemi, and G. Reeves (2021), Links of the Plasmapause With Other Boundary Layers of the Magnetosphere: Ionospheric Convection, Radiation Belt Boundaries, Auroral Oval, *Frontiers in Astronomy and Space Sciences*, *8*, doi:10.3389/fspas.2021.728531. 3.4

Randall, C., D. Rusch, R. Bevilacqua, K. Hoppel, and J. Lumpe (1998), Polar ozone and aerosol measurement (POAM) II stratospheric NO2, 1993–1996, *Journal of Geophysical Research: Atmospheres*, *103*(D21), 28,361–28,371. 4.2.2

Randall, C., V. Harvey, G. Manney, Y. Orsolini, M. Codrescu, C. Sioris, S. Brohede, C. Haley, L. Gordley, J. Zawodny, et al. (2005), Stratospheric effects of energetic particle precipitation in 2003–2004, *Geophysical Research Letters*, *32*(5). 4.2.2

Richardson, I. G. (2018), Solar wind stream interaction regions throughout the heliosphere, doi:10.1007/s41116-017-0011-z. 2.1

Richardson, I. G., E. W. Cliver, and H. V. Cane (2001), Sources of geomagnetic storms for solar minimum and maximum conditions during 1972-2000, *Geophysical Research Letters*, *28*(13), 2569–2572, doi:10.1029/2001GL013052. 3.5

Ripoll, J. F., S. G. Claudepierre, A. Y. Ukhorskiy, C. Colpitts, X. Li, J. F. Fennell, and C. Crabtree (2020), Particle Dynamics in the Earth's Radiation Belts: Review of Current Research and Open Questions, *Journal of Geophysical Research: Space Physics*, *125*(5), doi:10.1029/2019JA026735. 3.4

Roble, R. G., and E. C. Ridley (1987), An auroral model for the NCAR thermospheric general circulation model (TGCM), *Annales Geophysicae*, *5*, 369–382. 4.2.2

Rodger, C. J., M. A. Clilverd, J. C. Green, and M. M. Lam (2010), Use of POES SEM-2 observations to examine radiation belt dynamics and energetic electron precipitation into the atmosphere, *Journal of Geophysical Research: Space Physics*, *115*(4), doi:10.1029/2008JA014023. 4.2.2, 5.3, 5.3

Rodger, C. J., A. J. Kavanagh, M. A. Clilverd, and S. R. Marple (2013), Comparison between POES energetic electron precipitation observations and riometer absorptions: Implications for determining true precipitation fluxes, *Journal of Geophysical Research: Space Physics*, *118*(12), 7810–7821, doi:10.1002/2013JA019439. 3.1, 3.2, 5.3

Rozanov, E., M. Calisto, T. Egorova, T. Peter, and W. Schmutz (2012), Influence of the precipitating energetic particles on atmospheric chemistry and climate, *Surveys in geophysics*, *33*(3), 483–501. 4.2.2

Sahai, Y., F. Becker-Guedes, P. Fagundes, R. Jesus, A. De Abreu, L. Paxton, L. Goncharenko, C. Brunini, M. Gende, A. Ferreira, N. Lima, F. Guarnieri, V. Pillat, J. Bittencourt, and

C. Candido (2009), Effects observed in the latin american sector ionospheric f region during the intense geomagnetic disturbances in the early part of november 2004, *Journal of Geophysical Research*, *114*, doi:10.1029/2007JA013007. 5.1

Salice, J. A., H. Nesse, E. M. Babu, C. Smith-Johnsen, and I. G. Richardson (2023), Exploring the Predictability of the High-Energy Tail of MEE Precipitation Based on Solar Wind Properties, *Journal of Geophysical Research: Space Physics*, *128*(3), e2022JA031,194, doi:https://doi.org/10.1029/2022JA031194, e2022JA031194 2022JA031194. 3.5, 4.2.2

Sandanger, M., L. Ødegaard, T. HN, J. Stadsnes, F. Søraas, K. Oksavik, and K. Aarsnes (2015), Inflight calibration of NOAA POES proton detectorsDerivation of the MEPED correction factors, *Journal of Geophysical Research: Space Physics*, *120*, 9578–9593, doi:https://doi.org/10.1002/2015JA021388. 5.3, 5.3

Schwenn, R. (2006), Solar Wind Sources and Their Variations Over the Solar Cycle, , *124*(1-4), 51–76, doi:10.1007/s11214-006-9099-5. 2.1

Seppälä, A., C. Randall, M. Clilverd, E. Rozanov, and C. Rodger (2009), Geomagnetic activity and polar surface air temperature variability, *Journal of Geophysical Research: Space Physics*, *114*, doi:https://doi.org/10.1029/2008JA014029. 4.2.2

Seppälä, A., K. Matthes, C. E. Randall, and I. A. Mironova (2014), What is the solar influence on climate? Overview of activities during CAWSES-II, *Progress in Earth and Planetary Science*, *1*(1), 24, doi:10.1186/s40645-014-0024-3. 1.1, 4.2.1, 4.3, 4.2.2

Shekhar, S., R. Millan, and D. Smith (2017), A Statistical Study of the Spatial Extent of Relativistic Electron Precipitation With Polar Orbiting Environmental Satellites, *Journal of Geophysical Research: Space Physics*, *122*(11), 274–11, doi:10.1002/2017JA024716. 4.3

Shen, X.-C., M. K. Hudson, A. N. Jaynes, Q. Shi, A. Tian, S. G. Claudepierre, M.-R. Qin, Q.-G. Zong, and W.-J. Sun (2017), Statistical study of the storm time radiation belt evolution during Van Allen Probes era: CME- versus CIR-driven storms, *Journal of Geophysical Research: Space Physics*, *122*(8), 8327–8339, doi:https://doi.org/10.1002/2017JA024100. 3.5

Sinnhuber, M., H. Nieder, and N. Wieters (2012), Energetic Particle Precipitation and the Chemistry of the Mesosphere/Lower Thermosphere, *Surveys in Geophysics*, *33*, doi:https://doi.org/10.1007/s10712-012-9201-3. 4.2.2

Sinnhuber, M., H. Nesse Tyssøy, T. Asikainen, S. Bender, B. Funke, K. Hendrickx, J. Pettit, T. Reddmann, E. Rozanov, H. Schmidt, et al. (2022), Heppa III Intercomparison Experiment on Electron Precipitation Impacts: 2. Model-Measurement Intercomparison of Nitric Oxide (NO) During a Geomagnetic Storm in April 2010, *Journal of Geophysical Research: Space Physics*, *127*(1), e2021JA029,466. 4.3

Siscoe, G., N. Crooker, and C. Clauer (2006), Dst of the carrington storm of 1859, *Advances in Space Research*, *38*(2), 173–179, doi:https://doi.org/10.1016/j.asr.2005.02.102. 5.1

Smith-Johnsen, C., H. Nesse Tyssøy, K. Hendrickx, Y. Orsolini, G. Kishore Kumar, L.-K. G. Ødegaard, M. I. Sandanger, F. Stordal, and L. Megner (2017), Direct and indirect electron precipitation effect on nitric oxide in the polar middle atmosphere, using a full-range energy spectrum, *Journal of Geophysical Research: Space Physics*, *122*(8), 8679–8693, doi:https://doi.org/10.1002/2017JA024364. 4.2.2

Smith-Johnsen, C., D. R. Marsh, Y. Orsolini, H. Nesse Tyssøy, K. Hendrickx, M. I. Sandanger, L.-K. G. Ødegaard, and F. Stordal (2018), Nitric Oxide Response to the April 2010 Electron Precipitation Event: Using WACCM and WACCM-D With and Without Medium-Energy Electrons, *Journal of Geophysical Research: Space Physics*, *123*(6), 5232–5245, doi:https://doi.org/10.1029/2018JA025418. 4.2.2

Solomon, S., P. J. Crutzen, and R. G. Roble (1982), Photochemical coupling between the thermosphere and the lower atmosphere: 1. Odd nitrogen from 50 to 120 km., *Journal of Geophysical Research*, *87*(C9), 7206–7220, doi:10.1029/JC087iC09p07206. 4.2.2

Sugiura, M. (1964), Hourly values of equatorial Dst for IGY, *Ann. Int. Geophys. Year*, *35*, 49. 3.5

Swift, D. W. (1981), Mechanisms for auroral precipitation: A review, *Rev. Geophys. Space Phys.; (United States)*, *19*, doi:10.1029/RG019i001p00185. 3.1

Szelag, M. E., D. R. Marsh, P. T. Verronen, A. Seppälä, and N. Kalakoski (2022), Ozone impact from solar energetic particles cools the polar stratosphere, *Nature Communications*, *13*(1), 6883, doi:10.1038/s41467-022-34666-y. 4.2.2

Temerin, M., and X. Li (2015), The Dst index underestimates the solar cycle variation of geomagnetic activity, *Journal of Geophysical Research: Space Physics*, *120*, doi:https://doi.org/10.1002/2015JA021467. 5.1, 6

Theodoridis, G. C., and F. R. Paolini (1967), Pitch angle diffusion of relativistic outer belt electrons, *Ann. Geophys.*, *23*, 375–381. 5.3

Thomsen, M. F. (2004), Why Kp is such a good measure of magnetospheric convection, *Space Weather*, *2*(11), S11004, doi:10.1029/2004SW000089. 5.1

Thomsen, M. F., J. E. Borovsky, D. J. McComas, and M. R. Collier (1998), Variability of the ring current source population, *Geophysical Research Letters*, *25*(18), 3481–3484, doi:10.1029/98GL02633. 3.5

Thorne, R. M. (1980), The Importance of Energetic Particle Precipitation on the Chemical Composition of the Middle Atmosphere, *Pure and Applied Geophysics*, *118*, doi:https://doi.org/10.1007/BF01586448. 1.1

Thorne, R. M. (2010), Radiation belt dynamics: The importance of wave-particle interactions, *Geophysical Research Letters*, *37*(22), doi:10.1029/2010GL044990. 3.4, 3.3

Thorne, R. M., B. Ni, X. Tao, R. B. Horne, and N. P. Meredith (2010), Scattering by chorus waves as the dominant cause of diffuse auroral precipitation, *Nature*, *467*(7318), 943–946, doi:10.1038/nature09467. 3.1

Tsurutani, B. T., W. D. Gonzalez, G. Lakhina, and S. Alex (2003), The extreme magnetic storm of 1–2 september 1859, *Journal of Geophysical Research: Space Physics*, *108*(A7), doi:https://doi.org/10.1029/2002JA009504. 5.1

Turunen, E., P. T. Verronen, A. Seppälä, C. J. Rodger, M. A. Clilverd, J. Tamminen, C. F. Enell, and T. Ulich (2009), Impact of different energies of precipitating particles on NOx generation in the middle and upper atmosphere during geomagnetic storms, *Journal of Atmospheric and Solar-Terrestrial Physics*, *71*(10-11), 1176–1189, doi:10.1016/j.jastp.2008.07.005. 4.2, 4.2.2

Tyssøy, H. N., A. Haderlein, M. Sandanger, and J. Stadsnes (2019), Intercomparison of the POES/MEPED Loss Cone Electron Fluxes With the CMIP6 Parametrization, *Journal of Geophysical Research: Space Physics*, *124*, doi:https://doi.org/10.1029/2018JA025745. 4.2.2, 4.2.2, 4.3

Tyssøy, H. N., N. Partamies, E. M. Babu, C. Smith-Johnsen, and J. A. Salice (2021), The predictive capabilities of the auroral electrojet index for medium energy electron precipitation, *Frontiers in Astronomy and Space Sciences*, *8*, doi:10.3389/fspas.2021.714146. 5.2

Van Allen, J. A. (1959), The geomagnetically trapped corpuscular radiation, *Journal of Geophysical Research: Space Physics*, *64*, doi:https://doi.org/10.1029/JZ064i011p01683. 3.3

van de Kamp, M., A. Seppälä, M. A. Clilverd, C. J. Rodger, P. T. Verronen, and I. C. Whittaker (2016), A model providing long-term data sets of energetic electron precipitation during geomagnetic storms, *Journal of Geophysical Research*, *121*(20), 520–12, doi:10.1002/2015JD024212. (document), 3.4, 4, 4.3, 4.3

van de Kamp, M., C. J. Rodger, A. Seppälä, M. A. Clilverd, and P. T. Verronen (2018), An Updated Model Providing Long-Term Data Sets of Energetic Electron Precipitation, Including Zonal Dependence, *Journal of Geophysical Research: Atmospheres*, *123*(17), 9891–9915, doi:10.1029/2017JD028253. 3.4, 4.3

Verronen, P. T., C. J. Rodger, M. A. Clilverd, and S. Wang (2011), First evidence of mesospheric hydroxyl response to electron precipitation from the radiation belts, *Journal of Geophysical Research Atmospheres*, *116*(7), doi:10.1029/2010JD014965. 4.2.2

Ward, W., A. Seppälä, E. Yiğit, T. Nakamura, C. Stolle, J. Laštovička, T. N. Woods, Y. Tomikawa, F.-J. Lübken, S. C. Solomon, D. R. Marsh, B. Funke, and D. Pallamraju (2021), Role Of the Sun and the Middle atmosphere/thermosphere/ionosphere In Climate (ROSMIC): a retrospective and prospective view, *Progress in Earth and Planetary Science*, *8*(1), 47, doi:10.1186/s40645-021-00433-8. 4.2.1, 4.2.2

Xiao, F., Q. Zong, Z. Su, C. Yang, Z. He, Y. Wang, and Z. Gao (2013), Determining the mechanism of cusp proton aurora, *Scientific Reports*, *3*(1), 1654, doi:10.1038/srep01654. 3.1

Yando, K., R. M. Millan, J. C. Green, and D. S. Evans (2011), A monte carlo simulation of the NOAA POES Medium Energy Proton and Electron Detector instrument, *Journal of Geophysical Research: Space Physics*, *116*, doi:https://doi.org/10.1029/2011JA016671. 5.3, 5.3

Yermolaev, Y. I., and M. Y. Yermolaev (2002), Statistical Relationships between Solar, Interplanetary, and Geomagnetospheric Disturbances, 1976-2000, *Cosmic Research*, *40*(1), 1–14. 3.5

Yuan, C. J., and Q.-G. Zong (2012), Quantitative aspects of variations of 1.56.0 MeV electrons in the outer radiation belt during magnetic storms, *Journal of Geophysical Research: Space Physics*, *117*(A11), doi:https://doi.org/10.1029/2011JA017346. 3.5

Zawedde, A. E., H. Nesse Tyssøy, R. Hibbins, P. J. Espy, L.-K. G. Ødegaard, M. I. Sandanger, and J. Stadsnes (2016), The impact of energetic electron precipitation on mesospheric hydroxyl during a year of solar minimum, *Journal of Geophysical Research: Space Physics*, *121*(6), 5914–5929, doi:https://doi.org/10.1002/2016JA022371. 4.2.2

Zawedde, A. E., H. Nesse Tyssøy, J. Stadsnes, and M. I. Sandanger (2019), Are EEP Events Important for the Tertiary Ozone Maximum?, *Journal of Geophysical Research: Space Physics*, *124*(7), 5976–5994, doi:https://doi.org/10.1029/2018JA026201. 4.2.2, 4.2.2

Zhang, Y., W. Sun, X. S. Feng, C. S. Deehr, C. D. Fry, and M. Dryer (2008), Statistical analysis of corotating interaction regions and their geoeffectiveness during solar cycle 23, *Journal of Geophysical Research: Space Physics*, *113*(A8), doi:https://doi.org/10.1029/2008JA013095. 3.5

Zúñiga López, H. D., H. N. Tyssøy, C. Smith-Johnsen, and V. Maliniemi (2022), The Direct Effect of Medium Energy Electron Precipitation on Mesospheric Dynamics During a Sudden Stratospheric Warming Event in 2010, *Geophysical Research Letters*, *49*(13), doi:10.1029/2022GL097812. 4.2.2, 4.2.2

Chapter 8

Scientific Results

Paper I

Determining Latitudinal Extent of Energetic Electron Precipitation Using MEPED On-Board NOAA/POES

E.M. Babu, H. Nesse Tyssøy, C. Smith-Johnsen, V. Maliniemi, J.A. Salice, R.M. Millan, and I.G. Richardson.
Journal of Geophysical Research: Space Physics, **127**, doi:10.1029/2022JA030489 (2022)

JGR Space Physics

RESEARCH ARTICLE
10.1029/2022JA030489

Determining Latitudinal Extent of Energetic Electron Precipitation Using MEPED On-Board NOAA/POES

E. M. Babu[1], H. Nesse Tyssøy[1], C. Smith-Johnsen[1], V. Maliniemi[1], J. A. Salice[1], R. M. Millan[2], and I. G. Richardson[3,4]

[1]Department of Physics and Technology, Birkeland Centre for Space Science, University of Bergen, Bergen, Norway, [2]Department of Physics and Astronomy, Dartmouth College, Hanover, NH, USA, [3]Heliophysics Science Division, NASA Goddard Space Flight Center, Greenbelt, MD, USA, [4]Department of Astronomy, University of Maryland, College Park, MD, USA

Key Points:

- A model predicting equatorward extent of >43 keV electron precipitation is developed based on pressure-corrected Dst
- The model has an error estimate of ±2.2° cgmlat over a full solar cycle (2004–2014)
- The model has the highest accuracy during periods dominated by high-speed solar wind streams

Correspondence to:
E. M. Babu,
Eldho.Babu@uib.no

Citation:
Babu, E. M., Tyssøy, H. N., Smith-Johnsen, C., Maliniemi, V., Salice, J. A., Millan, R. M., & Richardson, I. G. (2022). Determining latitudinal extent of energetic electron precipitation using MEPED on-board NOAA/POES. *Journal of Geophysical Research: Space Physics, 127*, e2022JA030489. https://doi.org/10.1029/2022JA030489

Received 24 MAR 2022
Accepted 14 SEP 2022

Abstract Energetic Electron Precipitation (EEP) from the plasma sheet and the radiation belts ionizes the polar lower thermosphere and mesosphere. EEP increases the production of NO_x and HO_x, which will catalytically destroy ozone, an important element of atmospheric dynamics. Therefore, measurement of the latitudinal extent of the precipitation boundaries is important in quantifying the atmospheric effects of the Sun-Earth interaction. This study uses measurements by the Medium Energy Proton Electron Detector (MEPED) of six NOAA/POES and EUMETSAT/METOP satellites from 2004 to 2014 to determine the latitudinal boundaries of EEP and their variability with geomagnetic activity and solar wind drivers. Variation of the boundaries for different electron energies and Magnetic Local Time (MLT) is studied. Regression analyses are applied to determine the best predictor variable based on solar wind parameters and geomagnetic indices. The highest correlation was found for the pressure-corrected Dst index when applying a linear regression model. A model of the equatorward EEP boundary is developed separately for three different energy channels, >43, >114, and >292 keV, and for 3 hour MLT sectors. For >43 keV EEP, 80% of the equatorward boundaries predicted by the model are within ±2.2° cgmlat. The model exhibits a solar cycle bias where it systematically exaggerates the equatorward movement of the EEP region during solar minimum. The highest accuracy of the model is found in periods dominated by corotating interaction regions/high speed solar wind streams. The result will be a key element for constructing a model of EEP variability to be applied in atmosphere climate models.

Plain Language Summary Charged particles trapped in the Earth's magnetic field get accelerated to high energies through various magnetospheric processes. They can eventually precipitate into the Earth's atmosphere in a process known as Energetic Electron Precipitation or EEP. EEP deposits energy in the mesosphere and lower thermosphere which increase the production of ozone-depleting substances. Vertical transport of these, in particular during winter, can lead to indirect destruction of stratospheric ozone, a crucial element of atmospheric dynamics. Therefore, measurement of the latitudinal extent of EEP is important in quantifying the atmospheric effects of the Sun-Earth interaction. We use measurements from six NOAA/POES and EUMETSAT/METOP satellites from 2004 to 2014 to determine the equatorward latitudinal boundaries of EEP. We investigate how they correlate with solar wind parameters and geomagnetic indices to identify the best predictor for EEP boundaries. The result will be a key element for constructing a model of EEP variability to be applied in atmosphere climate models.

1. Introduction

Near-Earth space is permeated by solar plasma, driven by the slow solar winds, Coronal Mass Ejections (CMEs) or High-speed Solar wind Streams (HSSs) (Borovsky & Denton, 2006). CMEs are enormous plasma eruptions commonly caused by stressed magnetic fields around sunspots resulting in the most powerful geomagnetic storms. HSSs originate from coronal holes on the Sun. As the HSSs catch up with the slow solar wind, compression regions form, known as Co-rotating Interaction Regions (CIRs) (Richardson, 2018). Although the HSS/CIR geomagnetic disturbances typically are not as strong as CMEs, they often produce longer disturbed conditions in the near-Earth space (Zhang et al., 2007). The energetic electrons and ions from the solar wind and from the Earth's ionosphere gets trapped in the Earth's magnetosphere and forms torus-shaped regions (Shelley et al., 1972; Van Allen, 1959) constituting the radiation belts or the Van Allen belts. Investigating these trapped

particles have been a matter of interest since its discovery in 1958. Charged particles will be accelerated in the inner magnetosphere to significantly higher energy levels than in the solar wind by wave-particle accelerations and inward radial diffusion (Friedel et al., 2002).

There are two sinks that prompt loss of plasma from the radiation belts. The first is loss through the magnetopause back into the solar wind. The second sink is the atmosphere. Magnetospheric perturbations from plasma instabilities, pitch-angle anisotropy, and gradients in temperature and density generate plasma waves causing pitch-angle scattering of trapped particles into the atmospheric loss cone (Millan & Thorne, 2007), where they collide with atmospheric gases and deposit their energy.

Precipitating medium-energy electrons (MEE) (≥30 keV) amplify the local production of odd nitrogen (NO_x: N, NO, NO_2) and odd hydrogen (HO_x: H, OH, HO_2). NO_x can live sufficiently long in polar winter to be transported down to stratospheric altitudes affecting stratospheric ozone (Damiani et al., 2016; Maliniemi et al., 2021; Solomon et al., 1982), while HO_x have the capability of disrupting the mesospheric ozone balance (Andersson et al., 2012; Verronen et al., 2011; Zawedde et al., 2019). These chemical processes can impact the atmospheric temperature and dynamics, the consequences of which, might map down to the troposphere and surface (Baumgaertner et al., 2011; Maliniemi et al., 2019; Seppälä et al., 2009). Therefore, quantification of energetic electron precipitation (EEP), particularly its MEE aspect, is important in terms of understanding the impact of the Sun on the Earth's climate.

An accurate quantification of the MEE precipitation will require a solid description of both the overall MEE intensity, as well as its latitudinal extent. The plasmapause location is considered to play a critical role in determining the equatorward boundary of the MEE precipitation region (Moldwin et al., 2002; Pierrard et al., 2021, and references therein). It marks the outer boundary of the dense cold plasma in the plasmasphere. As the properties of electromagnetic waves strongly depend on the medium they propagate in, the plasmapause marks an abrupt change in the characteristics of the wave-particle interaction, and hence the radiation belt MEE diffusion rate into the atmospheric loss cone (Moldwin et al., 2002; Pierrard et al., 2021; Whittaker et al., 2014, and references therein). Chorus waves are dominating the EEP processes outside of the plasmasphere (Whittaker et al., 2014). Electromagnetic Ion Cyclotron (EMIC) wave-driven precipitation processes are favorable close to the outer edge of the plasmasphere (Carson et al., 2013), while plasmaspheric hiss are expected to be responsible for weak MEE precipitating fluxes within the plasmasphere (Hardman et al., 2015), as are lightning-generated whistlers (Rodger et al., 2007; Voss et al., 1998). The plasmapause location can vary strongly with geomagnetic activity, which implies a corresponding change in the equatorward boundary of the MEE precipitation.

Recently, van de Kamp et al. (2016) and van de Kamp et al. (2018) developed a MEE atmospheric ionization-rate model (>30 keV) based on an empirically derived plasmapause location, geomagnetic activity, and observations based on the Medium Energy Proton Electron Detector (MEPED) 0° telescopes on-board the National Oceanic and Atmospheric Administration (NOAA), Polar Orbiting Environmental Satellites (POES), and ESA's Meteorological Operational (MetOp) Satellites. The same observations have been used by Shekhar et al. (2017) and Gasque et al. (2021) to statistically determine the spatial extent of precipitating relativistic electrons (>800 keV). At high to mid-latitudes the MEPED 0° telescopes detect precipitating particle fluxes, whereas the 90° telescopes detect precipitating particle fluxes and/or trapped particles in the radiation belts (Nesse Tyssøy et al., 2016; Rodger et al., 2010). In the common case of pitch angle anisotropy, the 0° telescopes will underestimate, while the 90° telescopes will overestimate the flux of precipitating electrons (Nesse Tyssøy et al., 2016; Tyssøy et al., 2019). Hence, an accurate determination of the precipitation region will require the ability to estimate the MEE precipitating fluxes also during weak pitch angle diffusion. In this study, we combine observations from both the MEPED 0° and 90° detectors together with the theory of pitch angle diffusion by wave-particle interaction to quantify the MEE flux in the Bounce Loss Cone (BLC). At a specific latitude the size of the BLC changes with longitude due to the variation in the magnetic field strength. Over one drift period, the largest BLC will correspond to the drift loss cone. Applying the BLC compared to drift loss cone enables assessment of longitudinal differences and prevents overestimation of the precipitation at regions where the BLC is small. Also, as the level of anisotropy will vary with energy, we treat the MEPED energy channels, >43, >114, and >292 keV independently. We determine the equatorward boundary of the MEE precipitation region on a daily scale over a full solar cycle from 2004 to 2014 for different MLTs. We explore its dependency on solar wind components and geomagnetic activity. The parameter giving the highest predictability is used to develop a model which will be a key element for constructing a model of MEE variability to be applied in chemistry-climate models. The paper

is organized as follows: Section 2 describes the electron count measurements and the method to estimate the precipitating fluxes. Section 3 outlines the process of identifying the equatorward boundaries, whereas Section 4 examines its correlation with solar wind parameters and geomagnetic indices. The subsequent model and its accuracy is presented in Section 5.

2. Data

The Space Environment Monitor (SEM) on-board the NOAA/POES and EUMETSAT/MetOp series have been measuring precipitating and trapped electron and proton fluxes since 1978, covering roughly four solar cycles. These satellites have a circular sun-synchronous polar orbit with an orbital period of approximately 102 min (Evans & Greer, 2000). Each satellite covers similar MLT regions in every pass while moving through the L-shells. Their orbital altitude of 800–850 km from the surface of the Earth with a stabilized spatial orientation (Evans & Greer, 2000), allows them to monitor both trapped and precipitating particles near the foot of the field lines (Rodger et al., 2010; Nesse Tyssøy et al., 2016).

For this study, we use the MEPED on-board the second-generation SEM-2 instrument package which commenced its operation in 1998. The MEPED instrument has two solid-state detectors (0° and 90°) to measure a wide energy range of protons and electrons (Evans & Greer, 2000). This study concerns energetic electrons and therefore, uses readings from the electron telescopes. The MEPED electron telescopes have three energy channels E1, E2, and E3 measuring integral electron fluxes with nominal energy values of >30, >100, and >300 keV, respectively. Yando et al. (2011), however, demonstrated that the real detector efficiency will strongly depend on the incoming energy spectrum. Ødegaard et al. (2017) utilized the geometric factors given in Yando et al. (2011) to determine new optimized effective integral energy limits >43, >114, and >292 keV and associated geometric factors based on a series of realistic power law and exponential spectra. Furthermore, the electron energy channels suffer from >210 keV proton contamination (Evans & Greer, 2000; Yando et al., 2011) which results in false counts if used without rectification. We first apply the proton correction factors obtained by Sandanger et al. (2015) and Ødegaard et al. (2016) before fitting a monotonic piecewise cubic Hermite interpolating polynomial to the observed proton fluxes. The proton flux in the energy ranges known to impact the respective electron channels (Evans & Greer, 2000) is then retrieved and subtracted from the originally measured electron fluxes.

The 0° detector points toward the local zenith and measures particles near the center of the atmospheric BLC at high latitudes while the 90° detector, mounted orthogonally to the 0° detector and antiparallel to the spacecraft velocity vector, quantifies a combination of particles inside and outside the atmospheric BLC (Evans & Greer, 2000; Meredith et al., 2011; Nesse Tyssøy et al., 2016; Rodger et al., 2010). Consequently, using either the 0° or the 90° detector alone for this study will be an under-estimate or an over-estimate, respectively. We account for this by combining fluxes from both the 0° and 90° telescopes together with electron pitch angle distributions from the theory of wave-particle interactions in the magnetosphere. We solve the Fokker-Planck equation for particle diffusion (Kennel & Petschek, 1966; Theodoridis & Paolini, 1967) for a wide range of diffusion coefficients (the specific equations are also given in Nesse Tyssøy et al., 2016). The solutions are then transformed to the satellite altitude and stored in a lookup table. When comparing the theoretical pitch angle distributions with the measured particle fluxes, the procedure is as follows: We calculate the ratio between the fluxes detected by the 0° and 90° detector. We apply the telescope's viewing directions relative to the magnetic field and calculate the corresponding ratio for the theoretical solution. Next, we determine which of the theoretical pitch angle distributions best corresponds to the observed ratio. Finally, the size of the BLC, predicted based on the International Geomagnetic Reference Field (IGRF) model, are applied to estimate the precipitating fluxes. The BLC flux estimate is done separately for each energy channel as the level of particle diffusion will vary with energy. A detailed explanation of the method can be found in Nesse Tyssøy et al. (2016).

We used six different satellites during the investigation period; NOAA15, NOAA16, NOAA17, NOAA18, NOAA19, and MetOp-2, as seen in the right panel of Figure 1. The satellites have good coverage in most of the MLT sectors. We bin daily resolved fluxes into eight MLT sectors with 3 hr resolution and 1° magnetic latitude. However, in the Northern Hemisphere (NH), there is insufficient data in sectors 18–21 in the first half of the 11 years and sectors 21–24 in the second half (as seen in the left panel of Figure 1). Hence, we chose to ignore the MLT sectors 18–24.

For each day of the 11-year data series, the near-Earth solar wind condition is classified into three categories: CME, HSS/CIR, and slow ambient solar wind, based on the list created by Ian Richardson of the University

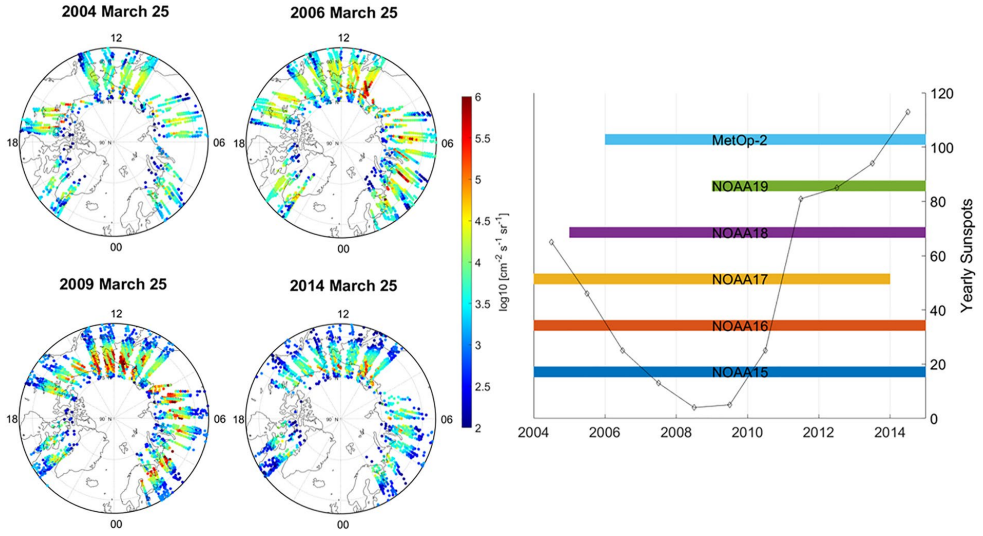

Figure 1. (left) Daily electron flux observation (>43 keV) and satellite ground-track during 25 March 2004, 2006, 2009, and 2014. (right) Polar Orbiting Environmental Satellites and Meteorological Operational satellite coverage during the 11 years of this study.

of Maryland and NASA Goddard Space Flight Center. The classification is done through examination of solar wind plasma parameters and geomagnetic indices obtained from the NASA Omniweb database along with 0.1–100 MeV energetic particle observations and cosmic ray observations from Goddard Space Flight Center instruments (Richardson & Cane, 2012). CIR and ambient will be used in this paper for convenience to denote the HSS/CIR and slow solar wind, respectively.

3. Identifying the Latitude Boundary

In this study, we focus on the NH applying the estimated BLC fluxes over the geomagnetic latitude band from 45° to 75°. We identify the latitude boundaries by first defining a threshold level in the region 50°–60° geomagnetic latitude. We define a threshold value for each channel across all MLT sectors based on mean flux values plus two standard deviation during ambient solar wind conditions.

The equatorward boundary is identified as the geomagnetic latitude at which the fluxes cross this threshold with a positive gradient, as indicated by the blue arrow in the left panel of Figure 2. However, we observe days with enhanced flux in the lower latitude region during modest to strong geomagnetic storm activity causing more than one threshold crossing moving from the equator to the poles, as illustrated by the black box on the right panel of Figure 2. These occurrences have been identified in Kavanagh et al. (2018) as slot region filling events; periods in which MEE penetrate and fill the slot region between the inner and outer radiation belts. These fluxes typically show a slow decay which appears independent of the strongly varying solar wind properties and geomagnetic activity. In such instances, the next positive gradient threshold crossing moving from the equator toward the poles is identified as the equatorward boundary. This will give a systematic lower EEP flux over the hemisphere compared to observations, but justified as the fluxes ignored are precipitated at relatively low latitudes where more efficient photo-chemistry likely renders their chemical imprint insignificant.

We fit a smoothing spline to the data and identify the local maxima and minima. Using these reference points, an algorithm identifies the threshold crossings for days with and without slot filling events for all MLTs and energy channels from 2004 to 2014. The algorithm successfully identified equatorward boundaries from 85% (E1 MLT 0–3) to 94% (E3 MLT 9–12) of the total number of days in the study. As the slot region filling has a slow decay, as seen inside the gray boxes in the 4th panel of Figure 3, there are 489 days for E1 where it was difficult to separate the dynamic boundary from the slot region filling events. We define these days as ambiguous and they

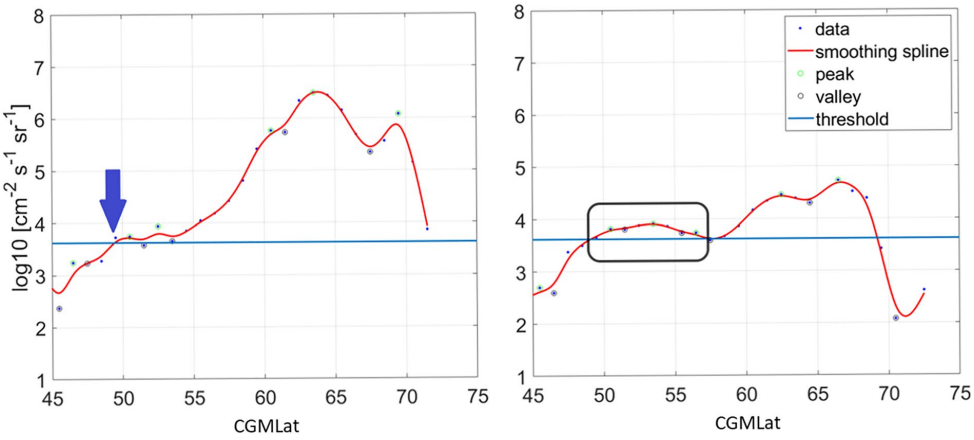

Figure 2. (left) Sample daily flux with one peak above the threshold. (right) Sample daily flux with a double peak above the threshold.

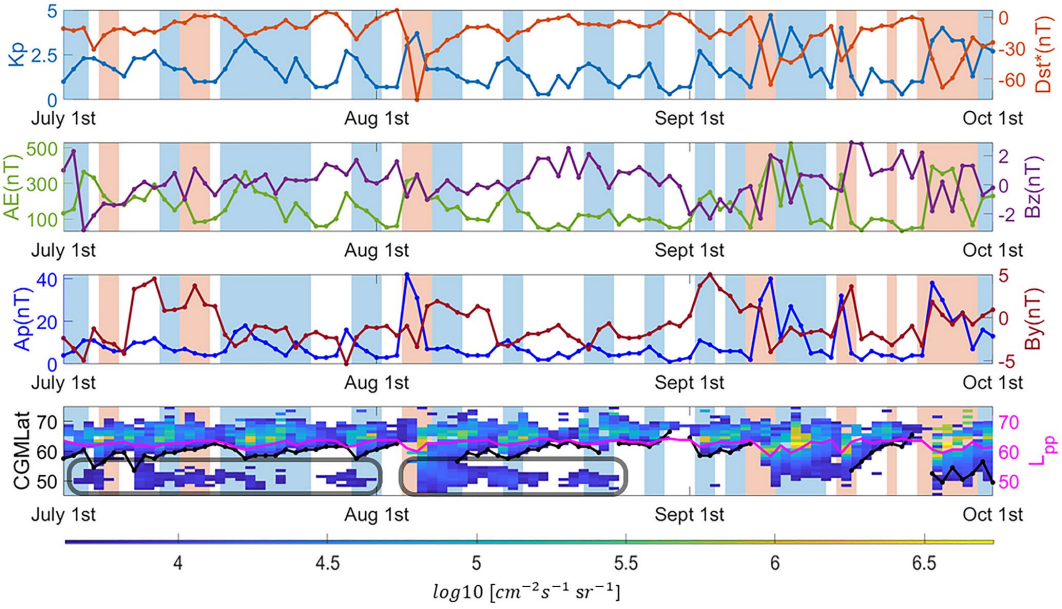

Figure 3. Geomagnetic indices and fluxes above the threshold from July–October 2011. Light red bars represent days with Coronal Mass Ejections, light blue bars days with Co-rotating Interaction Regions, and white bars are days with ambient wind conditions. (1st Panel) Kp on the left *y* axis and pressure corrected Dst (Burton et al., 1975) on the right. (2nd Panel) AE on the left *y* axis and Bz on the right. (3rd Panel) Ap on the left *y* axis and By on the right. (4th Panel) Equatorward boundary identified from the algorithm (black line with dots). The color-plot is fluxes above the threshold for E1 energy channel. The magenta line is the location of plasmapause from (Moldwin et al., 2002) plasmapause model. The gray boxes are slot filling events.

Table 1
Day of Year (DOY) With Ambiguous Boundaries Following the Slot Region Filling Events

2004	2005	2006	2007	2010	2011	2012	2013
1–31	8–25	95–113	29	95–105	76	68–80	145–160
42–48	38–43	127–128	143–149	150–156	149–153	114–122	180–202
70–77	49–51	158–161	184	215–219	156–158	164–166	
95–104	66–73	208–209	192		218–221	169–173	
167	95–110	232–236	344		252–260	191–205	
199	128–179	247–248			298–300	275–277	
200	191–229	334–336				282–295	
205–226	237–264	346–359					
259–268							
314–320							

are not included in the study. Table 1 lists the day of the year (DOY) which are excluded from the analysis, which accounts for 12% of the total days in the study.

4. Predicting the Latitude Boundary

To develop a solar wind parameter or geomagnetic index-based model to predict the equatorward boundaries of MEE precipitation, the parameter that correlates best with the identified boundaries needs to be determined. The parameters considered are pressure-corrected Dst, Kp, AE, Ap, Bz, By, Ey, solar wind flow pressure (P), and solar wind flow speed (v). The pressure-corrected Dst index, Dst*, removes the contribution from the current induced in the magnetopause from the solar wind dynamic pressure. Therefore, Dst* is a better representation of the ring current (Burton et al., 1975):

$$Dst^{*} = Dst - \left(15.8 \times P^{0.5}\right) + 20 \quad (1)$$

Dst* shows the highest Pearson correlation coefficient with the equatorward boundaries of >43 keV MEE precipitation with a value of 0.77. Kp and AE have correlation coefficients of 0.66 and 0.65, respectively. Figure 4 shows the associated scatter plots for the boundaries and Dst*, Kp, and AE. In general, low boundaries (<∼53°) appear to be associated with a wide range of Dst*, Kp, and AE values which might suggest that there are still a few data points associated with the slot region filling events discussed in Section 3. Nevertheless, both the Dst* and AE index have a well-defined upper envelope which clearly moves to lower latitudes as the geomagnetic activity increases. Furthermore, the 90/10 percentile lines in the scatter plots show that Kp has a higher spread of the predicted latitudes of ∼2.74/2.75 compared to AE ∼2.67/2.64 and Dst* ∼ 2.25/2.23. Dst* maintains the best

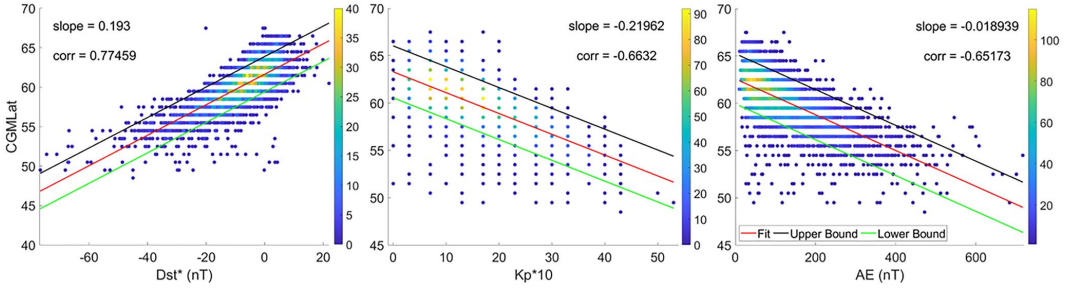

Figure 4. A comparison of the three best correlated indices with the identified boundary. (left) Dst, (center) Kp, and (right) AE. The red line is the linear fit. The green and the black lines are the 10th and the 90th percentiles of the residuals, respectively, when the boundaries predicted by each index is subtracted from the identified boundaries. The color bar represents the number density of data points. The data are from the E1 (>43 keV) energy channel in the Magnetic Local Time sector 0–3.

Table 2
Pearson Correlation Coefficients Between the Equatorward Boundaries and Dst, Kp, and AE*

	E1	E2	E3
Dst* correlation coefficient	**0.77**	**0.72**	**0.52**
Dst* 90th percentile (CGMLat)	2.25	2.24	2.11
Dst* 10th percentile (CGMLat)	−2.23	−2.10	−1.91
Kp correlation coefficient	**0.66**	**0.56**	**0.36**
Kp 90th percentile (CGMLat)	2.74	2.51	2.20
Kp 10th percentile (CGMLat)	−2.75	−2.57	−2.05
AE correlation coefficient	**0.65**	**0.56**	**0.37**
AE 90th percentile (CGMLat)	2.67	2.56	2.24
AE 10th percentile (CGMLat)	−2.64	−2.40	−2.04

Note. The 90th and 10th percentiles are the residuals when the boundaries predicted by each index is subtracted from the identified boundaries for E1, E2, and E3. The bold values indicates the most important values in this table.

correlation coefficient values for the E2 and E3 energy channels, as seen in Table 2. Therefore, the Dst* is selected as the best predictor for the equatorward boundary variability.

A linear model for the boundaries is found by fitting least squares regression on Dst* and using the following equation to calculate the boundaries for each of the MLT regions and energy channels separately:

$$Model\ Boundary = \text{y-intercept} + (Regression\ Coefficient \times Dst^*) \quad (2)$$

The y-intercepts and Pearson correlation coefficients for the three energy channels and six MLT sectors corresponding to Dst* model are listed in Table 3. Figure 5 shows a comparison between the identified and modeled boundaries for each energy channel in the MLT regions 0–3. The model (red dotted line) closely follows the identified boundaries (black dotted line) for all energy channels. As evident from Table 3, there is less variability in the equatorward boundary in the higher energy channels E2 and E3 compared to E1. The empty patches are days from Table 1 that are excluded from this study. Nevertheless, there appears to be a tendency to underestimate the equatorward boundary position in the aftermath of a slot region filling event. Furthermore, the model overestimates the equatorward boundary position in periods of weak activity.

5. Accuracy of the Dst* Model

To systematically explore the performance of the Dst* model, a residual analysis on the difference between the identified and Dst-regressed boundary is performed:

$$Residual\ Boundary = Identified\ Boundary - Model\ Boundary \quad (3)$$

The 3rd panel in Figure 6 shows the residual boundary plot for the E1 energy channel. Eighty percent of the residuals falls within ±2.2° cgmlat. However, the residuals do exhibit a solar cycle bias. The average error is −1.84° cgmlat during the declining phase in 2004, 1.51° cgmlat during the solar minimum year 2009, and 0.18° cgmlat near solar maximum in 2014, causing a potential solar cycle bias of up to 3.35° cgmlat. This systematic bias potentially arises because the quiet time baseline of the Dst index varies with the solar cycle. The Dst index will therefore underestimate or overestimate magnetic activity as a function of the solar cycle (Temerin & Li, 2015).

Considering the solar wind drivers, 12% of the total number of days in the study are dominated by CMEs, 40% of the days are characterized as CIRs, and 48% are described as ambient solar wind conditions. The Dst* model has the best predictability during CIRs as seen in Figure 7. This can also be seen in the 4th panel of Figure 6 where the CIR-dominated period from late 2006 to late 2008 period gives the smallest residuals. The dependency of the solar wind driver might be part of the systematic bias throughout the solar cycle. The frequency of CMEs peaks during solar maximum, HSSs/CIRs are more common in the declining phase, while ambient solar

Table 3
y-Intercepts, Regression Coefficients, and Correlation Coefficients for All Energy Channels and Magnetic Local Time (MLT) Sectors

	E1	E2	E3
MLT 0_3	61.65 + 0.1930Dst*; R = **0.7746**	60.55 + 0.1499Dst*; R = **0.7187**	59.60 + 0.0811Dst*; R = **0.5222**
MLT 3_6	61.76 + 0.1869Dst*; R = **0.7893**	60.62 + 0.1472Dst*; R = **0.7163**	59.48 + 0.1097Dst*; R = **0.6453**
MLT 6_9	61.94 + 0.1709Dst*; R = **0.7239**	60.78 + 0.1326Dst*; R = **0.6581**	59.67 + 0.1077Dst*; R = **0.6297**
MLT 9_12	61.66 + 0.1895Dst*; R = **0.7413**	60.62 + 0.1484; R = **0.6881**	59.54 + 0.1140Dst*; R = **0.6389**
MLT 12_15	61.98 + 0.2008Dst*; R = **0.7475**	60.67 + 0.1517Dst*; R = **0.6838**	59.53 + 0.1201Dst*; R = **0.6457**
MLT 15_18	61.91 + 0.1940Dst*; R = **0.7218**	60.51 + 0.1455Dst*; R = **0.6522**	59.38 + 0.1172Dst*; R = **0.6226**

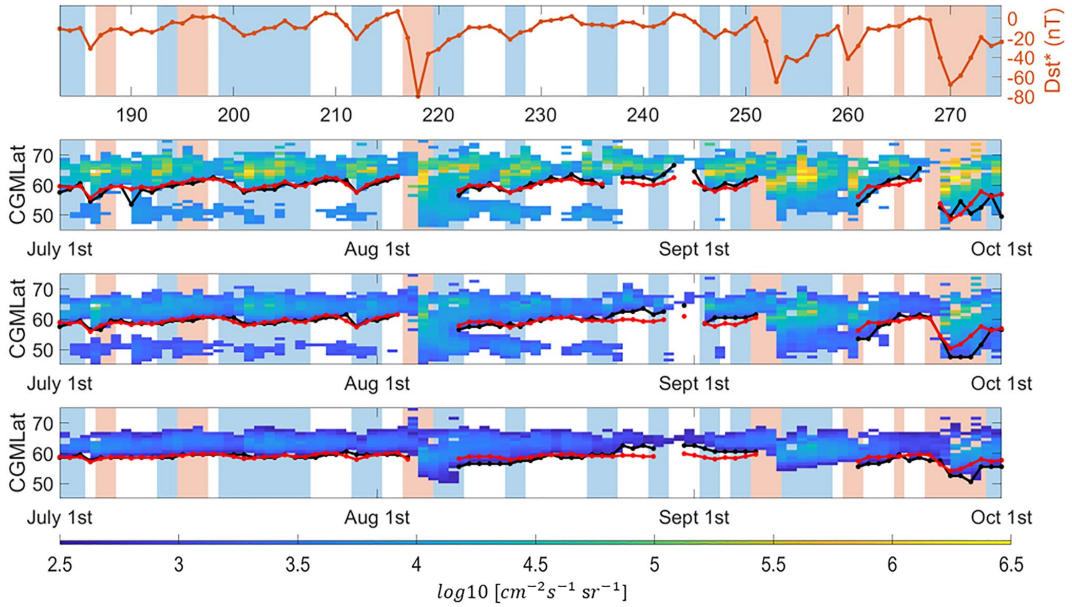

Figure 5. Identified boundaries and modeled boundaries for the E1, E2, and E3 energy channels from July to October 2011. Light red bars represent days with Coronal Mass Ejections, light blue bars days with Co-rotating Interaction Regions, and white bars are days with ambient wind conditions. (1st Panel) Dst index. Equatorward boundary identified from the algorithm (black dotted line) and the modeled equatorward boundary (red dotted line) for energy channels: (2nd Panel) E1, (3rd Panel) E2, and (4th Panel) E3. The color plots are fluxes above the threshold.

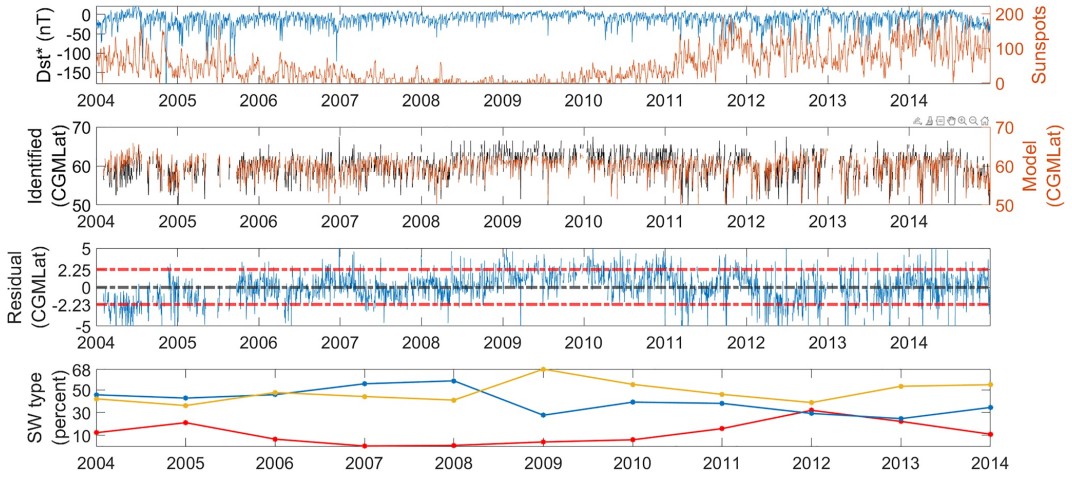

Figure 6. (1st Panel) Dst* (blue) and daily sunspot numbers (red) from 2004 to 2014. (2nd Panel) Identified boundaries (black) and Modeled boundaries (red). (3rd Panel) Residual plot. The red dashed line above and below the 0-line in the 3rd panel represents the 90th percentile value. (4th Panel) Percentage of each solar wind driver for each year in the study. Red line represents Coronal Mass Ejections, blue line Co-rotating Interaction Regions, and yellow line ambient solar wind conditions. The boundaries and residuals are for the E1 energy channel in the Magnetic Local Time sector 0–3 across the 11 years of this study.

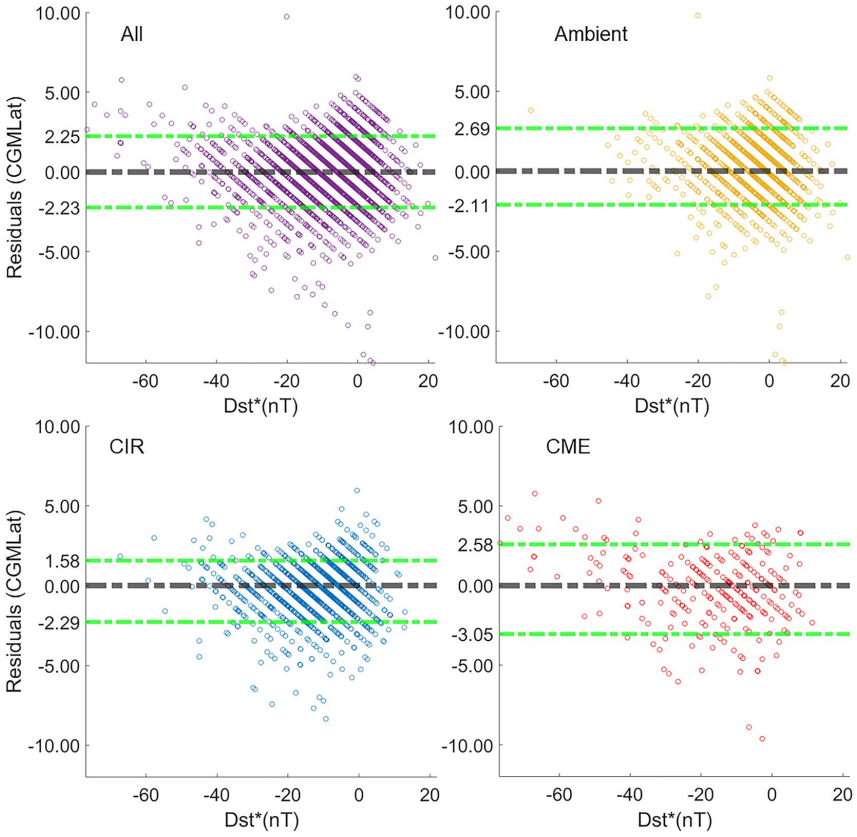

Figure 7. A comparison of the accuracy of the Dst* model for different solar wind drivers. (top left) Residuals for all solar wind drivers. (top right) Residuals for days with ambient solar wind conditions. (bottom left) Residuals for days with Co-rotating Interaction Regions. (bottom right) Residuals for days with Coronal Mass Ejections. The green dashed line above and below the black 0-line are the 90 and 10 percentiles of the residuals, respectively.

Table 4
The Difference Between Identified and Dst Model Boundaries in CGMLat for the Six Investigated Magnetic Local Time (MLT) Sectors and the Three Energy Channels*

	E1	E2	E3
MLT 0–3	2.25, −2.23	2.24, −2.10	2.11, −1.91
MLT 3–6	2.25, −2.22	2.28, −2.22	2.51, −2.51
MLT 6–9	2.47, −2.45	2.38, −2.21	2.52, −2.50
MLT 9–12	2.66, −2.64	2.51, −2.32	2.53, −2.53
MLT 12–15	2.78, −2.67	2.59, −2.34	2.62, −2.57
MLT 15–18	2.79, −2.79	2.58, −2.45	2.69, −2.71

Note. The numbers are the 90th and the 10th percentiles of the residuals.

wind dominates the solar minimum (Richardson et al., 2001). Therefore, as a future effort we will investigate if a model with solar wind drivers as a dependent variable can potentially reduce the solar cycle bias. It is also worth considering different geomagnetic indices and solar wind parameters during different phases of the solar cycle as they might be better at predicting MEE precipitation for different solar wind drivers (Borovsky & Denton, 2006).

Exploring the MLT dependence of the Dst* model, the midnight sector MLT 0–3 was found to have the best predictability, and the afternoon sector MLT 15–18 the highest uncertainty in all energy channels. The relatively highest uncertainty in the afternoon sector could be related to the Relativistic Electron Precipitation (REP) occurring in the MLT sector 14–20. These events have been shown by Smith et al. (2016) to be correlated with multiple solar wind parameters and geomagnetic indices, tying them to EMIC-driven precipitation. Table 4 shows the 90th and 10th percentiles of residuals for all MLT sectors and energy channels used in this study.

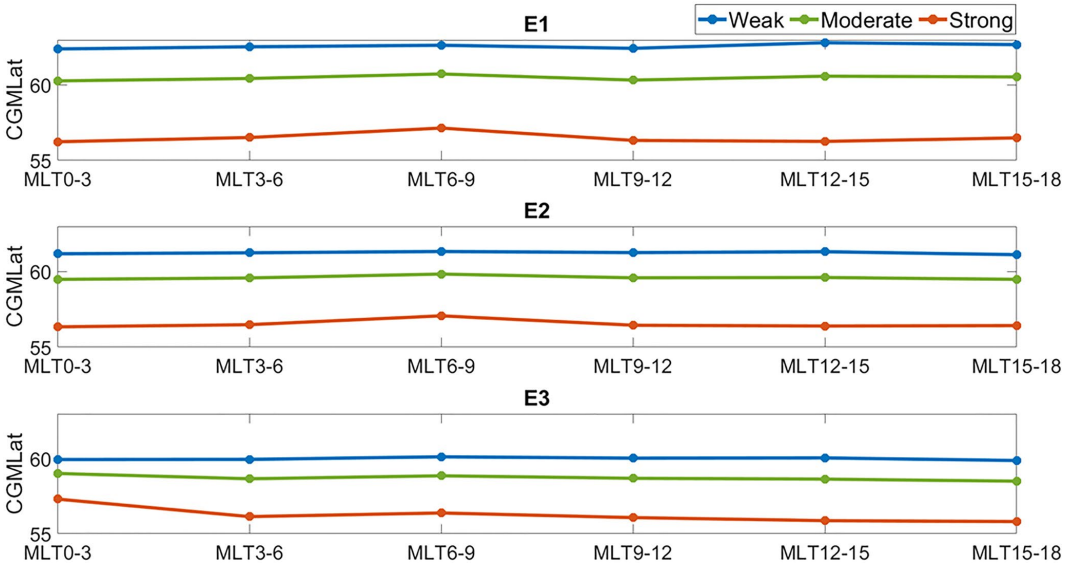

Figure 8. Variation of the median boundary of the Dst* model in each Magnetic Local Time sector and each energy channel for different geomagnetic activity levels.

The variability of the median boundary with respect to MLT and energy for different levels of geomagnetic activity is also investigated (Figure 8). All geomagnetic activity above the 80th percentile of the average Dst (0.89 nT) are defined as weak, while activity below the 20th percentile (−20.65 nT) are considered strong. Everything in between is categorized as a moderate activity. With increasing strength of Dst*, the boundaries are pushed equatorward as expected for all three energy channels. The E1 channel is the most dynamic of the three and exhibits the most poleward boundary, followed by E2, and lastly E3. Nevertheless, no systematic variation of the MEE precipitating boundaries as a function of MLT is observed for the same level of geomagnetic activity consistent with Table 4. The weak MLT dependency might be due to that MEE will travel multiple times around the Earth before being lost to the atmosphere. By using daily resolved MEE fluxes, the MLT variability associated with for example, isolated substorms will be averaged out. Hence, a higher temporal resolution might be needed to observe any notable MLT dependency for the precipitating latitudes.

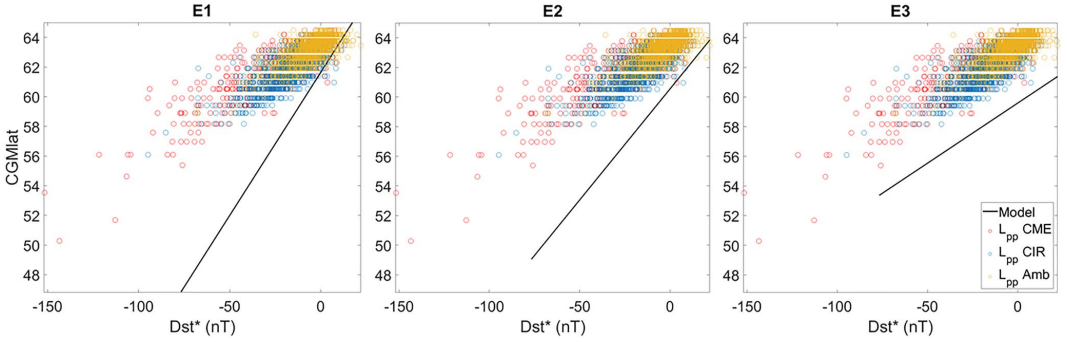

Figure 9. Location of the plasmapause estimated from Moldwin et al. (2002)'s plasmapause model are scatter-plotted for different solar wind drivers (red for Coronal Mass Ejection, blue for Co-rotating Interaction Region, and yellow for ambient). The equatorward boundaries predicted by the Dst* model is the black line. The data are for E1, E2, and E3 energy channels from left to right, respectively.

A comparison of the Dst* model with Moldwin et al. (2002)'s plasmapause model for the E1, E2, and E3 channels is presented in Figure 9. The solid black line represents the equatorward boundary predicted by the Dst* model. The red, blue, and yellow scatterplots depict the location of the plasmapause during CME, CIR, and ambient solar wind conditions. For the E1 channel, the more negative the Dst* index becomes, the larger the deviation is between the location of the plasmapause with respect to the Dst* model. Hence, the largest discrepancies are naturally found predominantly during days with CMEs. The location of the plasmapause is the closest to the Dst* model during ambient solar wind conditions compared to CIRs and CMEs. The differences between the plasmapause model and the Dst* model is less prominent in the E3-channel as the equatorward boundary is not as dynamic compared to the E1-channel, as shown in the 4th panel of Figure 5. Therefore, the location of the plasmapause in E3 is closer to the equatorward boundary than in E1, and appears to have a similar dependency on Dst*.

van de Kamp et al. (2016) and van de Kamp et al. (2018) use Moldwin et al. (2002)'s plasmapause model dependent on Ap, to predict the equatorward boundary of the >30 keV electron flux. Furthermore, van de Kamp et al. (2018) models the precipitation as a function of MLT. van de Kamp et al. (2018) finds a dependence of MEE flux on MLT in agreement with previous studies such as Wissing et al. (2008), Meredith et al. (2011), and Ødegaard et al. (2017). However, since Moldwin et al. (2002)'s plasmapause model is independent of MLT, the variation of precipitation boundaries with geomagnetic activity remains almost the same across all MLT sectors. This is consistent with Figure 8. Moreover, the equatorward boundaries predicted by Dst* model predicts are energy dependent, where the equatorward extent of the precipitation is pushed toward lower latitudes for higher electron energies. Therefore, based on Figure 9, it is likely that the discrepancy between the precipitation region in van de Kamp et al. (2016) and the Dst* model will increase with higher activity for E1, but have a more consistent discrepancy for the higher energies E2 and E3. We also note that the MLT sectors 18–21 and 21–24 are omitted in this study because of insufficient data.

In the HEPPA III intercomparison study in Nesse Tyssøy et al. (2022), a comparison of the latitudinal extent of the MEE precipitation region is done for eight different ionization rate estimates including the van de Kamp et al. (2016) model and the BLC rates used here. For the respective period, the van de Kamp et al. (2016) and plasmapause model provide the most prudent estimate of the equatorward boundary compared to the other ionization rate estimates. In particular, the ionization rates based on both the 0° and 90° telescopes, such as the BLC fluxes shown here, predict a much larger extent of the equatorward boundaries, and will hence lead to a stronger chemical impact.

6. Conclusion

This study investigates the variation of equatorward boundary of precipitating MEE electrons with respect to different geomagnetic indices and solar wind parameters. BLC measurements of >43, >114, and >292 keV MEE fluxes from MEPED detectors from 2004 to 2014 are used to develop a geomagnetic index-based model. This model is capable of predicting the equatorward extend of MEE precipitation in the NH over the geomagnetic latitude band of 45°–75°. An algorithm based on a threshold level identifies boundaries for the E1(>43 keV), E2(>114 keV), and E3(>292 keV) energy channels for MLT sectors 0–3, 3–6, 6–9, 9–12, 12–15, and 15–18. We find Dst* to be the best predictor of the identified boundaries compared to Kp, AE, Ap, Bz, By, Ey, solar wind flow pressure (P), and solar wind flow speed (v). The model uses a linear regression of Dst* to estimate equatorward boundaries with an error estimate of ±2.2° cgmlat. The model has a solar cycle bias from underestimation and overestimation of magnetic activity as a function of the solar cycle. The model also exhibits a bias based on solar wind drivers thus exacerbating the Dst* bias. The equatorward boundaries are pushed to lower latitudes with an increase in strength of the geomagnetic activity. However, no significant change in the median boundary as function of MLT is observed for the same level of geomagnetic activity. The more negative the Dst* index becomes, the larger the E1 boundaries deviate from Moldwin et al. (2002)'s plasmapause model and to a greater extent for CME and CIR events compared to ambient days.

In future work, we will explore to which degree the type of solar wind driver as a dependent variable, can improve the accuracy of a geomagnetic index based model. Furthermore, the choice to exclude the slot filling events implies a systematic underestimation of the hemispheric electron energy input at mid and low geomagnetic latitudes. This will be quantified in a future study, alongside an assessment of the chemical imprint considering the geographic latitudes and level of photolysis. Alongside predictions of the intensity of the MEE fluxes (Tyssoy, 2021), the Dst* model will be a key element for constructing a realistic estimate of EEP variability to be applied in atmosphere climate models. Moreover, the model can also be applied to examine the importance of the location of the plasmapause in moderating wave-particle interactions that lead to precipitation and how the precipitation boundaries might relate to the inner edge of the outer radiation belts.

Data Availability Statement

The NOAA/POES MEPED data used in this study are available from the National Oceanic and Atmospheric Administration (https://www.ngdc.noaa.gov/stp/satellite/poes/dataaccess.html). The MLT and CGMLat sorted MEPED data are available at Zenodo via https://doi.org/10.5281/zenodo.6590387. Geomagnetic indices and solar wind parameters were obtained from NASA Omniweb at https://omniweb.gsfc.nasa.gov/form/dx1.html.

Acknowledgments
The study is supported by the Norwegian Research Council (NRC) under contract nos. 223252 and 302040. HNT further acknowledge the Young CAS (Centre for Advanced Studies) fellow program. IGR acknowledges support from the ACE mission. The authors thank the Space Weather Prediction Center (SWPC), NOAA for providing the MEPED data.

References

Andersson, M. E., Verronen, P. T., Wang, S., Rodger, C. J., Clilverd, M. A., & Carson, B. R. (2012). *Precipitating radiation belt electrons and enhancements of mesospheric hydroxyl during 2004–2009* (Vol. 117). Blackwell Publishing Limited. https://doi.org/10.1029/2011JD017246

Baumgaertner, A. J., Seppälä, A., Jöckel, P., & Clilverd, M. A. (2011). Geomagnetic activity related NO_x enhancements and polar surface air temperature variability in a chemistry climate model: Modulation of the NAM index. *Atmospheric Chemistry and Physics*, *11*(9), 4521–4531. https://doi.org/10.5194/acp-11-4521-2011

Borovsky, J. E., & Denton, M. H. (2006). Differences between CME-driven storms and CIR-driven storms. *Journal of Geophysical Research*, *111*(A7), A07S08. https://doi.org/10.1029/2005JA011447

Burton, R., McPherron, R., & Russell, C. (1975). An empirical relationship between interplanetary conditions and Dst. *Journal of Geophysical Research*, *80*(31), 4204–4214. https://doi.org/10.1029/JA080i031p04204

Carson, B. R., Rodger, C. J., & Clilverd, M. A. (2013). POES satellite observations of EMIC-wave driven relativistic electron precipitation during 1998–2010. *Journal of Geophysical Research: Space Physics*, *118*(1), 232–243. https://doi.org/10.1029/2012JA017998

Damiani, A., Funke, B., López-Puertas, M., Santee, M. L., Cordero, R. R., & Watanabe, S. (2016). Energetic particle precipitation: A major driver of the ozone budget in the Antarctic upper stratosphere. *Geophysical Research Letters*, *43*(7), 3554–3562. https://doi.org/10.1002/2016GL068279

Evans, D., & Greer, M. (2000). *Polar orbiting environmental satellite space environment monitor-2: Instrument description and archive data documentation*. U.S. Department of Commerce, National Oceanic and Atmospheric Administration, Oceanic and Atmospheric Research Laboratories, Space Environment Center.

Friedel, R., Reeves, G., & Obara, T. (2002). Relativistic electron dynamics in the inner magnetosphere—A review. *Journal of Atmospheric and Solar-Terrestrial Physics*, *64*(2), 265–282. https://doi.org/10.1016/S1364-6826(01)00088-8

Gasque, L. C., Millan, R. M., & Shekhar, S. (2021). Statistically determining the spatial extent of relativistic electron precipitation events using 2-s polar-orbiting satellite data. *Journal of Geophysical Research: Space Physics*, *126*(4), e2020JA028675. https://doi.org/10.1029/2020JA028675

Hardman, R., Clilverd, M. A., Rodger, C. J., Brundell, J. B., Duthie, R., Holzworth, R. H., et al. (2015). A case study of electron precipitation fluxes due to plasmaspheric hiss. *Journal of Geophysical Research: Space Physics*, *120*(8), 6736–6748. https://doi.org/10.1002/2015JA021429

Kavanagh, A. J., Cobbett, N., & Kirsch, P. (2018). Radiation belt slot region filling events: Sustained energetic precipitation into the mesosphere. *Journal of Geophysical Research: Space Physics*, *123*(9), 7999–8020. https://doi.org/10.1029/2018JA025890

Kennel, C. F., & Petschek, H. E. (1966). Limit on stably trapped particle fluxes. *Journal of Geophysical Research*, *71*, 1–28.

Maliniemi, V., Asikainen, T., Salminen, A., & Mursula, K. (2019). Assessing North Atlantic winter climate response to geomagnetic activity and solar irradiance variability. *Quarterly Journal of the Royal Meteorological Society*, *145*(725), 3780–3789. https://doi.org/10.1002/qj.3657

Maliniemi, V., Nesse Tyssøy, H., Smith-Johnsen, C., Arsenovic, P., & Marsh, D. R. (2021). Effects of enhanced downwelling of NO_x on Antarctic upper-stratospheric ozone in the 21st century. *Atmospheric Chemistry and Physics*, *21*(14), 11041–11052. https://doi.org/10.5194/acp-21-11041-2021

Meredith, N. P., Horne, R. B., Lam, M. M., Denton, M. H., Borovsky, J. E., & Green, J. C. (2011). Energetic electron precipitation during high-speed solar wind stream driven storms. *Journal of Geophysical Research: Space Physics*, *116*(5), A05223. https://doi.org/10.1029/2010JA016293

Millan, R., & Thorne, R. (2007). Review of radiation belt relativistic electron losses. *Journal of Atmospheric and Solar-Terrestrial Physics*, *69*(3), 362–377. https://doi.org/10.1016/j.jastp.2006.06.019

Moldwin, M. B., Downward, L., Rassoul, H., Amin, R., & Anderson, R. (2002). A new model of the location of the plasmapause: CRRES results. *Journal of Geophysical Research*, *107*(A11), 1339. https://doi.org/10.1029/2001JA009211

Nesse Tyssøy, H., Sandanger, M. I., Ødegaard, L. K., Stadsnes, J., Aasnes, A., & Zawedde, A. E. (2016). Energetic electron precipitation into the middle atmosphere—Constructing the loss cone fluxes from MEPED POES. *Journal of Geophysical Research A: Space Physics*, *121*(6), 5693–5707. https://doi.org/10.1002/2016JA022752

Nesse Tyssøy, H., Sinnhuber, M., Asikainen, T., Bender, S., Clilverd, M. A., Funke, B., et al. (2022). HEPPA III intercomparison experiment on electron precipitation impacts: 1. Estimated ionization rates during a geomagnetic active period in April 2010. *Journal of Geophysical Research: Space Physics*, *127*(1), e2021JA029466. https://doi.org/10.1029/2021JA029128

Ødegaard, L.-K. G., Nesse, T. H., Sandanger, J., Stadsnes, M. I., & Søraas, F. (2016). Space Weather impact on the degradation of NOAA POES MEPED proton detectors. *Journal of Space Weather and Space Climate*, *6*, A26. https://doi.org/10.1051/swsc/2016020

Ødegaard, L.-K. G., Nesse, T. H., Søraas, F., Stadsnes, J., & Sandanger, M. I. (2017). Energetic electron precipitation in weak to moderate corotating interaction region-driven storms. *Journal of Geophysical Research: Space Physics*, *122*(3), 2900–2921. https://doi.org/10.1002/2016JA023096

Pierrard, V., Botek, E., Ripoll, J. F., Thaller, S. A., Moldwin, M. B., Ruohoniemi, M., & Reeves, G. (2021). Links of the plasmapause with other boundary layers of the magnetosphere: Ionospheric convection, radiation belt boundaries. *Auroral Oval Frontiers in Astronomy and Space Sciences*, *8*, 728531. https://doi.org/10.3389/fspas.2021.728531

Richardson, I. G. (2018). *Solar wind stream interaction regions throughout the heliosphere* (Vol. 15). Springer International Publishing. https://doi.org/10.1007/s41116-017-0011-z

Richardson, I. G., & Cane, H. V. (2012). Near-earth solar wind flows and related geomagnetic activity during more than four solar cycles (1963–2011). *Journal of Space Weather and Space Climate*, *2*, A02. https://doi.org/10.1051/swsc/2012003

Richardson, I. G., Cliver, E. W., & Cane, H. V. (2001). Sources of geomagnetic storms for solar minimum and maximum conditions during 1972–2000. *Geophysical Research Letters*, *28*(13), 2569–2572. https://doi.org/10.1029/2001GL013052

Rodger, C., Clilverd, M. A., Thomson, N. R., Gamble, R. J., Seppälä, A., Turunen, E., et al. (2007). Radiation belt electron precipitation into the atmosphere: Recovery from a geomagnetic storm. *Journal of Geophysical Research: Space Physics*, *112*(A11), A12304. https://doi.org/10.1029/2007JA012383

Rodger, C. J., Clilverd, M. A., Green, J. C., & Lam, M. M. (2010). Use of POES SEM-2 observations to examine radiation belt dynamics and energetic electron precipitation into the atmosphere. *Journal of Geophysical Research: Space Physics*, *115*(4), A12304. https://doi.org/10.1029/2008JA014023

Sandanger, M., Ødegaard, L., Hn, T., Stadsnes, J., Søraas, F., Oksavik, K., & Aarsnes, K. (2015). In-flight calibration of NOAA POES proton detectors—Derivation of the MEPED correction factors. *Journal of Geophysical Research: Space Physics*, *120*(11), 9578–9593. https://doi.org/10.1002/2015JA021388

Seppälä, A., Randall, C., Clilverd, M., Rozanov, E., & Rodger, C. (2009). Geomagnetic activity and polar surface air temperature variability. *Journal of Geophysical Research: Space Physics*, *114*(A10), A014029. https://doi.org/10.1029/2008JA014029

Shekhar, S., Millan, R., & Smith, D. (2017). A statistical study of the spatial extent of relativistic electron precipitation with polar orbiting environmental satellites. *Journal of Geophysical Research: Space Physics*, *122*(11), 274–311. https://doi.org/10.1002/2017JA024716

Shelley, E. G., Johnson, R. G., & Sharp, R. D. (1972). Satellite observations of energetic heavy ions during a geomagnetic storm. *Journal of Geophysical Research*, *77*(31), 6104–6110. https://doi.org/10.1029/ja077i031p06104

Smith, D. M., Casavant, E. P., Comess, M. D., Liang, X., Bowers, G. S., Selesnick, R. S., et al. (2016). The causes of the hardest electron precipitation events seen with SAMPEX. *Journal of Geophysical Research: Space Physics*, *121*(9), 8600–8613. https://doi.org/10.1002/2016JA022346

Solomon, S., Crutzen, P. J., & Roble, R. G. (1982). Photochemical coupling between the thermosphere and the lower atmosphere: 1. Odd nitrogen from 50 to 120 km. *Journal of Geophysical Research*, *87*(C9), 7206–7220. https://doi.org/10.1029/JC087iC09p07206

Temerin, M., & Li, X. (2015). The Dst index underestimates the solar cycle variation of geomagnetic activity. *Journal of Geophysical Research: Space Physics*, *120*(7), 5603–5607. https://doi.org/10.1002/2015JA021467

Theodoridis, G. C., & Paolini, F. R. (1967). Pitch angle diffusion of relativistic outer belt electrons. *Annales de Geophysique*, *23*, 375–381.

Tyssøy, H. N., Haderlein, A., Sandanger, M., & Stadsnes, J. (2019). Intercomparison of the POES/MEPED loss cone electron fluxes with the CMIP6 parametrization. *Journal of Geophysical Research: Space Physics*, *124*(1), 628–642. https://doi.org/10.1029/2018JA025745

Tyssøy, H. N., Partamies, N., Babu, E. M., Smith-Johnsen, C., & Salice, J. A. (2021). The Predictive Capabilities of the Auroral Electrojet Index for Medium Energy Electron Precipitation. *Frontiers in Astronomy and Space Sciences*, *8*. https://doi.org/10.3389/fspas.2021.714146

Van Allen, J. A. (1959). The geomagnetically trapped corpuscular radiation. *Journal of Geophysical Research*, *64*(11), 1683–1689. https://doi.org/10.1029/JZ064i011p01683

van de Kamp, M., Rodger, C. J., Seppälä, A., Clilverd, M. A., & Verronen, P. T. (2018). An updated model providing long-term data sets of energetic electron precipitation, including zonal dependence. *Journal of Geophysical Research: Atmospheres*, *123*(17), 9891–9915. https://doi.org/10.1029/2017JD028253

van de Kamp, M., Seppälä, A., Clilverd, M. A., Rodger, C. J., Verronen, P. T., & Whittaker, I. C. (2016). A model providing long-term data sets of energetic electron precipitation during geomagnetic storms. *Journal of Geophysical Research*, *121*(20), 12520. https://doi.org/10.1002/2015JD024212

Verronen, P. T., Rodger, C. J., Clilverd, M. A., & Wang, S. (2011). First evidence of mesospheric hydroxyl response to electron precipitation from the radiation belts. *Journal of Geophysical Research*, *116*(7), D07307. https://doi.org/10.1029/2010JD014965

Voss, H., Walt, M., Imhof, W., Mobilia, J., & Inan, U. (1998). Satellite observations of lightning-induced electron precipitation. *Journal of Geophysical Research*, *103*(A6), 11725–11744. https://doi.org/10.1029/97JA02878

Whittaker, I. C., Clilverd, M. A., & Rodger, C. J. (2014). Characteristics of precipitating energetic electron fluxes relative to the plasmapause during geomagnetic storms. *Journal of Geophysical Research: Space Physics*, *119*(11), 8784–8800. https://doi.org/10.1002/2014JA020446

Wissing, J. M., Bornebusch, J. P., & Kallenrode, M. B. (2008). Variation of energetic particle precipitation with local magnetic time. *Advances in Space Research*, *41*(8), 1274–1278. https://doi.org/10.1016/j.asr.2007.05.063

Yando, K., Millan, R. M., Green, J. C., & Evans, D. S. (2011). A Monte Carlo simulation of the NOAA POES medium energy proton and electron detector instrument. *Journal of Geophysical Research: Space Physics*, *116*(A10), 10231. https://doi.org/10.1029/2011JA016671

Zawedde, A. E., Nesse Tyssøy, H., Stadsnes, J., & Sandanger, M. I. (2019). Are EEP events important for the tertiary ozone maximum? *Journal of Geophysical Research: Space Physics*, *124*(7), 5976–5994. https://doi.org/10.1029/2018JA026201

Zhang, J., Richardson, I., Webb, D., Gopalswamy, N., Huttunen, E., Kasper, J. C., et al. (2007). Solar and interplanetary sources of major geomagnetic storms ($Dst \leq -100$ nT) during 1996–2005. *Journal of Geophysical Research: Space Physics*, *112*(A10), A10102. https://doi.org/10.1029/2007JA012321

Paper II

An Updated Geomagnetic Index-based Model for Determining the Latitudinal Extent of Energetic Electron Precipitation

E.M. Babu, H. Nesse, S.M. Hatch, N. Olsen, J.A. Salice, and I.G. Richardson. *Journal of Geophysical Research: Space Physics*, (Under Review as of April 2023)

Paper III

Energetic Electron Precipitation during Slot Region Filling Events

H. Nesse, E.M. Babu, J.A. Salice, and B. Funke. *Journal of Geophysical Research: Space Physics*, (Under Review as of April 2023)

Paper IV

The Predictive Capabilities of the Auroral Electrojet Index for Medium Energy Electron Precipitation

H. Nesse Tyssøy, N. Partamies, E.M. Babu, C. Smith-Johnsen, and J.A. Salice.
Frontiers in Astronomy and Space Sciences, doi:10.3389/fspas.2021.714146 (2021)

frontiers in Astronomy and Space Sciences

ORIGINAL RESEARCH
published: 04 October 2021
doi: 10.3389/fspas.2021.714146

The Predictive Capabilities of the Auroral Electrojet Index for Medium Energy Electron Precipitation

H. Nesse Tyssøy[1]*, *N. Partamies*[1,2], *E. M. Babu*[1], *C. Smith-Johnsen*[1] *and J. A. Salice*[1]

[1]Birkeland Centre for Space Science, Department of Physics and Technology, University of Bergen, Bergen, Norway, [2]Department of Arctic Geophysics, The University Centre in Svalbard (UNIS), Longyearbyen, Norway

The chemical imprint of the energetic electron precipitation on the atmosphere is now acknowledged as a part of the natural forcing of the climate system. It has, however, been questioned to which degree current proxies are able to quantify the medium energy electron (MEE) (≳30 keV) precipitation and the associated daily and decadal variability. It is particularly challenging to model the high energy tail (≳300 keV) of MEE, both in terms of the intensity as well as the timing. This study explores the predictive capabilities of the AE index for the MEE precipitation. MEE measurements from the NOAA/POES over a full solar cycle from 2004 to 2014 are applied. We combine observations from the MEPED 0° and 90° detectors together with theory of pitch angle diffusion by wave-particle interaction to estimate the precipitating fluxes. To explore the energy dependent time scales, each of the MEPED energy channels, > 43, >114, and >292 keV are evaluated independently. While there is a strong correlation between the daily resolved AE index and >43 keV fluxes, it is a poor predictor for the >292 keV fluxes. We create new AE based MEE proxies by accumulating the AE activity over multiple days, including terms counting for the associated lifetimes. The results indicate that AE based proxies can predict at least 70% of the observed MEE precipitation variance at all energies. The potential link between the AE index, substorms and the MEE precipitation is discussed.

Keywords: energetic electron precipitation, medium energy electrons, outer radiation belt, auroral electrojet index, substorms

OPEN ACCESS

Edited by:
Scott Alan Thaller, University of Colorado Boulder, United States

Reviewed by:
Victor Sergeev, Saint Petersburg State University, Russia
Ingmar Sandberg, Space Applications and Research Consultancy (SPARC), Greece

***Correspondence:**
H. Nesse Tyssøy
hilde.nesse@uib.no

Specialty section:
This article was submitted to Space Physics, a section of the journal Frontiers in Astronomy and Space Sciences

Received: *24 May 2021*
Accepted: *15 September 2021*
Published: *04 October 2021*

Citation:
Tyssøy HN, Partamies N, Babu EM, Smith-Johnsen C and Salice J (2021) The Predictive Capabilities of the Auroral Electrojet Index for Medium Energy Electron Precipitation. Front. Astron. Space Sci. 8:714146. doi: 10.3389/fspas.2021.714146

1 INTRODUCTION

Precipitating auroral electrons (≲ 30 keV) and protons (≲ 1 MeV) from the plasma sheet will ionize the lower thermosphere and upper mesosphere. Medium energy electrons (MEE) (≳ 30 keV) from the radiation belts have sufficient energy to penetrate deep into the mesosphere (Turunen et al., 2009). The associated ionization enhances the production rate of NOx and HOx gasses, which in turn can reduce ozone in catalytic processes (e.g., Sætre et al., 2004; Andersson et al., 2012; Sinnhuber et al., 2016; Zawedde et al., 2016). During polar winter, the chemical impact can be long lasting and influence temperatures, winds, and wave propagation. This chain of reactions can impact the strength of the stratospheric polar vortex, causing a dynamical signal that may propagate all the way down to the surface (Seppälä et al., 2013; Maliniemi et al., 2016). To account for this natural solar forcing of the atmosphere, a parametrization of energetic electron precipitation is – for the first time – part of the official input to the Coupled Model Intercomparison Project phase 6 (CMIP 6) going into the Intergovernmental Panel on

Climate Change sixth assessment report (Matthes et al., 2017). The MEE ionization rate dataset therein is based on observations from the Medium Energy Proton and Electron Detector (MEPED) instrument on board the NOAA/Polar Orbiting Environmental Satellites (POES), and the geomagnetic Ap index is used as a proxy to provide an extended time series beyond the satellite observation period (van de Kamp et al., 2016). There is, however, an active discussion to what extent this approach gives a representative flux and ionization rate level (Mironova et al., 2019; Nesse Tyssøy et al., 2019; Pettit et al., 2019; Clilverd et al., 2020). The CMIP6 flux is a general underestimate, largely ascribed to the use of the vertical (0°) detector on MEPED which only covers a small fraction of the loss cone (Nesse Tyssøy et al., 2019). Recent studies, however, also point out that the role of substorms in driving MEE precipitation is not readily explained by a single magnetic index value. Hence, substorms is one of the main unknowns in the existing proxies when considering the MEE precipitation and especially its high energy tail (≳ 300 keV) (Partamies et al., 2021).

Several processes in the magnetosphere contribute to the driving of the MEE precipitation. A globally induced electric field during southward interplanetary magnetic field accelerates and transports electrons from the magnetotail into the inner magnetosphere where they become a part of the radiation belts. In parallel, localized transient-induced electric fields, created from the magnetotail collapse during substorm activity, also energize and increase the MEE population in the radiation belts. So-called seed particles of 10–100 s keV can be directly injected into the inner magnetosphere during a substorm (Li et al., 2009; Jaynes et al., 2015). Further acceleration also occurs as the injection of source particles (tens of keV) gives rise to Very Low Frequency (VLF) wave growth, which may resonantly interact and accelerate radiation belt electrons to MEE (Borovsky & Yakymenko, 2017). Repeated substorm activity has been shown to be particularly important for MEE fluxes (Rodger et al., 2016; Partamies et al., 2021), possibly due the induction electric field directly energizing the trapped electrons as they drift across the nightside during substorm expansion phases (Dai et al., 2014). Partamies et al. (2021) identified the substorm occurrence by a regional AE index and used cosmic noise absorption enhancement as a measure of the MEE precipitation. They showed that for multi-night substorm events, the first night was rarely associated with the most intense absorption. Instead, the high-energy electron population, needed to cause the strongest absorption, was built up over one to two additional nights of substorm activity. This was further confirmed by MEPED *in situ* particle spectra. In the expansion phases the bulk of the spectra showed a local maximum flux in the range of a few keV to 10 keV, while in the recovery phases higher fluxes were seen in the range of tens of keV to hundreds of keV. Based on the SuperMAG substorm event list, Rodger et al. (2016) constructed a superposed epoch analysis differing between isolated and recurrent events. Even though their main focus was the trapped MEE fluxes, they also showed higher precipitating MEE fluxes in the epoch analysis for the recurrent events compared to isolated events, in particular with respect to the high energy tail (>300 keV). Although not commented on, Figure A1 in Rodger et al. (2016) showed an instant effect as well as a gradual build-up over the consecutive days. Seppälä et al. (2015) used the substorm model developed by Beharrell et al. (2015) to investigate the production of HOx and NOx and the subsequent depletion of mesospheric ozone with the Sondakylä Ion and Neutral Chemistry model (Turunen et al., 2009). The peak loss of mesospheric ozone was observed during the third and fourth day in the period of the repetitive substorm activity. This implies that the creation of MEE precipitation involves processes with various time constants and potentially accumulated effects, where there are increasing delays in flux buildup with energy (Boynton et al., 2016; Ødegaard et al., 2017; Stepanov et al., 2021).

Out of the International Association of Geomagnetism and Aeronomy (IAGA) recognized magnetic indices, the Auroral Electrojet (AE) index best corresponds to substorm activity. The AE index goes back to the 1960s and is constructed from the horizontal magnetic field component recorded with 1-min time resolution at 10–13 magnetic observatories located under the average auroral oval in the Northern Hemisphere (NH) (geomagnetic latitudes 60°–70°) (Davis & Sugiura, 1966; Kauristie et al., 2017, and references therein). The upper and lower envelope curves are defined to be the AU and AL indices which characterize the intensity of eastward and westward electrojets, respectively. The difference, AU—AL, defines the AE-index (Davis & Sugiura, 1966). The magnetotail energy release associated with the substorm expansion phase affects the intensity and spatial distribution of electric currents in the auroral oval region. In particular, the substorm current wedge causes sudden enhancements in the westward electrojet (Kauristie et al., 2017).

In this study, we explore the prediction capability of AE in regard to MEE precipitating fluxes. We combine observations from both the MEPED 0° and 90° detectors together with the theory of pitch angle diffusion by wave-particle interaction to quantify the MEE flux in the bounce loss cone. We treat the MEPED energy channels, > 43, >114, and >292 keV, independently to explore their associated time delays in respect to the geomagnetic activity. The objective is to determine the potential of AE as a proxy for MEE precipitating fluxes with a particular focus on the high energy tail. The paper is organised as follows: **Section 2** describes the MEPED detectors and the methods applied to estimate the loss cone fluxes. It provides a short introduction to the AE index followed by a comparison between the AE index and the SuperMAG substorms list from the period 2004–2014. **Section 3** starts with a simple inspection of the correlation between the AE index and the MEE fluxes, where the investigation of time delays and build-up effects points toward a more advanced model. **Section 4** provides a discussion of the implication of the results and the potential role of substorms as the physical process linking the AE based proxies and the MEE fluxes.

2 DATA AND METHODS

2.1 The Medium Energy Electrons Loss Cone Fluxes

The MEPED instrument is mounted on the NOAA/POES series and three EUMETSAT/MetOp spacecraft (Evans & Greer, 2004). The satellites are Sun-synchronous, low-altitude (~ 850 km), polar orbiting spacecrafts. Their orbital period is about 100 min, resulting in 14–15 orbits for each satellite each day. The combined measurements offer a long, near continuous observation of MEE from 1979 until today. During the latest decades a constellation of up to six operating satellites has allowed for a more global magnetic local time coverage.

The MEPED instrument consists of two directional electron telescopes and two directional proton telescopes, as well as an omni-directional detector for very energetic protons measured over a wide range of angles (Evans & Greer, 2004). The field of view of both the 0° and 90° telescopes is 30° full width. The nominal energy limits of the MEPED telescopes are given as > 30, >100, and >300 keV. The true detector efficiency, however, will depend on the incoming energy spectrum (Yando et al., 2011). Ødegaard et al. (2017) utilize the geometric factors given in Yando et al. (2011) to determine new optimized effective integral energy limits >43, >114, and >292 keV and associated geometric factors based on a series of realistic power law and exponential spectra. Furthermore, the spurious response to contaminating protons is accounted for. The observed proton fluxes are first corrected for degradation due to radiation damage by applying correction factors derived by Sandanger et al. (2015) and Ødegaard et al. (2016). Subsequently, a monotonic piecewise cubic Hermite interpolating polynomial is applied to the corrected proton fluxes. The proton flux in the energy ranges known to impact the respective electron channels (Evans & Greer, 2004), are then retrieved and subtracted from the original measured electron fluxes.

A detailed discussion on which radiation belt populations the 0° and 90° telescopes measure has been presented in Appendix A in Rodger et al. (2010). In general, it shows that at middle and high latitudes the 0° telescopes measure particle fluxes that will be lost to the atmosphere, whereas the 90° telescopes detect precipitating particle fluxes and/or trapped particles in the radiation belts. This implies that in the frequent case of pitch angle anisotropy the 0° detector will underestimate, while the 90° detector will overestimate the flux of precipitating electrons (Nesse Tyssøy et al., 2016; Nesse Tyssøy et al., 2019). A more realistic estimate can be achieved by combining fluxes from both the 0° and 90° telescopes together with electron pitch angle distributions from theory of wave-particle interactions in the magnetosphere. We solve the Focker-Planck equation for particle diffusion (Kennel & Petschek, 1966; Theodoridis & Paolini, 1967) for a wide range of diffusion coefficients (The specific equations are also given in Nesse Tyssøy et al. (2016)). The solutions are then transformed to the satellite altitude and saved in a look-up table. When comparing the theoretical pitch angle distributions with the measured particle fluxes the procedure is as follows:

- Determine the pitch angles of center look directions of the 0° and 90° telescopes.
- Calculate the ratio between of the fluxes detected by the 0° and 90° detector.
- Calculate the ratio between the fluxes for the theoretical pitch angle distributions taking into account the look directions.
- Determine which of the theoretical pitch angle distributions best corresponds to the observed ratio.

Finally, the size of the loss cone, predicted based on the International Geomagnetic Reference Field (IGRF) model, are applied to estimate the precipitating fluxes. The loss cone flux estimate is done separately for each energy channel as the level of particle diffusion will vary with energy. A detail explanation of the method can be found in Nesse Tyssøy et al. (2016).

We use MEE precipitation estimates from a full solar cycle from 2004 to 2014. This includes the active years in the declining phase of cycle 23, the extreme minimum, and the moderate maximum of cycle 24. **Figure 1** illustrates the number of NOAA and MetOp satellites applied throughout the 11 years alongside the MLT coverage in the NH. Although, the combination of satellites has a near global coverage on a daily scale, it is not equally distributed in terms of MLT. In particular, the evening sector and midnight sector are poorly represented in the NH. The daily average of the fluxes is therefore first calculated for four separate MLT sectors, 0–6 MLT, 6–12 MLT, 12–18 MLT, and 18–24 MLT over the CGM latitude band 55°–70°. Thereafter, a daily MEE flux is achieved as the average of the four MLT regions to ensure that the MEE flux is weighted equally in respect to MLT. **Figure 2** shows the resulting daily integral fluxes for the energies >43 keV (blue line), >114 keV (red line), and >292 keV (black line) over the full solar cycle. The values are given as the logarithm of the flux value, illustrating that the flux of the high energy tail >292 keV are typically two order of magnitude less than the >43 keV fluxes.

2.2 The Auroral Electrojet Index

The AE-index is designed by Davis and Sugiura (1966) to monitor the electrojet activity. The link to substorm activity was assumed from the very beginning as the substorm current system lies in the ionosphere. However, its deficiency with respect to coarse geographic latitude and longitude coverage was quickly pointed out. The observations, limited to a geomagnetic latitude band of 60°–70°N, could not always detect the dynamic auroral oval, both expanding equatorward and contracting poleward of the 12–13 stations. Short-term and localized events in the midnight sector, such as substorms, can easily be missed by the coarse network of stations. Besides substorms, pseudo-breakups, steady magnetospheric convection events, sawtooth injections, poleward boundary intensifications, or a mixture of these modes have been recognized in the AE data (McPherron, 2015). To overcome some of these challenges, regional electrojet-indices have been created (Tanskanen, 2009), and multiple regional magnetometer chains have been combined to compile globally denser network of stations (Gjerloev, 2012). Analysis have been performed to identify individual substorms. However, no generally accepted

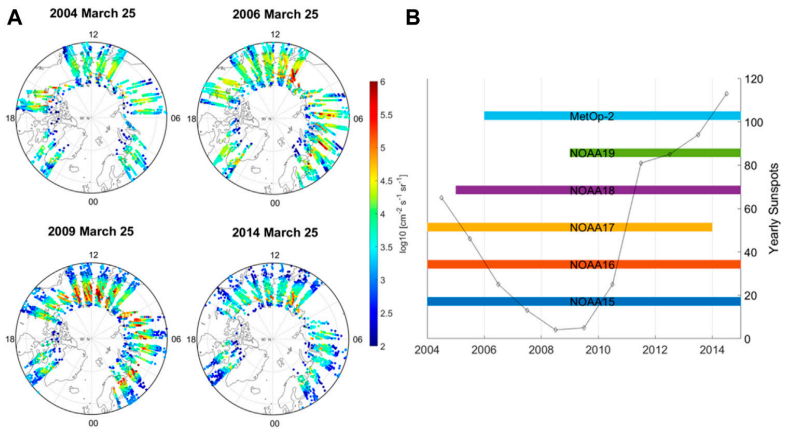

FIGURE 1 | (A): The POES and MetOp satellite MLT coverage over a full day during March 25th in 2004, 2006, 2009 and 2014. **(B)**: The POES and MetOp satellite coverage over a full solar cycle from 2004 to 2014.

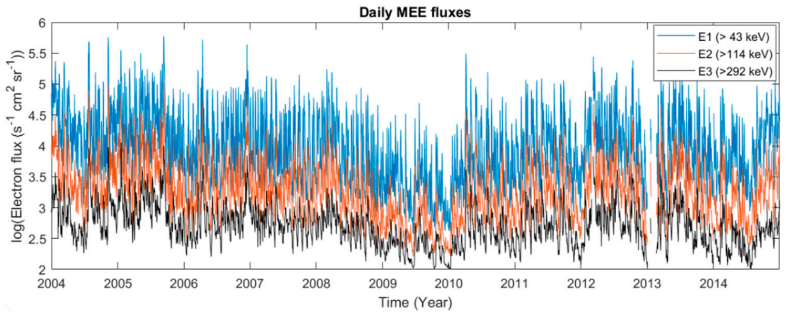

FIGURE 2 | Daily MEE of >43 keV (blue line), >114 keV (red line), and >292 keV (black line) from 2004 to 2014. The fluxes are averaged over all MLT and the CGM latitude band 55°–70°N.

method exists to identify substorm events from auroral electrojet indices, and different sets of criteria are used in different studies (e.g., Tanskanen et al., 2002; Newell & Gjerloev, 2011).

Figure 3 shows the daily averaged AE index alongside the daily number of substorms identified by Newell and Gjerloev (2011) from 2004 to 2014. The Pearson correlation coefficient, r, between the two datasets over the entire solar cycle is 0.89, giving $r^2 = 0.79$. It should, however, be emphasized that using the AE index on a daily scale makes identification of substorm/non-substorm modes problematic in particular for long active periods. Therefore, **Figure 3** shows a potential (but not proven) link between the daily averaged AE index and substorms.

We note that the daily AE index has a pronounced seasonal bias where the AU and AL indices maximize during summer and equinoctial months, respectively (Ahn et al., 2000). The equinox bias is due to the seasonal bias of solar wind driving which also applies to MEE. While the summer maxima, clearly evident in **Figure 3**, is due to increased background ionization from UV. This implies that the relation between the AE index and other parameters such as the number of substorms or MEE flux will vary with season. It also means that if AE, based on observations only from NH, is to be used as a global proxy for both hemispheres the seasonal bias needs to be addressed. In the MEE_{proxy} developed in this study, we remove the seasonal trend by subtracting the minimum daily AE value found in a moving window of ±14 days from the daily resolved AE index.

3 RESULTS

The daily AE index vary by three orders of magnitude over the 11 years. The daily fluxes of >43, >114, and >292 keV loss cone

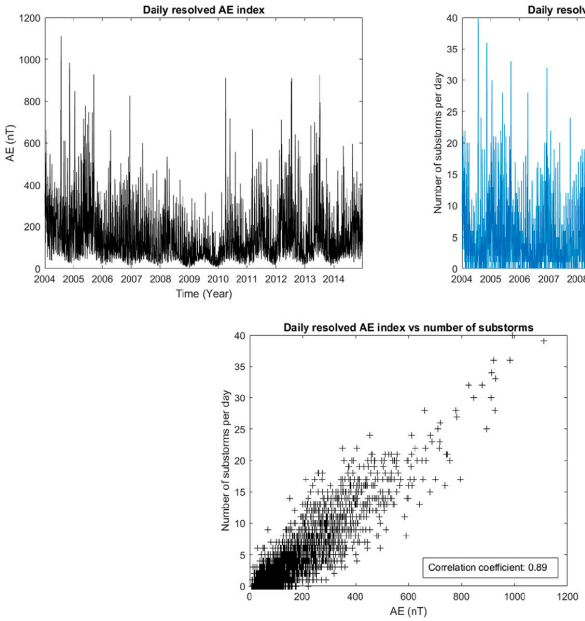

FIGURE 3 | Upper left plot: Daily resolved AE index (black line). **Upper right plot:** The number of substorms per day (blue line) based on Newell and Gjerloev (2011). **Upper right plot:** Scatter plot of the number of substorms per day and the daily resolve AE index. All panels include the period from 2004 to 2014.

fluxes over the 55°–70° CGM latitude band varies by five, four, and three orders of magnitude over the same period, respectively. **Figure 4** shows the scatter plots of a linear fit for 1) the linear value of the daily AE index and linear value of the daily >43 keV fluxes (Linear-Linear), 2) the linear value of the daily AE index and logarithmic value of the daily >43 keV fluxes (Linear-Logarithmic), and 3) the logarithmic value of the daily AE index and logarithmic value of the daily >43 keV fluxes (Logarithmic-Logarithmic). Despite a fairly good correlation of 0.83, the predictability of the Linear-Linear comparison is quite poor for low flux values. The Linear-Logarithmic and Logarithmic-Logarithmic comparison ensure equal weighting of errors associated to high and low flux values. Nevertheless, despite a high correlation coefficient of 0.81, the Linear-Logarithmic comparison systematically overestimates the high flux values and underestimate the low flux values. The Logarithmic-Logarithmic fit shows a clear linear dependence with the highest correlation coefficient of 0.88. As such, it is evident both in the correlation coefficients, and the scatter plots that using both the logarithmic values of the AE and the fluxes, ensures the strongest correspondence.

Table 1 lists the Pearson correlation coefficient between the daily resolved logarithmic value of the AE index and the logarithmic value of >43, >114, and >292 keV The square value of the correlation coefficients of 0.88 and 0.73 implies that the AE regression models fit with 77% and 53% of the variability of the >43 keV and >114 keV fluxes, respectively. The correlation coefficient decreases with energy, where a value of 0.47 implies that the AE regression model can only fit 22% of the variability of the >292 keV fluxes. This might reflect that a larger fraction of the >43 keV and >114 keV electron fluxes are directly injected during the substorm activity, while relatively fewer electrons >292 keV are part of the initial seed population. **Table 1** also shows that the AE index is best correlated with >43 keV and >114 keV electron fluxes in the post-midnight MLT sector which supports the link to substorm nightside injection and the subsequent eastward electron drift around the Earth and westward electrojet enhancements. The MLT bias is, however, not as prominent for >292 keV electron fluxes.

Figure 5A shows the Pearson correlation coefficients between the logarithmic value of the AE index 0–8 days prior to the logarithmic value of the observed MEE fluxes. The highest correlation is found on day zero, zero, and two for >43, >114, and >292 keV fluxes, respectively. The increasing offset as a function of energy substantiates that time is a prerequisite for the MEE high energy tail. The broad correlation peak and gradual decay further suggest that the MEE fluxes are influenced by the geomagnetic activity level of several days. **Figure 5B** shows the correlation between the logarithmic value of the AE index accumulated over consecutive longer periods prior to the logarithmic value of the observed MEE fluxes. The correlation coefficients between the accumulated AE index and the >43 keV fluxes peaks at 0.88 when both the zero and first preceding day are taken into account, which based on r-squared corresponds to

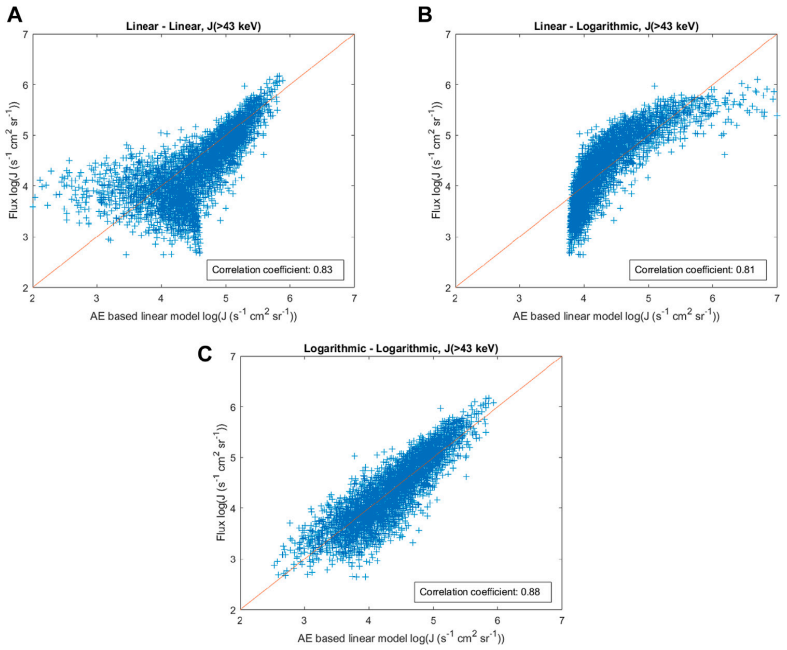

FIGURE 4 | Scatter plots and a linear fit of **(A)** the linear value of the daily AE index and linear value of the daily >43 keV fluxes (Linear-Linear), **(B)** the linear value of the daily AE index and logarithmic value of the daily >43 keV fluxes (Linear-Logarithmic), and **(C)** the logarithmic value of the daily AE index and logarithmic value of the daily >43 keV fluxes (Logarithmic-Logarithmic).

TABLE 1 | The Pearson correlation coefficient between daily resolved AE index and the logarithmic value of >43 > 114, and >292 keV loss cone fluxes over the 55°–70° CGM latitude band for the years 2004–2014.

Correlation coefficient between the AE index and MEE fluxes					
Energy	**0–6 MLT**	**6–12 MLT**	**12–18 MLT**	**18–24 MLT**	**All MLT**
>43 keV	0.86	0.86	0.85	0.74	0.88
>114 keV	0.73	0.75	0.73	0.65	0.73
>292 keV	0.48	0.46	0.45	0.47	0.47

approximately 77% of the flux variability. The correlation coefficient of the AE index for the >114 keV fluxes reaches about 0.83 when 3–4 days are accumulated, increasing the predictive capability of AE index from about 53% to 69%. The correlation coefficient between the accumulated AE index and the >292 keV fluxes increases rapidly the first few days and as many as seven preceding days are required for it to reach its peak of 0.81. Now, the predictive capability of the AE index has increased from about 22% to 66%.

Based on the correlation coefficients shown in **Figure 5A** is unlikely that each of the preceding days are equally important as assumed in this simple model shown in **Figure 5B**. As time evolves the seed population injected during a specific substorm is not only accelerated, but it is likely to be lost to the atmosphere or to the magnetopause. A more realistic model, where the AE index is weighted in respect to lifetimes of the particle population, could increase the predictive capability of the AE index even more. We assume the following weighting of geomagnetic activity:

$$MEE_{proxy} = \sum_{i=0}^{10} AE_i \cdot e^{\left(\frac{-i}{\tau}\right)} \quad (1)$$

where i refers to the preceding days and τ is the assumed lifetime. Due to the broad peak found in **Figure 5** for the >292 keV fluxes, the equation includes ten offset days. Furthermore, **Figure 3** shows a clear seasonal trend in the daily AE index which could impact the correlation with the MEE fluxes. As described in **Section 2.2**, we remove the seasonal trend in the AE index by subtracting the minimum daily AE value found in a moving window of ±14 days from all AE values. Now, the maximum correlation coefficients increases to 0.91, 0.89, and 0.84, using the optimized lifetime, τ, of one, three, and 9 days for >43 keV, > 114 keV, and >292 keV, respectively.

For the >43 keV fluxes a correlation coefficient of 0.91 is a small improvement from the 0.88 found in **Figure 5**. In addition, to better model low and high extremes, we fit two separate linear equations based on the logarithmic value of the MEE_{proxy}. The optimized separating boundary and the associated model equations are achieved by stepwise moving the limit over the

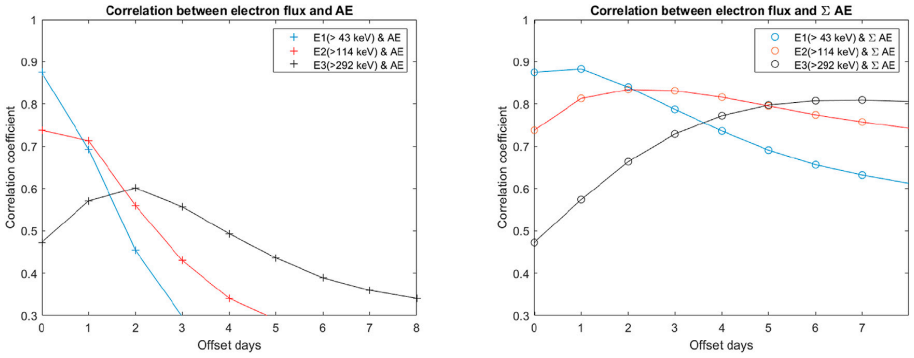

FIGURE 5 | The Pearson correlation coefficients between the logarithmic value of the electron fluxes >43 keV (blue line), >114 keV (red line), and >292 keV (black line) and the logarithmic value of the AE index (left plot) and the logarithmic value of the accumulated AE values (right plot).

TABLE 2 | The MEE_{proxy} models for two separate MEE_{proxy} intervals. The models give the logarithmic value of >43, >114, and >292 keV loss cone fluxes over the 55°–70° CGM latitude band.

The MEE_{proxy} model			
Energy	**MEE_{proxy}**	**Linear Model 1**	**Linear Model 2**
>43 keV	$\sum_{i=0}^{10} AE_i \cdot e^{(\frac{-i}{7})}$	$MEE_{proxy} < 66nT$: $a \cdot log(MEE_{proxy}) + b$, a = 0.6481, b = 2.634	$MEE_{proxy} \geq 66nT$: $a \cdot log(MEE_{proxy}) + b$, a = 1.733, b = 0.6631
>114 keV	$\sum_{i=0}^{10} AE_i \cdot e^{(\frac{-i}{7})}$	$MEE_{proxy} < 224nT$: $a \cdot log(MEE_{proxy}) + b$, a = 0.9654, b = 0.9843	$MEE_{proxy} \geq 224nT$: $a \cdot log(MEE_{proxy}) + b$, a = 1.752, b = -0.8791
>292 keV	$\sum_{i=0}^{10} AE_i \cdot e^{(\frac{-i}{7})}$	$MEE_{proxy} < 984nT$: $a \cdot log(MEE_{proxy}) + b$, a = 0.7717, b = 0.6536	$MEE_{proxy} \geq 984nT$: $a \cdot log(MEE_{proxy}) + b$, a = 1.414, b = -0.9869

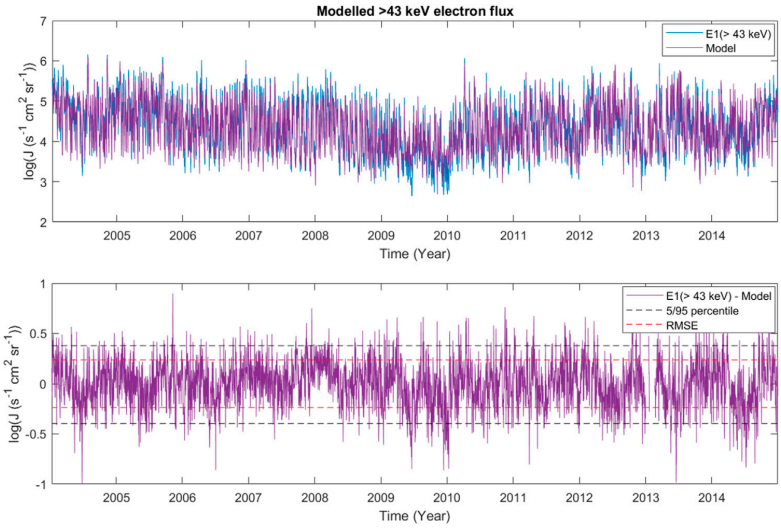

FIGURE 6 | The upper panel shows the observed (blue) and modelled (purple) daily resolved fluxes >43 keV in the period from 2004 to 2014. The lower panel shows the difference between the observed and modelled fluxes.

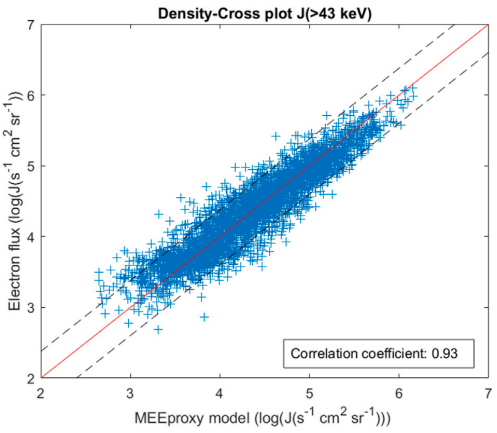

FIGURE 7 | Scatter plot of a linear fit of the logarithmic value of the optimized MEE_{proxy} and logarithmic value of the daily >43 keV fluxes. The black, dashed lines show the 95 and 5 percentile of the model errors.

entire MEE_{proxy} interval while performing two independent linear regression fits for the fluxes associated with the MEE_{proxy} values below and above the limit. The boundary giving the highest correlation coefficient and smallest RMSE for the two model fits combined are selected. An overview of the AE based MEE_{proxy}, including the mathematical expressions, lifetime τ, and linear equations are given in **Table 2** (Note that the limits are based on the MEE_{proxy} and not the daily AE values.) These simple measures increase the correlation coefficients to 0.93, 0.90, and 0.85 for >43 keV, > 114 keV, and >292 keV, respectively. This implies that about 86%, 81% and 72% of the daily flux variability, considering all MLTs and the full solar cycle, can be accounted for by the MEE_{proxy} models.

The upper panel in **Figure 6** shows the resulting linear fits to the AE-based MEE_{proxy} for >43 keV electron fluxes. The model captures the day-to-day fluctuations. The lower panel shows the differences between the observed and modelled fluxes. Similarly to the flux, the error are given as log [J ($s^{-1}cm^2sr^{-1}$)], which implies that values larger than one would correspond to one order of magnitude difference. The 5/95 percentile black, dashed lines demonstrate that the typical error is less than 0.4 log [J ($s^{-1}cm^2sr^{-1}$)], corresponding to the value $10^{0.40} \sim 2.5$. This means that for 90% of the days the model predicts fluxes that deviates from the observed fluxes by less than a factor of 2.5. The largest error found is 0.99 which correspond to a factor of 9.8. Hence, all values are within one order of magnitude of the observed fluxes. We note, however, specific periods in time where the model appears to have a bias. In the declining phase the model underestimates the flux level, while the opposite occurs for the extreme solar minimum year of 2009. There also appear to be a seasonal bias where the model overestimate/underestimate the flux values during summer/winter. **Figure 7** shows the scatter plot of the MEE_{proxy} model vs the observed >43 keV electron flux. It illustrates that the largest errors are found during low to moderate activity. Compared to **Figure 4** the improvement using the MEE_{proxy} model on a detrended AE index is readily evident.

Figure 8 shows the resulting linear fits to the AE-based MEE_{proxy} for >114 keV electron fluxes. The accuracy and weaknesses of the modelled >114 keV fluxes are similar to the modelled >43 keV fluxes as shown in **Figure 8**. However, **Figure 9** shows a tendency of the MEE_{proxy} model to overestimate the fluxes during high activity. **Figure 10** and **Figure 11** confirm a similar trend for the modelled >292 keV fluxes. All correlation coefficients, including the MLT dependence are listed in **Table 3**.

4 DISCUSSION AND CONCLUSION

There is increasing evidence that substorms are key in driving MEE precipitation (Beharrell et al., 2015; Partamies et al., 2021). Nevertheless, the substorms remain partly unresolved in the existing proxies when considering the MEE precipitation (van de Kamp et al., 2016). In this study, we have explored the prediction capability of AE in regard to MEE precipitation on a daily scale over a full solar cycle. The potential link between the AE index, substorms, and MEE precipitation will be discussed, alongside the progressive time delay between the geomagnetic activity and the MEE precipitation.

The initial correlation study, summarized in **Figure 5**, reveals a high coherence between the daily AE index with zero lag and >43 keV precipitating electron fluxes. Similarly, **Figure 3** suggests a strong coherence with the daily AE index and the daily number of substorms. The magnetotail dipolarization during substorms will directly inject source and seed particles in this energy range, some of which will precipitate into the atmosphere. It is therefore a realistic physical link between the AE intensity and >43 keV fluxes, despite the fact that the >43 keV fluxes deposit their energy below 100 km and do not directly contribute to the intensity of the electrojets. The strong correlation between the AE index and >43 keV fluxes is in agreement with recent studies of the trapped radiation belt electrons. Based on an extensive database of 16 years of corrected MEE flux observations (40–400 keV) from the Research with Adaptive Particle Imaging Detector (RAPID)/Imaging Electron Spectrometer (IES) instrument on board the Cluster mission, Smirnov et al. (2019) reveal that the variability of the outer belt electrons (L-shell 4–6) exhibits a pattern very close to the AE index. Furthermore, Katsavrias et al. (2021) confirm, based on 9 years of electron measurements from GOES-13, 14 and 15, that the trapped electron fluxes at energies in the interval 10–100 keV are well correlated with the AE index consistent with substorm injected source particles.

In the case of the high energy tail of the MEE precipitation, **Figure 5** suggests that only 22% of the >292 keV flux variability are described by the daily AE variability. Ødegaard et al. (2017) shows that these higher energy electrons typically peak 1–2 days after the onset of a geomagnetic storm. The progressive time delays of relativistic electrons has also been identified by e.g., Boynton et al. (2016) and Mourenas et al. (2019). The delay implies that it takes time to accelerate the injected seed electrons

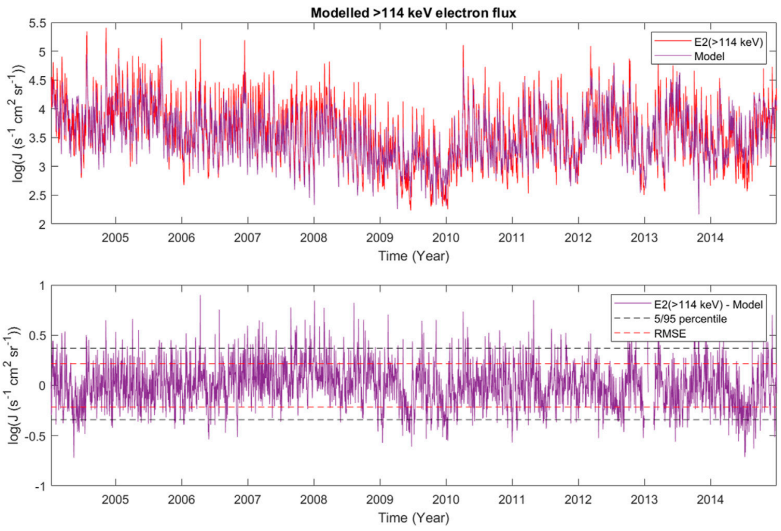

FIGURE 8 | The upper panel shows the observed (red) and modelled (purple) daily resolved fluxes >114 keV in the period from 2004 to 2014. The lower panel shows the difference between the observed and modelled fluxes.

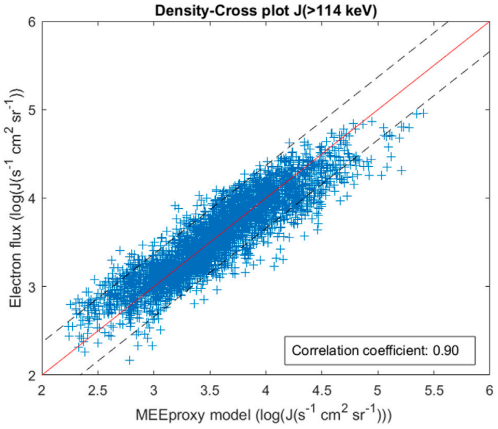

FIGURE 9 | Scatter plot of a linear fit of the logarithmic value of the optimized MEE_{proxy} and logarithmic value of the daily >114 keV fluxes. The black, dashed lines show the 95 and 5 percentile of the model errors.

into several 100 s keV. It will also require a continuous acceleration mechanism. This could be provided during repeated substorm activity, as the source particles will fuel VLF waves and the injected seed particles can be energized as they drift across the substorm induced electric field on the nightside. This means that the precipitating >292 keV fluxes are a product of both the ongoing activity, as well as the substorm activity during the previous days. This potential link is made viable by the simple accumulation of the AE values in **Figure 5B**. However, the identification of substorm/non-substorm modes might be problematic using the daily resolved AE index, in particular for long active geomagnetic periods. Moreover, VLF acceleration and scattering are not limited to substorm periods.

Katsavrias et al. (2021) also find a reduced correlation between 100–350 keV trapped electron flux and the AE index compared to the 10–100 keV electrons. These higher energies display, however, a strong dependence on the solar wind speed. They suggest that it implies that the acceleration and loss of the seed energies are not purely substorm driven but rather depend on convection driven by the fast solar wind and/or ULF driven inward diffusion. Smirnov et al. (2019) demonstrate a high positive correlation between the 40–400 keV radiation belt electrons and the AE index and solar wind dynamic pressure. Furthermore, Stepanov et al. (2021) confirm the role of solar wind speed as one of the most important predictors for transporting electron fluxes from the plasmasheet to the radiation belt region. Similarly, Ødegaard et al. (2017) show how the >292 keV flux variability depends on the Akasufos's coupling function. Boynton et al. (2016) developed forecast models for MEE and highly relativistic electrons using the coupling function proposed by (Boynton et al., 2011) and the Dst index. The latter confirms the solar wind dependence while simultaneously accounting for the direction of the Northward interplanetary field direction. Neither the solar wind dependence, nor the coupling function dependence does, however, exclude substorms and the associated VLF wave generation as the working mechanism. In

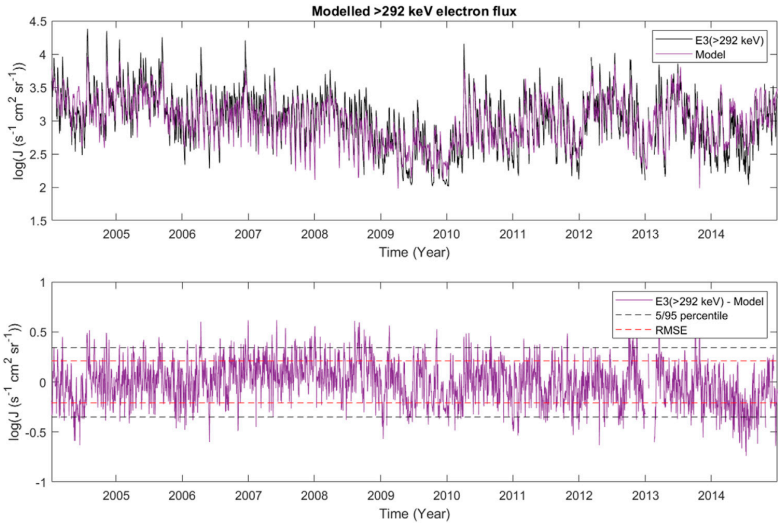

FIGURE 10 | The upper panel shows the observed (black) and modelled (purple) daily resolved fluxes >292 keV in the period from 2004 to 2014. The lower panel shows the difference between the observed and modelled fluxes.

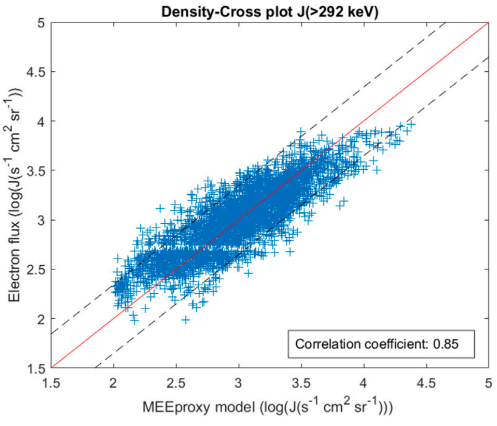

FIGURE 11 | Scatter plot of a linear fit of the logarithmic value of the optimized MEE_{proxy} and logarithmic value of the daily >292 keV fluxes. The black, dashed lines show the 95 and 5 percentile of the model errors.

fact, Miyoshi et al. (2013) find that High Speed Solar Wind Streams (HSSWS) alone is not sufficient to cause relativistic electron flux enhancement in the outer radiation belt, but strongly depend on IMF-Bz. They state that this would not be the case if radial transport via ULF waves is the primary mechanism. Miyoshi and Kataoka (2008) suggested that the IMF-Bz dependence could be attributed to substorm occurrence during HSSWS events where the electrons are accelerated via VLF waves. This is in line with the relativistic electron flux enhancements found during intervals of prolonged substorm activity operating on a timescale of the order of days (Bühler & Desorgher, 2002; Meredith et al., 2003).

The lifetimes applied in the MEE_{proxy} are impacted by the lifespan of the MEE particles in the outer radiation belt. The lifespan depends on the energy, radial distance from Earth, and the level of geomagnetic activity. The lifetimes for 100 keV electrons at a radial distance of about four are approximately 3.6 days and 13 h for quiet and active geomagnetic conditions, respectively, and are increasing rapidly with energy to about 131 and 17 days for 1 MeV electrons (Orlova et al., 2016). The expected lifetime can, however, be rapidly reduced in the case of magnetopause shadowing where trapped particles over several radial distances are lost to the magnetopause. This is a consequence of a sudden dynamic pressure increase in the solar wind, alongside convection driven outward radial transport (Turner et al., 2012). Applying a fixed lifetime as suggested in the MEE_{proxy} is therefore unrealistic. The optimized lifetime applied in the MEE_{proxy} is thus only the empirical average based on the applied data. It does, however, demonstrate the potential of an AE based MEE_{proxy}, where the precipitation fluxes are an accumulated effect of both the current and previous geomagnetic activity.

This study reveals the high predictive capabilities of the AE index for MEE precipitation, and how to account for the delayed response of the high energy tail (> 300 keV). Hence, it offers a potential improvement to the current MEE parameterization included in CMIP6 recommendation (Matthes et al., 2017). Nesse Tyssøy et al. (2019) compares the loss cone estimate to

TABLE 3 | The Pearson correlation coefficient between daily resolved AE based MEE_{proxy} and the logarithmic value of >43, >114, and >292 keV loss cone fluxes over the 55°–70° CGM latitude band for the years 2004–2014.

Correlation coefficient between the AE based MEE proxy and MEE fluxes					
Energy	**0–6 MLT**	**6–12 MLT**	**12–18 MLT**	**18–24 MLT**	**All MLT**
>43 keV	0.91	0.92	0.91	0.84	0.93
>114 keV	0.87	0.89	0.91	0.89	0.90
>292 keV	0.84	0.84	0.85	0.85	0.85

the CMIP recommendation and shows an overall underestimation of basic flux strength about one order of magnitude arises from utilizing 0° detector electron fluxes. As this is the same data used to develop the MEE_{proxy} model it is likely that the same assessment will apply if compared to the CMIP recommendation. Furthermore, Nesse Tyssøy et al. (2019) showed that the CMIP recommendation generally captured the initial phase of the storm fluxes, but fell short in respect to reproducing elevated flux levels during the recovery phase of CIR-driven storms. As such, the energy dependent lifetimes applied in the MEE_{proxy}, taking into account the accumulated geomagnetic activity, is likely to avoid this pitfall.

However, for AE to be used as a proxy for MEE precipitation in a more advanced MEE precipitation model, the seasonal bias needs further examination as it could be a source of unequal distribution between the two hemispheres. In addition, **Figures 6**, **8**, **10** show a potential solar cycle bias of a general underestimation in the declining phase. To which extent this is due to the dynamical expansion of the auroral oval and the equatorward shift of the electrojets, where the AE-stations cannot reliably monitor their intensity, needs to be explored. The small number of magnetometer stations and their uneven spatial distribution implies that small perturbations (e.g., isolated substorms and pseudo-breakups) can be undetected and large deflections underestimated if they are constrained in longitude or are located at latitudes poleward or equatorward of the AE station network (Gjerloev et al., 2004). Similarly, the MEE precipitation region does not cover a fixed latitude band, and its dependence with geomagnetic activity is explored in a parallel study. Alternatively, the solar cycle bias might reflect the type of solar wind driver responsible for the geomagnetic disturbances as Corotating Interaction Region (CIR)/ High Speed Solar Wind Streams (HSSWS) and Coronal Mass Ejection (CME) driven geomagnetic storms dominate different phases of the solar cycle. For example, the lifetime applied in the MEE_{proxy} can vary in weak but long lasting CIR/HSSWS compared to a short but powerful CME event.

In summary, this study demonstrates that simple AE based MEE-proxies have the capability of explaining at 72–86% of the detected MEE precipitation variance on a daily scale. The model shows, however, caveats in respect to the solar cycle and extreme events that summon further investigations. Nevertheless, 90% of the modelled flux values deviate less than a factor of 2.5 from the observed NOAA/ POES MEPED fluxes throughout a full solar cycle. By evaluating the different energy channels, > 43, >114, and >292 keV, independently, the model enables a realistic description of the time dependent energy spectrum. This finding will form the base of a new MEE model to be used for future studies of the energetic electron precipitation impact on the atmosphere.

DATA AVAILABILITY STATEMENT

Publicly available datasets were analyzed in this study. This data can be found here: https://www.ngdc.noaa.gov/stp/satellite/poes/dataaccess.html http://wdc.kugi.kyoto-u.ac.jp/wdc/Sec3.html https://supermag.jhuapl.edu/substorms/

AUTHOR CONTRIBUTIONS

HNT conceived idea of this paper, in charge of the analysis, and writing as lead author. NP contributed to the idea of this paper and editing of the manuscript. EMB is responsible for constructing the MLT dependent daily resolved electron flux and editing of the manuscript. CS-J contributed to editing of the manuscript. JAS contributed to editing of the manuscript.

FUNDING

The study is supported by the Norwegian Research Council (NRC) under contract 223252, 302040 and 287427. HNT further acknowledge the Young CAS (Centre for Advanced Studies) fellow program.

ACKNOWLEDGMENTS

The NOAA/POES data used in this study are available from the National Oceanic and Atmospheric Administration (https://www.ngdc.noaa.gov/stp/satellite/poes/dataaccess.html). The AE index used in this paper was provided by the WDC for Geomagnetism, Kyoto (http://wdc.kugi.kyoto-u.ac.jp/wdc/Sec3.html). We also acknowledge the substorm timing list identified by the Newell and Gjerloev technique (Newell and Gjerloev, 2011), the SMU and SML indices (Newell and Gjerloev, 2011); and the SuperMAG collaboration (Gjerloev, 2012) (https://supermag.jhuapl.edu/substorms/).

REFERENCES

Ahn, B.-H., Kroehl, H. W., Kamide, Y., and Kihn, E. A. (2000). Seasonal and Solar Cycle Variations of the Auroral Electrojet Indices. *J. Atmos. Solar-Terrestrial Phys.* 62 (14), 1301–1310. doi:10.1016/s1364-6826(00)00073-0

Andersson, M. E., Verronen, P. T., Wang, S., Rodger, C. J., Clilverd, M. A., and Carson, B. R. (2012). Precipitating Radiation belt Electrons and Enhancements of Mesospheric Hydroxyl during 2004-2009. *J. Geophys. Res.* 117 (D9). doi:10.1029/2011JD017246

Beharrell, M. J., Honary, F., Rodger, C. J., and Clilverd, M. A. (2015). Substorm-induced Energetic Electron Precipitation: Morphology and Prediction. *J. Geophys. Res. Space Phys.* 120 (4), 2993–3008. doi:10.1002/2014ja020632

Borovsky, J. E., and Yakymenko, K. (2017). Substorm Occurrence Rates, Substorm Recurrence Times, and Solar Wind Structure. *J. Geophys. Res. Space Phys.* 122 (3), 2973–2998. doi:10.1002/2016ja023625

Boynton, R. J., Balikhin, M. A., Billings, S. A., Wei, H. L., and Ganushkina, N. (2011). Using the Narmax Ols-Err Algorithm to Obtain the Most Influential Coupling Functions that Affect the Evolution of the Magnetosphere. *J. Geophys. Res. Space Phys.* 116 (A5). doi:10.1029/2010ja015505

Boynton, R. J., Balikhin, M. A., Sibeck, D. G., Walker, S. N., Billings, S. A., and Ganushkina, N. (2016). Electron Flux Models for Different Energies at Geostationary Orbit. *Space Weather* 14 (10), 846–860. doi:10.1002/2016sw001506

Bühler, P., and Desorgher, L. (2002). Relativistic Electron Enhancements, Magnetic Storms, and Substorm Activity. *J. Atmos. Solar-Terrestrial Phys.* 64 (5), 593–599. doi:10.1016/s1364-6826(02)00017-2

Clilverd, M. A., Rodger, C. J., van de Kamp, M., and Verronen, P. T. (2020). Electron Precipitation from the Outer Radiation belt during the St. Patrick's Day Storm 2015: Observations, Modeling, and Validation. *J. Geophys. Res. Space Phys.* 125 (2), e2019JA027725. doi:10.1029/2019ja027725

Dai, L., Wygant, J. R., Cattell, C. A., Thaller, S., Kersten, K., Breneman, A., et al. (2014). Evidence for Injection of Relativistic Electrons into the Earth's Outer Radiation belt via Intense Substorm Electric fields. *Geophys. Res. Lett.* 41 (4), 1133–1141. doi:10.1002/2014gl059228

Davis, T. N., and Sugiura, M. (1966). Auroral Electrojet Activity indexAEand its Universal Time Variations. *J. Geophys. Res.* 71 (3), 785–801. doi:10.1029/jz071i003p00785

Evans, D. S., and Greer, M. S. (2004). *Polar Orbiting Environmental Satellite Space Environment Monitor - 2: Instrument Descriptions and Archive Data Documentation*. Boulder, Colorado: NOAA Technical Memorandum, 93. version 1.4

Gjerloev, J. W., Hoffman, R. A., Friel, M. M., Frank, L. A., and Sigwarth, J. B. (2004). Substorm Behavior of the Auroral Electrojet Indices. *Ann. Geophys.* 22 (6), 2135–2149. doi:10.5194/angeo-22-2135-2004

Gjerloev, J. W. (2012). The Supermag Data Processing Technique. *J. Geophys. Res. Space Phys.* 117 (A9), 9213. doi:10.1029/2012ja017683

Jaynes, A. N., Baker, D. N., Singer, H. J., Rodriguez, J. V., Loto'aniu, T. M., Ali, A. F., et al. (2015). Source and Seed Populations for Relativistic Electrons: Their Roles in Radiation belt Changes. *J. Geophys. Res. Space Phys.* 120 (9), 7240–7254. doi:10.1002/2015ja021234

Katsavrias, C., Aminalragia–Giamini, S., Papadimitriou, C., Sandberg, I., and Jiggens, P. (2021). Daglis, I.,and Evans, HOn the Interplanetary Parameter Schemes Which Drive the Variability of the Source/seed Electron Population at Geo. Journal of Geophysical Research. *Space Phys.* 126 (6), e2020JA028939. doi:10.1029/2020ja028939

Kauristie, K., Morschhauser, A., Olsen, N., Finlay, C. C., McPherron, R. L., Gjerloev, J. W., et al. (2017). On the Usage of Geomagnetic Indices for Data Selection in Internal Field Modelling. *Space Sci. Rev.* 206, 61–90. doi:10.1007/s11214-016-0301-0

Kennel, C. F., and Petschek, H. E. (1966). Limit on Stably Trapped Particle Fluxes. *J. Geophys. Res. (1896-1977)* 71 (1), 1–28. doi:10.1029/jz071i001p00001

Li, L. Y., Cao, J. B., Zhou, G. C., and Li, X. (2009). Statistical Roles of Storms and Substorms in Changing the Entire Outer Zone Relativistic Electron Population. *J. Geophys. Res. Space Phys.* 114 (A12). doi:10.1029/2009ja014333

Maliniemi, V., Asikainen, T., and Mursula, K. (2016). Effect of Geomagnetic Activity on the Northern Annular Mode: Qbo Dependence and the holton-tan Relationship. *J. Geophys. Res. Atmospheres* 121 (17), 10043–10055. doi:10.1002/2015jd024460

Matthes, K., Funke, B., Andersson, M. E., Barnard, L., Beer, J., Charbonneau, P., et al. (2017). Solar Forcing for CMIP6 (v3.2). *Geosci. Model. Dev.* 10, 2247–2302. doi:10.5194/gmd-10-2247-2017

McPherron, R. L. (2015). "Earth's Magnetotail," in *Magnetotails in the Solar System* (American Geophysical Union), 61–84. doi:10.1002/9781118842324.ch4

Meredith, N. P., Cain, M., Horne, R. B., Thorne, R. M., Summers, D., and Anderson, R. R. (2003). Evidence for Chorus-Driven Electron Acceleration to Relativistic Energies from a Survey of Geomagnetically Disturbed Periods. *J. Geophys. Res. Space Phys.* 108 (A6). doi:10.1029/2002ja009764

Mironova, I. A., Artamonov, A. A., Bazilevskaya, G. A., Rozanov, E. V., Kovaltsov, G. A., Makhmutov, V. S., et al. (2019). Ionization of the Polar Atmosphere by Energetic Electron Precipitation Retrieved from Balloon Measurements. *Geophys. Res. Lett.* 46 (2), 990–996. doi:10.1029/2018gl079421

Miyoshi, Y., and Kataoka, R. (2008). Flux Enhancement of the Outer Radiation belt Electrons after the Arrival of Stream Interaction Regions. *J. Geophys. Res. Space Phys.* 113 (A3). doi:10.1029/2007ja012506

Miyoshi, Y., Kataoka, R., Kasahara, Y., Kumamoto, A., Nagai, T., and Thomsen, M. F. (2013). High-speed Solar Wind with Southward Interplanetary Magnetic Field Causes Relativistic Electron Flux Enhancement of the Outer Radiation belt via Enhanced Condition of Whistler Waves. *Geophys. Res. Lett.* 40 (17), 4520–4525. doi:10.1002/grl.50916

Mourenas, D., Artemyev, A. V., and Zhang, X. J. (2019). Impact of Significant Time-Integrated Geomagnetic Activity on 2-MeV Electron Flux. *J. Geophys. Res. Space Phys.* 124 (6), 4445–4461. doi:10.1029/2019ja026659

Nesse Tyssøy, H., Haderlein, A., Sandanger, M. I., and Stadsnes, J. (2019). Intercomparison of the POES/MEPED Loss Cone Electron Fluxes with the CMIP6 Parametrization. *J. Geophys. Res. Space Phys.* 124, 628–642. doi:10.1029/2018JA025745

Nesse Tyssøy, H., Sandanger, M. I., Ødegaard, L.-K. G., Stadsnes, J., Aasnes, A., and Zawedde, A. E. (2016). Energetic Electron Precipitation into the Middle Atmosphere—Constructing the Loss Cone Fluxes from Meped Poes. *J. Geophys. Res. Space Phys.* 121 (6), 5693–5707. doi:10.1029/2004JA010485

Newell, P. T., and Gjerloev, J. W. (2011). Evaluation of SuperMAG Auroral Electrojet Indices as Indicators of Substorms and Auroral Power. *J. Geophys. Res.* 116 (A15). doi:10.1029/2011JA016779

Ødegaard, L.-K. G., Tyssøy, H. N., Sandanger, M. I. J., Stadsnes, J., and Søraas, F. (2016). Space Weather Impact on the Degradation of Noaa Poes Meped Proton Detectors. *J. Space Weather Space Clim.* 6, A26. doi:10.1051/swsc/2016020

Ødegaard, L. K. G., Tyssøy, H. N., Søraas, F., Stadsnes, J., and Sandanger, M. I. (2017). Energetic Electron Precipitation in Weak to Moderate Corotating Interaction Region-driven Storms. *J. Geophys. Res. Space Phys.* 122 (3), 2900–2921. doi:10.1002/2016ja023096

Orlova, K., Shprits, Y., and Spasojevic, M. (2016). New Global Loss Model of Energetic and Relativistic Electrons Based on Van allen Probes Measurements. *J. Geophys. Res. Space Phys.* 121 (2), 1308–1314. doi:10.1002/2015ja021878

Partamies, N., Tesema, F., Bland, E., Heino, E., Nesse Tyssøy, H., and Kallelid, E. (2021). Electron Precipitation Characteristics during Isolated, Compound, and Multi-Night Substorm Events. *Ann. Geophys.* 39 (1), 69–83. doi:10.5194/angeo-39-69-2021

Pettit, J. M., Randall, C. E., Peck, E. D., Marsh, D. R., Kamp, M., Fang, X., et al. (2019). Atmospheric Effects of >30-keV Energetic Electron Precipitation in the Southern Hemisphere Winter during 2003. *J. Geophys. Res. Space Phys.* 124 (10), 8138–8153. doi:10.1029/2019ja026868

Rodger, C., Carson, B., Cummer, S., Gamble, R., Clilverd, M., Green, J., et al. (2010). Contrasting the Efficiency of Radiation belt Losses Caused by Ducted and Nonducted Whistler-Mode Waves from Ground-Based Transmitters. *J. Geophys. Res. Space Phys.* 115 (A12). doi:10.1029/2010ja015880

Rodger, C. J., Cresswell-Moorcock, K., and Clilverd, M. A. (2016). Nature's Grand Experiment: Linkage between Magnetospheric Convection and the Radiation Belts. *J. Geophys. Res. Space Phys.* 121 (1), 171–189. doi:10.1002/2015ja021537

Sandanger, M. I., Ødegaard, L. K. G., Nesse Tyssøy, H., Stadsnes, J., Søraas, F., Oksavik, K., et al. (2015). In-flight Calibration of NOAA POES Proton Detectors-Derivation of the MEPED Correction Factors. *J. Geophys. Res. Space Phys.* 120 (11), 9578–9593. doi:10.1002/2015ja021388

Sætre, C., Stadsnes, J., Nesse, H., Aksnes, A., Petrinec, S. M., Barth, C. A., et al. (2004). Energetic Electron Precipitation and the No Abundance in the Upper

Atmosphere: A Direct Comparison during a Geomagnetic Storm. *J. Geophys. Res. Space Phys.* 109 (A9). doi:10.1029/2004JA010485

Seppälä, A., Clilverd, M. A., Beharrell, M. J., Rodger, C. J., Verronen, P. T., Andersson, M. E., et al. (2015). Substorm-induced Energetic Electron Precipitation: Impact on Atmospheric Chemistry. *Geophys. Res. Lett.* 42 (19), 8172–8176. doi:10.1002/2015gl065523

Seppälä, A., Lu, H., Clilverd, M. A., and Rodger, C. J. (2013). Geomagnetic Activity Signatures in Wintertime Stratosphere Wind, Temperature, and Wave Response. *J. Geophys. Res. Atmos.* 118 (5), 2169–2183. doi:10.1002/jgrd.50236

Sinnhuber, M., Friederich, F., Bender, S., and Burrows, J. P. (2016). The Response of Mesospheric NO to Geomagnetic Forcing in 2002-2012 as Seen by SCIAMACHY. *J. Geophys. Res. Space Phys.* 121, 3603–3620. doi:10.1002/2015JA022284

Smirnov, A. G., Kronberg, E. A., Latallerie, F., Daly, P. W., Aseev, N., Shprits, Y. Y., et al. (2019). Electron Intensity Measurements by the Cluster/RAPID/IES Instrument in Earth's Radiation Belts and Ring Current. *Space Weather* 17 (4), 553–566. doi:10.1029/2018sw001989

Stepanov, N. A., Sergeev, V. A., Sormakov, D. A., Andreeva, V. A., Dubyagin, S. V., and Ganushkina, N. (2021). Superthermal Proton and Electron Fluxes in the Plasma Sheet Transition Region and Their Dependence on Solar Wind Parameters. Journal of Geophysical Research. *Space Phys.* 126 (4), e2020JA028580. doi:10.1029/2020ja028580

Tanskanen, E. (2009). A Comprehensive High-Throughput Analysis of Substorms Observed by Image Magnetometer Network: Years 1993–2003 Examined. *J. Geophys. Res. Space Phys.* 114 (A5). doi:10.1029/2008ja013682

Tanskanen, E., Pulkkinen, T. I., Koskinen, H. E. J., and Slavin, J. A. (2002). Substorm Energy Budget during Low and High Solar Activity: 1997 and 1999 Compared. *J. Geophys. Res. Space Phys.* 107 (A6). doi:10.1029/2001ja900153

Theodoridis, G. C., and Paolini, F. R. (1967). Pitch Angle Diffusion of Relativistic Outer belt Electrons. *Ann. Geophys.*, 375–381.

Turner, D. L., Shprits, Y., Hartinger, M., and Angelopoulos, V. (2012). Explaining Sudden Losses of Outer Radiation belt Electrons during Geomagnetic Storms. *Nat. Phys* 8, 208–212. doi:10.1038/nphys2185

Turunen, E., Verronen, P. T., Seppälä, A., Rodger, C. J., Clilverd, M. A., and Tamminen, J. (2009). . . . Ulich, TImpact of Different Energies of Precipitating Particles on Nox Generation in the Middle and Upper Atmosphere during Geomagnetic Storms. *J. Atmos. Solar-Terrestrial Phys.* 71 (10), 1176–1189. doi:10.1016/j.jastp.2008.07.005

van de Kamp, M., Seppälä, A., Clilverd, M. A., Rodger, C. J., Verronen, P. T., and Whittaker, I. C. (2016). A Model Providing Long-Term Data Sets of Energetic Electron Precipitation during Geomagnetic Storms. *J. Geophys. Res. Atmos.* 121, 12520–12540. doi:10.1002/2015JD024212

Yando, K., Millan, R. M., Green, J. C., and Evans, D. S. (2011). A Monte Carlo Simulation of the Noaa Poes Medium Energy Proton and Electron Detector Instrument. Journal of Geophysical Research:. *Space Phys.* 116 (A10). doi:10.1029/2011ja016671

Zawedde, A. E., Nesse Tyssøy, H., Hibbins, R., Espy, P. J., Ødegaard, L.-K. G., Sandanger, M. I., et al. (2016). The Impact of Energetic Electron Precipitation on Mesospheric Hydroxyl during a Year of Solar Minimum. *J. Geophys. Res. Space Phys.* 121 (6), 5914–5929. doi:10.1002/2016ja022371

Conflict of Interest: The authors declare that the research was conducted in the absence of any commercial or financial relationships that could be construed as a potential conflict of interest.

Publisher's Note: All claims expressed in this article are solely those of the authors and do not necessarily represent those of their affiliated organizations, or those of the publisher, the editors and the reviewers. Any product that may be evaluated in this article, or claim that may be made by its manufacturer, is not guaranteed or endorsed by the publisher.

Paper V

Exploring the Predictability of the High-Energy Tail of MEE Precipitation Based on Solar Wind Properties

J.A. Salice, H. Nesse, E.M. Babu, C. Smith-Johnsen, and I.G. Richardson.
Journal of Geophysical Research: Space Physics, **128**, doi:10.1029/2022JA031194 (2023)

JGR Space Physics

RESEARCH ARTICLE
10.1029/2022JA031194

Exploring the Predictability of the High-Energy Tail of MEE Precipitation Based on Solar Wind Properties

J. A. Salice[1], H. Nesse[1], E. M. Babu[1], C. Smith-Johnsen[1], and I. G. Richardson[2,3]

[1]Birkeland Centre for Space Science, Department of Physics and Technology, University of Bergen, Bergen, Norway, [2]Heliophysics Science Division, NASA Goddard Space Flight Center, Greenbelt, MD, USA, [3]Department of Astronomy, University of Maryland, College Park, MD, USA

Key Points:

- The solar wind parameter ϵ best predicts the peak flux of the >292 keV electron precipitation independent of solar wind structure
- The delay in the peak flux of >292 keV electron precipitation relative to that of >43 keV electrons is influenced by solar wind speed
- On average, electron precipitation >292 keV persists 2–3 days longer than electron precipitation >43 keV

Correspondence to:

J. A. Salice,
Josephine.Salice@uib.no

Citation:

Salice, J. A., Nesse, H., Babu, E. M., Smith-Johnsen, C., & Richardson, I. G. (2023). Exploring the predictability of the high-energy tail of MEE precipitation based on solar wind properties. *Journal of Geophysical Research: Space Physics*, *128*, e2022JA031194. https://doi.org/10.1029/2022JA031194

Received 29 NOV 2022
Accepted 1 MAR 2023

The copyright line for this article was changed on 29 MAR 2023 after original online publication.

Abstract Medium Energy Electron (MEE) precipitation (≳30 keV) ionizes the mesosphere and initiates chemical reactions, which ultimately can reduce mesospheric and stratospheric ozone. Currently, there are considerable differences in how existing parameterizations represent flux response, timing, and duration of MEE precipitation, especially considering its high-energy tail (≳300 keV). This study compares the nature of ≳300 to ≳30 keV electron fluxes to better understand differences within MEE precipitation. The MEE fluxes are estimated from measurements by the Medium Energy Proton and Electron Detector (MEPED) onboard the Polar Orbiting Environmental Satellite (POES) from 2004 to 2014. The fluxes are explored in the context of solar wind drivers: corotating high-speed solar wind streams (HSSs) and coronal mass ejections (CMEs) alongside their associated solar wind properties. Three key aspects of ≳300 keV electron fluxes are investigated: maximum response, peak timing, and duration. The results reveal a structure-dependent correlation (0.89) between the peak fluxes of ≳30 and ≳300 keV electrons. The epsilon coupling function correlates well (0.84) with the ≳300 keV peak flux, independent of solar wind structure. The ≳300 keV flux peaks 0–3 days after the ≳30 keV flux peaks. The highest probability (~42%) occurs for a 1-day delay, while predictive capabilities increase when accounting for solar wind speed. The ≳300 keV flux response has the highest probability of lasting 4 days for both CMEs and HSSs. The results form a base for a stochastic MEE parameterization that goes beyond the average picture, enabling realistic flux variability on both daily and decadal scales.

Plain Language Summary Electrons with energies >30 keV precipitating into the Earth's atmosphere is known as medium energy electron (MEE) precipitation. Solar wind properties drive the rate and energy of MEE. MEE precipitation is a relevant solar forcing as it produces ozone-depleting substances. Variations in ozone concentration can modify the atmospheric temperature profile and lead to changes in atmospheric circulation that can map down onto surface climate. The community's capability of parameterizing MEE precipitation is an active field of research. This study aims to build a foundation for an MEE parameterization that represents realistic variability on daily and decadal scales by exploring the variability in the context of different solar wind properties. The study focuses on three key aspects regarding the differences within the energy spectrum of MEE precipitation: maximum response, timing, and duration. The key aspects are evaluated regarding the probability of a specific response. This study looks at an entire solar cycle (11 yr). It is found that solar wind properties, such as solar wind speed, can help determine the probability of a particular MEE response. The results from this paper will be key elements for constructing an MEE precipitation parameterization to be applied in a chemistry-climate model.

1. Introduction

Energetic particle precipitation (EPP) causes chemical changes in the upper atmosphere (≳50 km), for example, by creating NO_x and HO_x gasses (e.g., Smith-Johnsen et al., 2017; Verronen & Lehmann, 2013; Verronen et al., 2006; Zawedde et al., 2018). The increase of NO_x is particularly significant due to its long lifetime during high-latitude winter darkness, allowing for downward transportation and depletion of stratospheric ozone (Damiani et al., 2016; Maliniemi et al., 2021; Solomon et al., 1982). Ozone plays a significant role in stabilizing the atmosphere's radiation balance and climate system by absorbing incoming solar radiation and emitting long-wave infrared radiation. Hence, variation in ozone will cause changes in the atmospheric temperature profile and lead to changes in atmospheric circulation that can potentially map down onto surface climate (Baldwin & Dunkerton, 2001; Kidston et al., 2015; Maliniemi et al., 2016; Seppälä et al., 2016). The strengths of the

atmospheric ionization rates and chemical modulation highly depend on the number, energy, and type of particles hitting the atmosphere.

EPP consists of both protons and electrons. Auroral electron ($\lesssim$30 keV) and proton ($\lesssim$1 MeV) precipitation originating from the plasma sheet will ionize the lower thermosphere and upper mesosphere. Medium energy electrons (MEEs; $\gtrsim$30 keV) from the radiation belts deposit their energy throughout the upper mesosphere, whereas the high-energy tail of MEE ($\gtrsim$300 keV) can reach the upper stratosphere (Turunen et al., 2009). Occasionally, high-energetic precipitating protons from solar proton events (SPEs; 1–50 MeV) can ionize the stratosphere, where the production of NO_x and HO_x allows for a direct impact on stratospheric ozone (Jackman et al., 2005; Tyssøy & Stadsnes, 2015; Tyssøy et al., 2013; Zawedde et al., 2018).

The link between electron precipitation at auroral energies and how it affects NO_x in the lower thermosphere is well established (Marsh et al., 2004; Sinnhuber et al., 2011). Similarly, the effects of SPEs are fairly well quantified (Funke et al., 2011; Jackman et al., 2005; Tyssøy & Stadsnes, 2015; Tyssøy et al., 2013). However, knowledge gaps remain regarding the MEE precipitation spectrum, particularly when considering the high-energy tail. MEE precipitation is acknowledged as one of the relevant factors in understanding stratospheric ozone depletion (Matthes et al., 2017). Currently, the community's capability of parameterizing MEE precipitation is an active field of research (Babu et al., 2022; Beharrell et al., 2015; Duderstadt et al., 2021; Mironova et al., 2019; Partamies et al., 2021; Pettit et al., 2019; Tyssøy et al., 2019; Tyssøy, Partamies, Babu, Smith-Johnsen, & Salice, 2021; Tyssøy et al., 2021; van de Kamp et al., 2018, 2016). Instrumental challenges and different data handling result in a wide range of electron flux and ionization rate estimates (Tyssøy et al., 2021). This uncertainty propagates into chemistry-climate model projections of the associated chemical effects (Sinnhuber et al., 2022).

Geomagnetic indices are often used as proxies for precipitation. The lower part of the electron precipitation spectrum is known to correspond well with geomagnetic indices (e.g., Hendrickx et al., 2015; Østgaard et al., 2002; Y. Zhang & Paxton, 2008). The high-energy tail of MEE precipitation is more ambiguous (Turunen et al., 2009; Tyssøy, Babu, Smith-Johnsen, & Salice, 2021). The Coupled Model Intercomparison Project Phase 6 (CMIP6) provides climate projections in a multi-model context (WCRP, 2011). The current CMIP6 solar forcing recommendation utilizes van de Kamp et al. (2016)'s daily resolved model for MEE precipitation (Matthes et al., 2017). The model is based on the 0° Medium Energy Proton and Electron Detector (MEPED) measurements onboard the NOAA Polar Orbiting Environmental Satellites (POES) and is scaled by the Ap index. Several limitations to this approach have been established (e.g., Mironova et al., 2019; Pettit et al., 2019; Tyssøy et al., 2019; Tyssøy et al., 2021).

Tyssøy et al. (2019) find that the Ap-based model falls short in reproducing flux levels, variability associated with strong geomagnetic storms, and the duration of storms. Typically, the high-energy tail of MEE acts differently compared to the lower energies with respect to the timing (Ødegaard et al., 2017) and duration (Longden et al., 2008) of the flux response. Moreover, as the parameterization developed in van de Kamp et al. (2016) is based on an average response to geomagnetic activity, it is likely to downplay the impact of extreme events (Tyssøy et al., 2021). To model the effect of the transient forcing of MEE on the atmosphere, a correct representation of the daily MEE variability over a wide range of energies with respect to both the background drizzle and storm periods is necessary. Additionally, an average representation of the typical storm might not reflect the variability throughout a solar cycle. In particular, the solar wind drivers of MEE exhibit a fairly strong solar cycle dependence (e.g., Asikainen & Ruopsa, 2016; Kilpua, Balogh, et al., 2017; Kilpua, Koskinen, et al., 2017), potentially causing a systematic bias on decadal scales (Tyssøy et al., 2019). An accurate representation of MEE precipitation will allow for better parameterization on both daily and decadal scales.

The solar wind fuels the magnetospheric processes that accelerate and scatter electrons trapped in the radiation belts. Coronal mass ejections (CMEs) and high-speed solar wind streams (HSSs) are the primary large-scale heliospheric solar wind structures driving geomagnetic disturbances (e.g., J. Zhang et al., 2007). These structures occasionally occur in rapid sequences or are merged, leading to intense geomagnetic disturbances (Asikainen & Ruopsa, 2016; Kilpua, Balogh, et al., 2017; Kilpua, Koskinen, et al., 2017). CMEs consist of various components such as shocks, sheaths, ejecta, and clouds (for reviews on CMEs, see e.g., Kilpua, Balogh, et al., 2017; Kilpua, Koskinen, et al., 2017; Zurbuchen & Richardson, 2006). HSSs are often accompanied by a corotating interaction region (CIR) leading the stream (for a review on HSSs and CIRs, see Richardson, 2018). Generally, CMEs tend to be brief ($\sim$1 day) and may include strong, slowly varying magnetic field components, while HSSs tend to last longer and have fluctuating magnetic field components (e.g., Borovsky & Denton, 2006; Kataoka &

Table 1
Nominal Detector Responses in the Three Electron Channels E1, E2, and E3 of the SEM-2 MEPED Electron Detector (Evans & Greer, 2004) and the New Optimized Integral Energy Limit for the Different Channels (Ødegaard et al., 2017)

Energy channel	Nominal lower limit [keV]	New optimized lower limit [keV]
E1	>30	>43
E2	>100	>114
E3	>300	>292

Miyoshi, 2006; Kilpua, Balogh, et al., 2017; Kilpua, Koskinen, et al., 2017). Throughout a solar cycle, HSSs are nearly always (except at solar maxima) more frequent than CMEs (Asikainen & Ruopsa, 2016). The fundamentally different solar wind properties drive different geomagnetic disturbances as well as different MEE precipitation characteristics (e.g., Borovsky & Denton, 2006; Longden et al., 2008).

This study explores daily MEE precipitation in the context of its solar wind drivers and the associated solar wind properties, such as solar wind speed and interplanetary magnetic field (IMF). Notably, the focus is on the behavior of the high-energy tail compared to low-energy MEE precipitation. The low-energy MEE is generally easier to quantify due to its high correspondence to geomagnetic activity in contrast to the high-energy tail. The MEE bounce loss cone (BLC) fluxes are estimated based on observations from MEPED onboard POES/METOP over 11 yr from 2004 to 2014. Periods of isolated CME- and HSS-driven solar wind structures and periods when they are in close sequence are examined. Three key aspects of $\gtrsim$300 keV electron flux are investigated:

- The maximum flux response.
- The timing of the maximum flux response.
- The duration of the flux response.

The key aspects are evaluated regarding the probability of a specific response. The goal is to identify variables that increase the accuracy of a daily MEE parameterization to be applied in a chemistry-climate model. This paper is organized as follows: Section 2 describes the data and methods used, Section 3 presents the results which are discussed in Section 4, and finally, conclusions of this study are provided in Section 5.

2. Data and Method

2.1. MEE Flux

The series of NOAA/POES and EUMETSAT/MetOp satellites are Sun-synchronous, low-altitude polar-orbiting spacecraft. The spacecraft circle at ~850 km altitude with a period of ~100 min, resulting in 14–15 orbits per day (Evans & Greer, 2004). The MEPED instrument is mounted on the POES series and three of the MetOp spacecraft. The combined measurements from the different satellites give a near-continuous observation of MEE precipitation from 1979 until today.

MEPED consists of a set of eight separate solid-state particle detector systems. Two are proton solid-state detector telescopes, two are electron solid-state detector telescopes, and the remaining four are omni-directional detector systems for high-energy protons measured over a wide range of angles (Evans & Greer, 2004). The electron detectors monitor the intensity of electrons in three bands from 30 to 2,500 keV (Evans & Greer, 2004). The nominal electron energy limits for the electron telescope in the three bands E1, E2, and E3 as given in Evans and Greer (2004) are listed in Table 1. When in operation, the true electron energy limits depend on the incoming electron energy spectrum (Yando et al., 2011). The new optimized effective integral energy limits and associated geometric factors are based on a series of realistic power laws and exponential spectra and were determined by Ødegaard et al. (2017) by applying the geometric factors given in Yando et al. (2011).

The electron solid-state detector telescopes consist of a 0° and 90° telescope. The 0° telescope is oriented radially outward along the Earth-satellite connecting axis. The 90° telescope is perpendicular to the 0° telescope and anti-parallel to the satellite's velocity vector. Both telescopes are rotated away from the described axis by 9° to ensure a clear field of view (Evans & Greer, 2004). Charged particles gyrate along the magnetic field lines. The angle between the velocity vector of a particle and the magnetic field line is known as the particle's pitch angle. This angle determines whether the particle will be lost to the atmosphere or mirrored back along the magnetic field. The atmospheric BLC is defined as the range of pitch angles at which particles will be lost. The size of the BLC changes with latitude and longitude due to variations in the magnetic field strength. In MEPED, the 0° telescopes will mainly measure atmospheric BLC particles when traveling across high geomagnetic latitude, while the 90° telescopes will mainly measure particles at the edge or outside of the BLC (Rodger et al., 2010).

Separately, the two telescopes do not give an accurate estimate of the BLC electron flux (Tyssøy et al., 2016) as the 90° telescope will give an overestimation and the 0° telescope an underestimation. This is because the

energetic electron fluxes are often strongly anisotropic with decreasing fluxes toward the center of the BLC (Tyssøy et al., 2016). Tyssøy et al. (2016) estimated a complete BLC flux for each electron energy channel by combining measurements from both telescopes with electron pitch angle distributions from theories of wave-particle interactions in the magnetosphere. The Focker-Planck equation for particle diffusion (Kennel & Petschek, 1966; Theodoridis & Paolini, 1967) is solved for a wide range of diffusion coefficients. The solutions are then transformed to the satellite altitude and stored in a look-up table. The ratio between the fluxes detected by the 0° and 90° detector is compared to the theoretical solution considering the telescope's viewing directions relative to the magnetic field. Finally, the size of the BLC is predicted based on the International Geomagnetic Reference Field model and is applied to estimate the precipitating fluxes. The BLC flux estimate is done separately for each energy channel, as the level of particle diffusion will vary with energy. A detailed explanation of the method can be found in Tyssøy et al. (2016).

This study applies the BLC fluxes with the new optimized effective integral limits E1 (>43 keV) and E3 (>292 keV). The BLC fluxes represent daily fluxes averaged over 55°–75° corrected geomagnetic (CGM) latitude and all magnetic local times for a full solar cycle from 2004 to 2014. During this period, up to seven satellites have been operational, all with the newest instrument package SEM-2. More details of the operating satellites and data coverage for the specific time period can be found in Babu et al. (2022) and Tyssøy, Partamies, Babu, Smith-Johnsen, and Salice (2021). For simplicity, >43 and >292 keV electron fluxes will be referred to as E1 and E3, respectively.

2.2. Solar Wind Structure and Parameters

The near-Earth solar wind is divided into three basic flow types:

- Corotating high-speed streams that originate from coronal holes at the Sun.
- Transient flows associated with CMEs at the Sun.
- Slower, interstream solar wind typically associated with the streamer belt at the Sun.

Classification of these three structures for every day of the 11 yr period from 2004 to 2014 was made using the same methods discussed by Richardson and Cane (2012). Their list of daily resolution solar wind structures, based on a 1 hr resolution assessment of these structures, includes the day the structure starts to the day it ends, even if that solar wind structure did not predominately occur on these days. The classifications are based on a variety of data, including near-Earth solar wind parameters from the OMNI database, geomagnetic activity data, and energetic (~0.1–100 MeV) particle and cosmic ray observations (Richardson & Cane, 2012). Since the near-Earth solar wind data is essentially continuous throughout the investigated period, Richardson and Cane (2012)'s classifications are considered representative and suitable for this study.

The corotating high-speed streams, denoted as HSSs in this paper, typically have solar wind speed $v \gtrsim 450$ km/s and include both the high-speed stream and CIR where the leading edge of the high-speed stream interacts with the preceding slower, cooler, and denser solar wind. The transient flows originating with CMEs at the Sun include interplanetary CMEs (ICMEs), the manifestations in the solar wind of the CMEs, and the associated upstream shocks and post-shock/sheath regions (Richardson & Cane, 2012). Richardson and Cane (2012) refer to ICMEs and their upstream shocks and sheaths collectively as "CME-associated" structures. This paper follows the same approach and, for brevity, uses "CME" to refer to these structures. More information on the respective data sets and how the different structures are identified can be found in Richardson and Cane (2012) and references therein.

The solar wind magnetic field strength and direction as well as the solar wind speed are primary drivers of geomagnetic activity. In this paper, the IMF component Bz (in GSM-coordinates) and plasma flow speed, v, were retrieved from the OMNI 2 database with a daily resolution from 2004 to 2014. In addition, the epsilon parameter, ϵ, which is based on Bz and v and which gives a general idea of the energy transfer between the solar wind and the magnetosphere, was retrieved from the SuperMAG database (Gjerloev, 2012) with daily resolution over the same time interval. ϵ is given by:

$$\epsilon = \frac{4\pi}{\mu_0} v B^2 sin^4\left(\frac{\theta}{2}\right) l_0^2 \quad (1)$$

Equation 1 is based on Akasofu (1981) and is given in SI units (Watt) by Koskinen and Tanskanen (2002). In Equation 1, $4\pi/\mu_0 = 10^7$, v is solar wind velocity, B is the magnitude of the solar wind magnetic field, θ is the clock angle (the angle between geomagnetic north and the projection of the IMF in the plane transverse to the radial direction), and l_0 is seven times the Earth's radius ($l_0 = 7R_E$).

The current parameterization for MEE precipitation recommended for CMIP6 is represented as daily averages based on daily Ap values (Matthes et al., 2017). Moreover, the high-energy tail of the MEE spectra often peaks after 1–2 days (Ødegaard et al., 2017; Tyssøy, Partamies, Babu, Smith-Johnsen, & Salice, 2021). Because of this, the goal of our study is not to attempt to understand the role of solar wind drivers over short time intervals but to reveal their stochastic role in the behavior of precipitating the high-energy tail of MEE. Tyssøy, Partamies, Babu, Smith-Johnsen, and Salice (2021) demonstrate that the MEE precipitating fluxes are determined by accumulated geomagnetic activity. As such, it is not the specific short periods of negative Bz or positive ϵ that determine the daily MEE precipitation. Hence, we apply daily averages of the hourly determined solar wind structures, the 1 min Bz, v, and ϵ parameters alongside daily averaged MEE fluxes.

2.3. Method

In this study, CMEs and HSSs are categorized into single and combined events. The combinations of events include a CME followed by an HSS and vice versa. In the 11 yr of interest, 420 events were selected based on the requirements that they were classified as a structure for at least 1 day and had slower, interstream solar wind the day before and after. However, 12 events were removed because of gaps in the electron flux data. Additionally, 52 events with fluxes falling below 250 electrons/($cm^2 \cdot s \cdot sr$) were removed because they were close to the detectors noise level of around 100 electrons/($cm^2 \cdot s \cdot sr$). Moreover, 107 events, where either E1 or E3 reached their highest flux before the solar wind event, were removed. These events would have given misleading flux responses, as this study evaluates the electron fluxes within the solar wind structure and does not consider pre-event fluxes. Based on these criteria, 249 events within the 11 yr period were retained: 34 CMEs, 181 HSSs, 17 CME + HSSs, and 17 HSS + CMEs.

Figure 1 shows a superposed epoch analysis (SEA) over a 14-day period of E1 and E3 as well as the parameters Bz, v, and ϵ for all 249 events, denoted as the Base. The onset is defined by the peak in E1. Previous studies have shown that the E1 evolution and maximum flux response are fairly well correlated with geomagnetic activity (Tyssøy, Partamies, Babu, Smith-Johnsen, & Salice, 2021; van de Kamp et al., 2016). The evolution of E1 and the three solar wind parameters in Figure 1 confirms this correlation. Hence, this study targets the behavior of the E3 peak relative to the E1 peak and, therefore, defines the onset based on E1. In addition, choosing the flux peak instead of flux rise avoids the pitfall of MEE radiation belt fluxes being subject to adiabatic variability where it is not always evident when the flux rise starts (Ødegaard et al., 2017). Moreover, the peak flux is a pragmatic parameter to apply in a model assuming a fairly consistent rise time. In this study, the peak fluxes refer to the highest flux response within the solar wind structure period.

Figure 1 captures the long duration of elevated fluxes, particularly for E3. Note that other events may occur during the 8 days following onset, which can give rise to some of the features in the SEA. When evaluating the E3 peak, as well as the delay between E1 and E3, activity throughout the 8-day period after the onset does not affect the interpretations. However, when evaluating the duration, events with activity throughout the 8-day period after the onset are discarded (see Section 3.4).

Under the assumption that it is the accumulated effect of solar wind drivers that is responsible for E3 characteristics, we apply a 4-day average of the three parameters Bz, v, and ϵ from 2 days before the onset (−2 days) to 1 day after (+1 day). This captures the main energy transfer period as illustrated by ϵ in the lower panel of Figure 1, which occurs before the average E3 peak. The respective time interval is optimized and confirmed based on regression analysis between E3 and different time intervals for ϵ. Note that Bz averages out around zero as it oscillates between negative and positive values throughout the day. A daily average will not capture the oscillation but can still indicate if Bz was more negative or positive throughout the day and if large negative values occur.

SEAs of the flux response in the E1 (black) and E3 (green) flux channels during the different events are presented in Figure 2. The top panel shows Base events and gives a general picture of how active solar wind periods affect electron precipitation. The four subsequent panels show the flux evolution during CMEs, HSSs, CME + HSSs, and HSS + CMEs. As HSSs make up ∼73% of all the events, they will correspond well with the Base. All five panels list the E1 and E3 peaks with the associated timings. In addition, the transition between structures within the combined events is marked on the upper x-axis. Note that one HSS + CME event does not change from an HSS-driven structure to a CME-driven one until after the plotted period of 8 days from onset. This event is not disregarded as we do not differentiate between electron fluxes reaching their peak in a certain structure of the combined events.

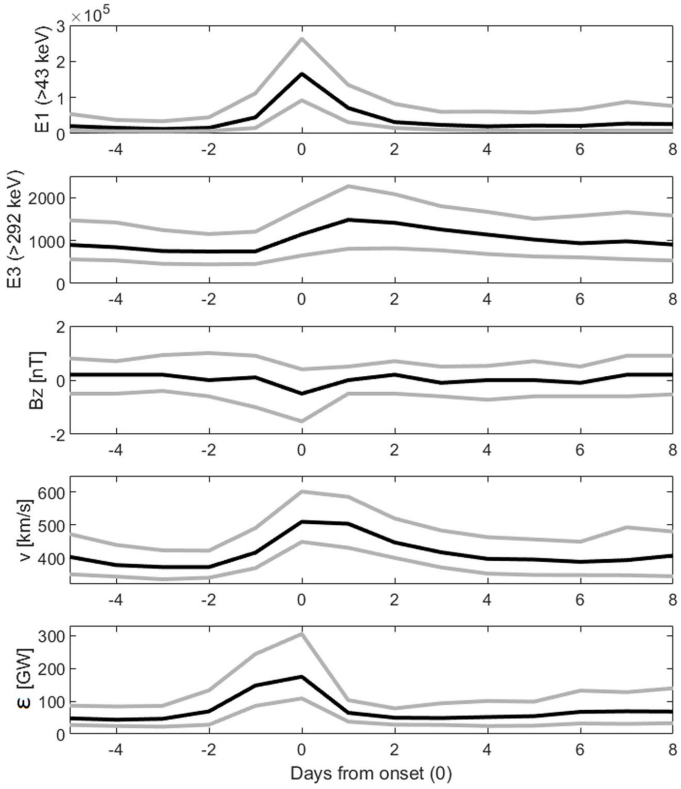

Figure 1. Superposed epoch analysis of the evolution of parameters for all events in this study (Base). From the top: E1 (>43 keV), E3 (>292 keV), *Bz*, *v*, and ϵ. The fluxes are in $cm^{-2}s^{-1}sr^{-1}$. The onset is defined as the E1 maximum flux response within the solar wind structure period (denoted as the E1 peak). The gray lines show the lower and upper quartiles.

The electron flux channels E1 and E3 represent two different energy intervals within the MEE range, the latter being the high-energy tail. As the magnetospheric acceleration and scattering processes are energy-dependent (Millan & Thorne, 2007), it is expected that the nature of particles precipitating at these two energy intervals also differs. The E1 maximum response is higher as it not only represents an integral spectrum but naturally has a higher flux due to the flux always decreasing with higher energy. However, it is evident that the broadness of the E1 and E3 peaks typically differs. A prolonged E3 response implies a significant accumulated effect. More time is needed to accelerate and scatter electrons at higher energies (>292 keV) which can lead to a delay in the E3 response compared to that of E1 (Ødegaard et al., 2017; Tyssøy, Partamies, Babu, Smith-Johnsen, & Salice, 2021). As solar wind drives the acceleration and scattering processes of electrons in the magnetosphere, this study will examine to which degree different solar wind structures generate different characteristic flux responses in the high-energy tail (E3) of MEE precipitation.

3. Results

3.1. The General Flux Evolution

The average flux evolution presented in Figures 1 and 2 represents an overview of the data used in this study. The figures demonstrate the expected differences between the two energy channels of MEE precipitation. Both Figures 1 and 2 show that the E3 peak is typically about two orders of magnitude smaller than that of E1. From

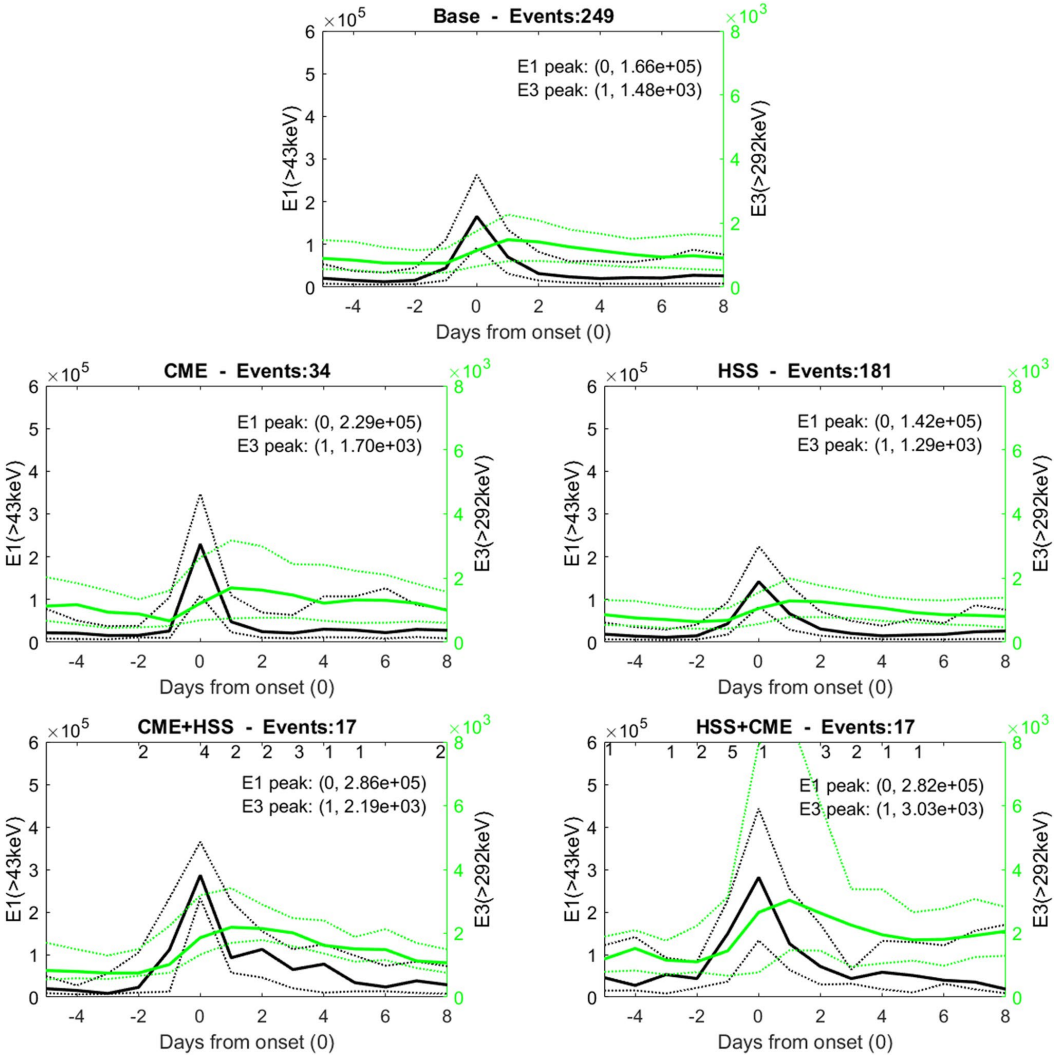

Figure 2. SEAs of the electron flux for the E1 (>43 keV) (black) and E3 (>292 keV) (green) energy channels during different solar wind structures given in $cm^{-2}s^{-1}sr^{-1}$. The *x*-axis indicates days from the onset defined as in Figure 1. The dotted lines show the lower and upper quartiles. The coordinates of the E1 and E3 peaks are presented in the upper right corner. The numbers at the top of the bottom two panels indicate the number of events with a structural solar wind change on a specific day. Note that the *y*-axis scaling of the black and green curves are different; the green *y*-axis is on the right-hand side. However, the *y*-axes are the same for all panels.

Figure 2, the average HSS has considerably lower flux responses than other structures. The two combined structures have higher E1 and E3 average peaks than single structures. HSS + CMEs show large variability in E3 as the upper and lower quartiles indicate extremely high and low flux responses, respectively. E3 typically has the highest flux responses within 1 day after the E1 peak. Also evident is the relatively steep rise and fall of E1 around the onset compared to the broader E3 response. The following results explore potential prediction capabilities for the E3 peak, the delay of the E3 peak relative to that of E1, and the duration of E3 enhancement in relation to solar wind properties.

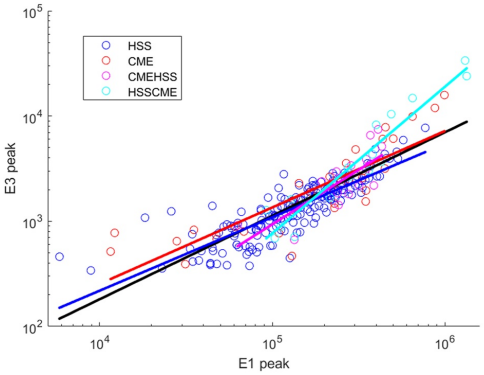

Structure	r	p-value	a	b
BASE	0.89	0	0.79	-2.10
CME	0.94	0	0.73	-1.15
HSS	0.91	0	0.70	-1.04
CME+HSS	0.74	0.0007	1.03	-5.07
HSS+CME	0.96	0	1.39	-9.39

Figure 3. Scatter plot of the dependence the E3 (>292 keV) peak has on the E1 (>43 keV) peak. The two fluxes are given in $cm^{-2}s^{-1}sr^{-1}$. The regression lines for the different structures, including the base (black), are plotted on top. The fluxes are on a log-log scale. The correlation coefficients (r), the statistical significance values (p-value), and the line fitting parameters, a and b, for the different structures are shown in a table to the right.

3.2. The E3 (>292 keV) Peak Flux

Figure 3 shows a log-log scatter plot of how the E3 peak depends on the peak of E1. On the right is a table of the correlation coefficients (r), p-values, and line-fitting parameters a and b. Note that the peak fluxes refer to the maximum flux response within the solar wind structure period. The E3 peak scales consistently to that of the E1 peak with a correlation coefficient of 0.89 for all events (Base). Independently, the solar wind structures also have high correlation coefficients (>0.90), with the exception of CME + HSSs, which have a correlation coefficient of 0.74. CMEs and HSSs have similar rates of change (≈0.70), while the rate of change for the combined structures is higher (>1.00). The E3 peak during HSS + CMEs has a significantly stronger sensitivity to changes in the E1 peak with a rate of change equal to 1.39. For high E1 values ($>3 \times 10^5 cm^{-2}s^{-1}sr^{-1}$), Figure 3 shows that the fit derived from the Base events would underestimate the strong HSS + CME response due, particularly, to the dominance of the weaker HSS response.

Figure 4 shows the same as Figure 3 just for how the E3 peak depends on different solar wind properties. From top to bottom, the solar wind properties are Bz, v, and ϵ. The properties are averaged over 4 days, from 2 days before to 1 day after onset. As in Figure 3, the correlation between the peak fluxes and the solar wind parameters is portrayed in a scatter plot with the corresponding linear regression lines for each structure. Note that the Bz and v plots are semi-log plots while ϵ is a log-log plot. To the right of each scatter plot is a table with the same content as in Figure 3.

When considering the Base presented in Figure 4, Bz (top panel) and v (middle panel) correlate poorly with the E3 peak as the correlation coefficients are −0.51 and 0.49, respectively. However, the correlation between the Base and ϵ (bottom panel) is high (0.84). ϵ has small p-values (<0.05) and the highest correlation coefficients (r) for the various solar wind structures. An exception is found for CMEs where the correlation coefficient between solar wind speed and E3 is higher (0.75). The relation between the ϵ coupling function and the E3 peak (bottom panel) shows that the rates of change for the different structures are fairly similar, and the lines are nearly superposed. In fact, CMEs and HSSs have the same rate of change (1.16).

The poor correlation between E3 and Bz (top panel in Figure 4) might be due to the negative and positive variations in Bz being averaged over 4 days, whereas it is the negative Bz periods that would most effectively impact E3.

3.3. The Delay of E3

To utilize the correlations presented in Figures 3 and 4, information on the difference in timing between the two peak fluxes is needed. Figure 5 shows the probability of a given delay in the E3 peak for the different structures.

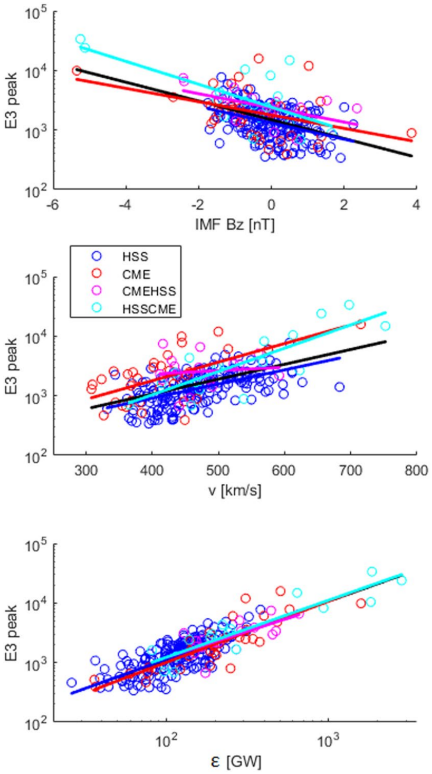

Structure	r	p-value	a	b
Base	-0.51	0	-0.38	11.87
CME	-0.29	0.1016	-0.35	11.89
HSS	-0.40	0	-0.39	11.78
CME+HSS	-0.67	0.0035	-0.16	12.44
HSS+CME	-0.80	0.0001	-0.33	12.33

Structure	r	p-value	a	b
Base	0.49	0	0.0059	9.19
CME	0.75	0	0.0057	9.67
HSS	0.52	0	0.0067	8.66
CME+HSS	0.02	0.9371	0.0030	11.07
HSS+CME	0.75	0.0006	0.0058	9.49

Structure	r	p-value	a	b
Base	0.84	0	0.96	7.21
CME	0.63	0.0001	1.16	5.92
HSS	0.76	0	1.16	6.28
CME+HSS	0.77	0.0003	0.49	9.79
HSS+CME	0.85	0	0.63	9.00

Figure 4. Scatter plots of the dependence the E3 (>292 keV) peak [$cm^{-2}s^{-1}sr^{-1}$] has on the 4-day averaged IMF *Bz* (top), *v* (middle), and ϵ (bottom). The regression lines for the different structures, including the Base (black), are plotted on top. *Bz* and *v* are on a log-lin scale while ϵ is on a log-log scale. The correlation coefficients (*r*), the statistical significance values (*p*-value), and the line fitting parameters, *a* and *b*, for the different structures are shown in a table to the right of each plot.

A 0-day delay indicates that E3 peaks within the same day as E1, a 1-day delay that E3 peaks within the following day, and so on. The highest probability is for a 1-day delay of the E3 peak, independent of solar wind structure (see Figure 5). A high probability for a 1-day delay is expected based on the SEAs shown in Figures 1 and 2. However, the delay varies from zero to 3 days. CMEs have the highest probability (32%) for a 0-day delay and the lowest probability for a 3-day delay (9%). Both CME and HSS + CME events have a higher probability (32% and 29%, respectively) for a 0-day delay than a delay of more than 1 day.

All structures have >60% chance for a 1-day delay of the E3 peak. A higher resolution is needed to see differences within these days. Still, based on daily variability, this study targets parameters that influence the timing of the maximum response in E3 from 0 to 3 days.

Figure 6 shows the average *Bz*, *v*, ϵ, and E1 peak values for the different delays in the E3 peak for CMEs (red) and HSSs (blue). (The low statistics of the combined structures resulted in large errors and insignificant results, and are therefore not shown here.) In general, none of the parameters show a significant trend in influencing the delay of the E3 peak. Still, a weak tendency is evident in the solar wind speed, where slower speed might be associated with a longer delay.

Figure 7 shows the probabilities of different delays in the E3 peak with regard to solar wind speed. The *x*-axis indicates the speeds at which the 4-day average *v* exceeds. The *y*-axis for the two top panels shows the probability of the indicated delay with a solar wind speed above the given *x*-value, while the bottom panels show the number

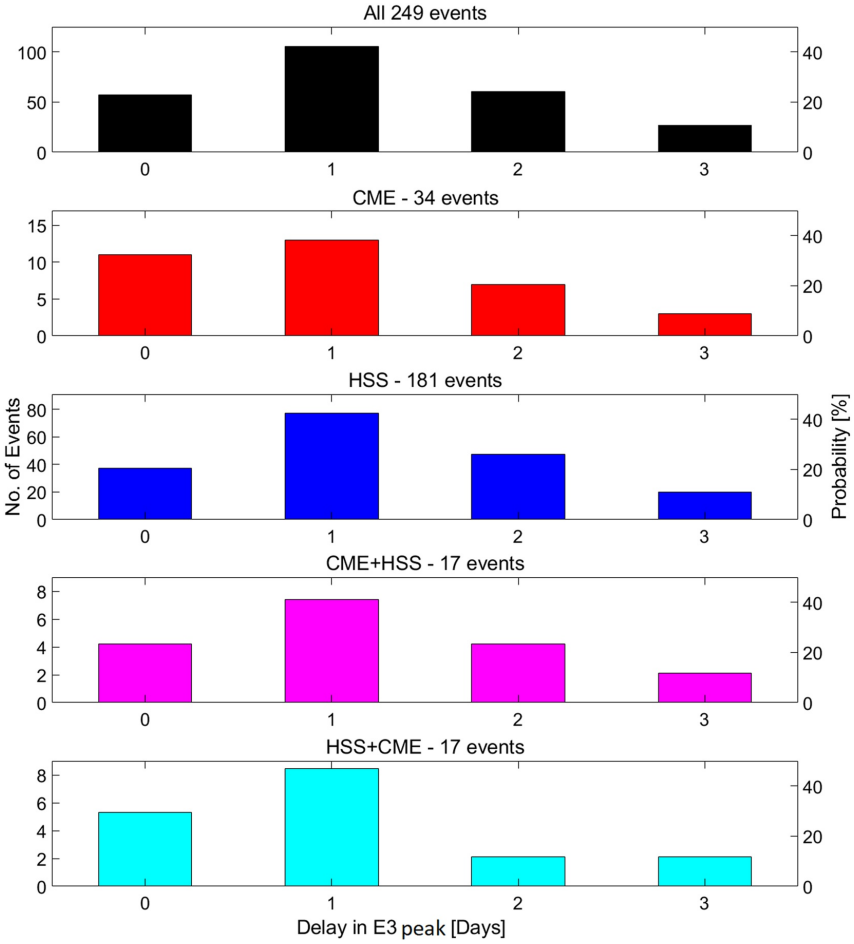

Figure 5. The delay in the E3 (>292 keV) peak relative to the E1 (>43 keV) peak associated with the different solar wind structures showed in days on the *x*-axis. The left *y*-axis shows the number of events with a certain E3 delay, and the right *y*-axis shows the probability of this delay.

of events with an average v above the given x-value. Only results for v are shown as Bz, ϵ, and E1 showed little influence on the delay when examined in the same manner as presented in Figure 7.

Figure 7 shows that there is a threshold in the solar wind speed at $v > 400$ km/s and $v > 550$ km/s for CMEs and HSSs, respectively, above which the probability of a 0-day delay increases substantially. For CMEs, this probability increases from 47% at $v > 400$ km/s to 75% at $v > 475$ km/s, while $v > 350$ km/s reduces the chance of a two- and 3-day delay to below 10%. For HSSs, a 1-day delay is dominant up until ∼425 km/s, where the probability of a 0-day delay increases consistently and reaches the same probability (41%) of a 1-day delay at $v > 550$ km/s.

3.4. The Duration of the Precipitation Events

To evaluate the duration of the flux responses, the full width at the half-maximum value of the peak for both E1 and E3 was calculated. Twelve events were discarded as E1, E3, or both did not fall below this value within 8 days

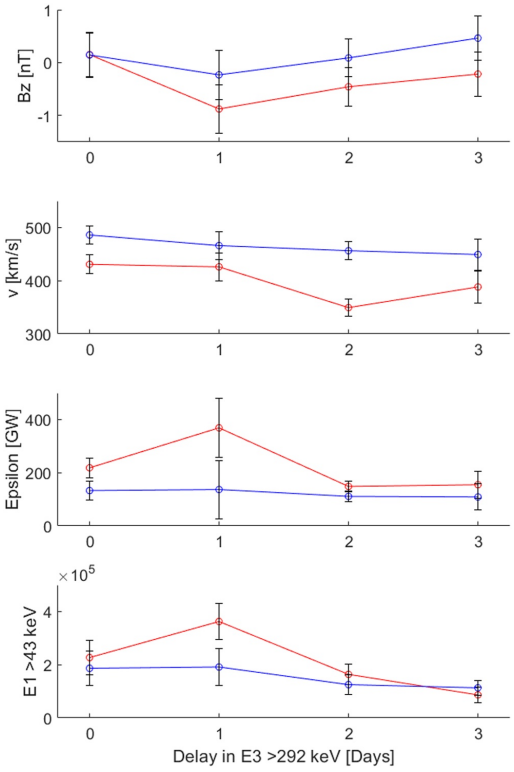

Figure 6. The average Bz, v, ϵ, and maximum E1 (>43 keV) [$cm^{-2}s^{-1}sr^{-1}$] values associated with the delay of the E3 (>292 keV) peak for CMEs (red) and HSSs (blue). The error bars show the standard deviations of the average values.

from the onset due to new activity. This led to a loss of 17 HSSs and three HSS + CMEs. The duration of the E1 and E3 responses and their occurrence probability are presented in Figure 8.

Generally, when considering the Base (top), the E3 response lasts longer (>2 days) compared to the duration of the E1 response (<3 days). Figure 8 also shows that CMEs have the highest probability (62%) for an elevated E1 response of just 1 day, while for HSSs, CME + HSSs, and HSS + CMEs, a duration of 2 days is most common. The duration of the high-energy tail (E3) is most likely to last 4 days for both CMEs and HSSs, with a probability of 32% and 23%, respectively. Even though CMEs have a higher probability for a shorter E1 response, the highest probability of the E3 duration is still 4 days. In fact, 79% of CMEs have an E3 duration of 3 days or longer. The combined structures, though having low statistics, also indicate longer flux enhancements of the high-energy tail compared to E1.

No significant tendency was evident between the duration of E3 and Bz, v, or ϵ when examined in the same manner as delay in Figures 6 and 7.

4. Discussion

In this study, the high-energy tail of MEE precipitation has been compared to the E1 response and investigated in the context of solar wind drivers and the associated v, Bz, and ϵ parameters concerning the following features.

- The maximum flux response
- The delay in maximum flux response
- The duration of the flux response

An in-depth understanding of these three key parameters is necessary to represent the entire MEE precipitation spectrum realistically. Evaluating each parameter's potential in determining the probability of a specific response paves the way for understanding which variables can be applied to increase the accuracy of an MEE parameterization on both daily and decadal scales.

4.1. The Maximum Precipitating Fluxes

On average, HSSs have lower MEE flux responses than CMEs and combined structures (see Figure 2). Consistent with our results, Asikainen and Ruopsa (2016) showed that the average precipitating fluxes in 2004–2014 were higher for CMEs compared to HSSs for the E1 and E3 energy channels. The relatively low HSS flux response might be partly because the precipitating MEE flux is averaged over a wide latitude band from 55° to 75°N and the precipitation region associated with HSS typically does not expand as widely as CMEs (Babu et al., 2022). The upper quartile of the MEE flux for HSS + CMEs in Figure 2 demonstrates that these structures can trigger extreme MEE flux levels in both E1 and E3. Kilpua, Balogh, et al. (2017) and Kilpua, Koskinen, et al. (2017) also pointed out the potential of severe geomagnetic storms associated with the combination of solar wind structures. Moreover, Asikainen and Ruopsa (2016) found that the efficiency of both HSSs and CMEs in producing MEE precipitation peaks in the declining phase of the solar cycle, where these events often occur simultaneously or in close sequence.

HSSs are more frequent throughout a solar cycle than CMEs (Asikainen & Ruopsa, 2016) and, in this study, constitute 73% of the identified structures during the investigated 11 yr. As the average HSS has considerably weaker flux responses compared to CME-related events, an MEE parameterization based on "the average event" will underestimate the potentially strong impact associated with CME-related activity and exaggerate flux levels associated with the common HSSs. Hence, such a model will not be able to represent the variability associated with MEE precipitation for daily and decadal scales. Tyssøy et al. (2019) showed that van de Kamp et al. (2016)'s ApEEP model, which is scaled by the geomagnetic index Ap based on median flux responses, falls short in reproducing the flux levels and variability associated with strong geomagnetic storms. Additionally, Tyssøy

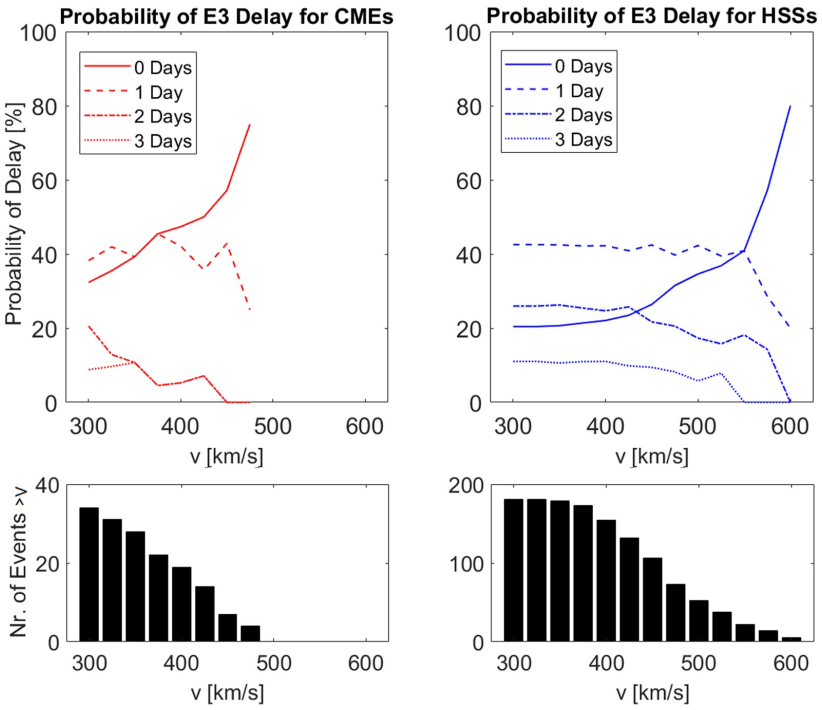

Figure 7. The solar wind speed-dependent probability of the delay in the E3 (>292 keV) peak for CMEs (red) and HSSs (blue). The *y*-axis of the two top panels shows the probability of the indicated delay dependent on events with average solar wind speeds that exceed the indicated *x*-axis value. The *y*-axis of the two bottom panels shows the number of events with average solar wind speeds which exceed the indicated *x*-value.

et al. (2021) compared eight different ionization rates, all based on MEPED observations, during an active period of March/April 2010, including a period of combined events. The comparison showed that the ApEEP-based model predicts significantly weaker ionization rates than other estimates, particularly when considering the high-energy tail. Hence, a more realistic representation of MEE precipitation might be achieved by considering the probability of flux response variations regarding solar wind structure.

Figure 3 implies that knowledge of the E1 peak will enable the prediction of the peak flux of the high-energy tail as the correlation coefficient for the Base events is 0.89. Independently, the solar wind structures all have a high correlation (>0.90), with the exception of CME + HSSs, which have a low correlation (0.74). The E3 peak during combined structures stands out as it has a stronger sensitivity to changes in E1. Particularly, HSS + CMEs stand out with a significantly higher rate of change of 1.39. As HSSs strongly dominate the average structure, a model based on the average relationship will systematically underestimate the high-energy tail of MEE precipitation during combined events when the E1 response is high ($>3 \times 10^5 \mathrm{cm}^{-2}\mathrm{s}^{-1}\mathrm{sr}^{-1}$).

Figure 4 reveals ϵ as a key parameter to determine the peak of E3, independent of solar wind structure. Ødegaard et al. (2017) reported a linear relationship between the energy input into the magnetosphere and precipitation of relativistic electrons by studying 41 weak and moderate geomagnetic storms driven by CIRs. Our study suggests, however, that this relationship is independent of the driving solar wind structure. This is not self-evident as multiple studies suggest that the energy partitioning within the magnetosphere might be different for different solar wind structures (N. E. Turner et al., 2009).

Note that to utilize the dependency between either the E1 and E3 peaks or the E3 peak and the ϵ parameter in a model, the timing of the flux peaks needs to be known. The timing of the E1 peak corresponds well with the

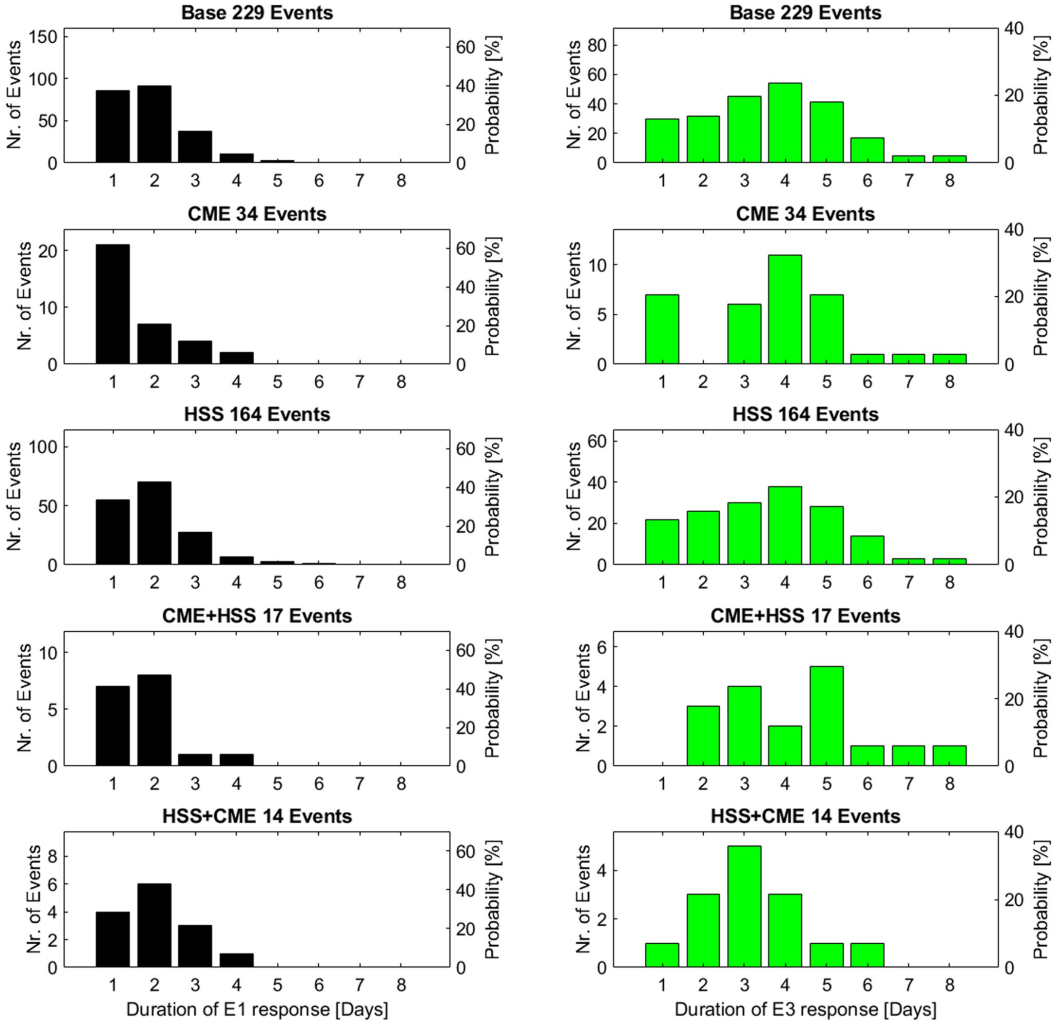

Figure 8. Probability of the duration [days] of E1 (>43 keV) and E3 (>292 keV) for the four different solar wind structures. E1 is presented in black to the left, and E3 in green to the right. From top to bottom, the solar wind structures are Base, CME, HSS, CME + HSS, and HSS + CME.

indices Bz, v, and ϵ (see Figure 1). Previous studies have also shown that the E1 peak and timing are fairly well correlated with geomagnetic activity (Tyssøy, Partamies, Babu, Smith-Johnsen, & Salice, 2021; van de Kamp et al., 2016). However, the timing of the E3 peak differs from that of E1.

4.2. Delay

Figure 5 shows that the E3 peak has the highest probability of occurring 1 day after onset. Evidence of delayed electron flux responses with increasing electron energy has also been documented in other studies (Li et al., 2005; Longden et al., 2008; Ødegaard et al., 2017; Tyssøy, Partamies, Babu, Smith-Johnsen, & Salice, 2021). Li et al. (2005) found solar wind speed to be a dominant controlling parameter for electron energies from 50 keV to 6 MeV. They identified an energy-dependent time shift of approximately 1 day between 50–75 and 225–300 keV,

consistent with our findings. A similar time shift for the MEE high-energy tail was also found by Longden et al. (2008) and Ødegaard et al. (2017). Moreover, Tyssøy, Partamies, Babu, Smith-Johnsen, and Salice (2021) investigated the predictability of the AE index for MEE precipitation. They demonstrated how high predictability could be achieved when accounting for the delayed response of the high-energy tail ($\gtrsim$300 keV) by accumulating the geomagnetic activity over time, taking into account the electron flux lifetimes.

The presence of a time delay is consistent with the view of electrons in the radiation belts being accelerated to progressively higher energies over time (Horne et al., 2005). Both Horne et al. (2005) and Rodger et al. (2010) observed the delay in trapped electron particle energies and found an energy-dependent time delay.

This study finds a spread of 0–3 days in the delay of the E3 peak. CMEs have higher probabilities for a fast response than the other solar wind structures as the high-energy tail peaks within a day for 71% of the events. In contrast, HSSs are more likely to have a 2-day delayed E3 peak than a 0-day delay. The varying time delay makes it difficult to produce a representative MEE precipitation climatology. Information about solar wind speed increases the prediction capabilities for both CMEs and HSSs. However, different speed thresholds need to be applied for the different structures to determine the probability of delay (see Figure 7).

The lower energies in the MEE fluxes are often associated directly with substorm injection. However, the high-energy tail (E3) needs additional energizing (Li et al., 2005; Tyssøy, Partamies, Babu, Smith-Johnsen, & Salice, 2021). Therefore, the physical mechanisms that link solar wind velocity to MEE precipitation are likely to be two-fold. Larger solar wind velocities can produce more intense ULF waves within the magnetosphere (Engebretson et al., 1998), providing radial diffusion and energizing the lower energy electrons (Barker et al., 2005; Schulz & Lanzerotti, 1974). Simultaneously, high solar wind speed is a good predictor of the substorm onset probability (Newell et al., 2016). Substorms will fuel VLF chorus waves, and the injected seed particles can be energized as they drift across the substorm-induced electric field on the night side.

Miyoshi et al. (2013) highlighted the importance of the southward (negative) IMF Bz component in accelerating the high-energy tail of the radiation belt population. Miyoshi et al. (2013) showed that HSS dominated by a southward IMF are associated with large flux enhancements of relativistic electrons. However, the role of Bz in our analysis is less evident due to the daily resolution wherein the average Bz is near zero, as it is likely to have both positive and negative values throughout the day. Nonetheless, as ϵ emphasizes negative Bz values, it will better represent the geoeffectiveness throughout a day which might be relevant in terms of peak flux levels and delay.

The timing of the E3 peaks is a product of both the acceleration processes and the lifetime of the respective electron enhancement. A short delay of zero or 1 day is typically linked to both high E1 values and high solar wind velocity based on Figure 6. This implies that an efficient acceleration process needs to be accompanied by an efficient loss process.

The lifetimes of MEE in the radiation belts depend on the energy, radial distance from Earth, and the level of geomagnetic activity. The lifetimes for 100 keV electrons at a radial distance of about four earth radii from the center of the Earth are approximately 3.6 days and 13 hr for quiet and active geomagnetic conditions, respectively (Orlova et al., 2016). Hence, a short lifetime is likely to follow the strength of the coupling functions, ϵ, which is closely linked to geomagnetic activity (Newell et al., 2016). This link is consistent with the average ϵ values for HSSs in Figure 6, whereas the average ϵ values for CMEs are a bit more ambiguous. The expected lifetime can, however, also be rapidly reduced in the case of magnetopause shadowing, where trapped particles over several radial distances are lost to the magnetopause. Magnetopause shadowing is a consequence of a sudden dynamic pressure increase in the solar wind, alongside convection-driven outward radial transport (D. L. Turner et al., 2012), both commonly associated with CME events.

4.3. Duration

Similar to the flux peaks, the duration of the MEE precipitation events will depend on a combination of the acceleration and loss mechanisms. Figure 8 shows longer flux enhancements of the high-energy tail compared to E1. CMEs have a higher probability for a short E1 duration (62% chance of lasting 1 day) compared to the other structures, which are more likely to be associated with durations of 2 days. Similarly, Longden et al. (2008) found that the mean electron flux intensity for 50–500 keV electrons during geomagnetic storms driven by CMEs typically return to pre-storm levels after 1–2 days from zero epoch (the first minimum in Dst), while CIR-driven

storms do not return to pre-storm values within their 3-day analysis after zero epoch. In our study, all structures, including CMEs, showed that the high-energy tail of the MEE precipitation had the highest probability of lasting 3–5 days, indicating the possibility of strong, long-lasting precipitation of E3 electrons in all structures, including CMEs. The shorter E1 duration associated with CMEs does not appear to suggest a shorter E3 duration. Note that the conclusion about the duration of the flux responses during CMEs is based on a few events but still seems to have a solid trend.

When examining the different solar wind parameters, it was concluded that they have no significant correlation with the duration of the flux responses and were, therefore, not included in this study. Tyssøy, Partamies, Babu, Smith-Johnsen, & Salice (2021) found the >292 keV precipitation fluxes to correlate well with the accumulated geomagnetic activity, assuming a lifetime of 9 days. Hence, the flux response and its duration are likely to be an accumulated effect of the preceding geomagnetic activity. This feature cannot be accounted for in the present analysis focusing on isolated events.

Moreover, Tyssøy et al. (2019) discussed the implication of underestimating the duration of the MEE precipitation events. It is, therefore, essential that an MEE precipitation parameterization applied in chemistry-climate models reflects the variability found in Figure 8.

5. Conclusion

Motivated by the demand to create a MEE parameterization that goes beyond the average picture, this study targets three key aspects needed to understand the high-energy tail of MEE precipitation: peak flux, delay, and duration. MEE precipitation is explored in the context of its solar wind drivers and the associated solar wind properties. The BLC measurements of the E1 (>43 keV) and E3 (>292 keV) MEE fluxes based on the MEPED detectors for the years 2004–2014 (one solar cycle) at 55°–75° CGM latitude are used. These energy channels reflect the general behavior of MEE and its high-energy tail. The key aspects are evaluated concerning the probability of a specific response.

The high occurrence frequency of HSSs compared to CMEs implies that they will strongly dominate the average event throughout a solar cycle in terms of flux strength, the delay of the high-energy tail, and the duration. In this study, HSSs constitute 73% of all 249 events selected in the 11 yr and are found to have lower flux responses than CME and combined events. Hence, the average event will best represent HSSs and underestimate stronger precipitation events.

There is a strong link between the peak fluxes in E1 and E3, with a correlation of 0.89. Information on the delay is needed to utilize their temporal relationship in a model. Moreover, higher correlations can be achieved when considering the respective solar wind driver. ϵ is a good parameter to use if the solar wind structure is unknown as the relation between ϵ and the E3 peak is the same for CMEs and HSSs.

E3 peaks 0–3 days after E1 peaks. The highest probability of ∼42% occurs for a 1-day delay, independent of solar wind structure. CMEs and HSS + CMEs have higher probabilities for faster E3 responses (>70% for a zero-one-day delay) compared to the other structures. Considering solar wind speed will increase the capability of predicting the delay for both CMEs and HSSs. Different speed thresholds for the different structures need to be applied.

All structures are associated with longer flux enhancements of the high-energy tail compared to E1. The duration of the E1 response has the highest probability of lasting 1 day for CMEs, whereas there is a higher probability of durations of 2 days for other structures. Nevertheless, the duration of the E3 response has the highest probability of lasting 4 days for both CMEs and HSSs. None of the applied solar wind parameters correlated with the duration of the MEE events.

A future MEE precipitation parameterization should represent the variability on both daily and decadal scales more realistically, allowing a better description of the subsequent atmospheric and chemical impact. This could be achieved by implementing a stochastic MEE parameterization accounting for the range of possible flux responses, delay, and duration. This is particularly important to understand the impact of the high-energy tail of the MEE spectrum.

Data Availability Statement

The NOAA/POES MEPED data used in this study are available from the National Oceanic and Atmospheric Administration (https://www.ngdc.noaa.gov/stp/satellite/poes/dataaccess.html). The bounce loss cone fluxes used in this study are available at Zenodo via https://doi.org/10.5281/zenodo.6590387. Geomagnetic indices and solar wind parameters were obtained from NASA Omniweb at https://omniweb.gsfc.nasa.gov/form/dx1.html.

The authors gratefully acknowledge the SuperMAG collaborators (https://supermag.jhuapl.edu/info/?page=acknowledgement) where the epsilon (ϵ) parameter was downloaded.

Acknowledgments
The study is supported by the Norwegian Research Council (NRC) under contracts 223252 and 302040. HNT further acknowledges the Young CAS (Centre for Advanced Studies) fellow program. The authors thank the Space Weather Prediction Center (SWPC), NOAA for providing the MEPED data. IGR acknowledges support from the ACE mission.

References

Akasofu, S. I. (1981). Energy coupling between the solar wind and the magnetosphere. *Space Science Reviews*, *28*(2). https://doi.org/10.1007/BF00218810

Asikainen, T., & Ruopsa, M. (2016). Solar wind drivers of energetic electron precipitation. *Journal of Geophysical Research: Space Physics*, *121*(3), 2209–2225. https://doi.org/10.1002/2015JA022215

Babu, E. M., Tyssøy, H. N., Smith-Johnsen, C., Maliniemi, V., Salice, J. A., Millan, R. M., & Richardson, I. G. (2022). Determining latitudinal extent of energetic electron precipitation using MEPED on-board NOAA/POES. *Journal of Geophysical Research: Space Physics*, *127*(9). https://doi.org/10.1029/2022JA030489

Baldwin, M. P., & Dunkerton, T. J. (2001). Stratospheric harbingers of anomalous weather regimes. *Science*, *294*(5542), 581–584. https://doi.org/10.1126/science.1063315

Barker, A. B., Li, X., & Selesnick, R. S. (2005). Modeling the radiation belt electrons with radial diffusion driven by the solar wind. *Space Weather*, *3*(10). https://doi.org/10.1029/2004SW000118

Beharrell, M. J., Honary, F., Rodger, C. J., & Clilverd, M. A. (2015). Substorm-induced energetic electron precipitation: Morphology and prediction. *Journal of Geophysical Research: Space Physics*, *120*(4), 2993–3008. https://doi.org/10.1002/2014JA020632

Borovsky, J. E., & Denton, M. H. (2006). Differences between CME-driven storms and CIR-driven. *Journal of Geophysical Research: Space Physics*, *111*(A7), A07S08. https://doi.org/10.1029/2005JA011447

Damiani, A., Funke, B., López-Puertas, M., Santee, M. L., Cordero, R. R., & Watanabe, S. (2016). Energetic particle precipitation: A major driver of the ozone budget in the Antarctic upper stratosphere. *Geophysical Research Letters*, *43*(7), 3554–3562. https://doi.org/10.1002/2016GL068279

Duderstadt, K. A., Huang, C.-L., Spence, H. E., Smith, S., Blake, J. B., Crew, A. B., et al. (2021). Estimating the impacts of radiation belt electrons on atmospheric chemistry using FIREBIRD II and Van Allen Probes observations. *Journal of Geophysical Research: Atmospheres*, *126*(7). https://doi.org/10.1029/2020JD033098

Engebretson, M., Glassmeier, K.-H., Stellmacher, M., Hughes, W. J., & Lühr, H. (1998). The dependence of high-latitude PcS wave power on solar wind velocity and on the phase of high-speed solar wind streams. *Journal of Geophysical Research: Space Physics*, *103*(A11), 26271–26283. https://doi.org/10.1029/97JA03143

Evans, D. S., & Greer, M. S. (2004). Polar orbiting environmental satellite space environment monitor - 2: Instrument descriptions and archive data documentation. NOAA Technical Memorandum version 1.4.

Funke, B., Baumgaertner, A., Calisto, M., Egorova, T., Jackman, C. H., Kieser, J., et al. (2011). Composition changes after the "Halloween" solar proton event: The High Energy Particle Precipitation in the Atmosphere (HEPPA) model versus MIPAS data intercomparison study. *Atmospheric Chemistry and Physics*, *11*(17), 9089–9139. https://doi.org/10.5194/acp-11-9089-2011

Gjerloev, J. W. (2012). The SuperMAG data processing technique. *Journal of Geophysical Research*, *117*(A9). https://doi.org/10.1029/2012JA017683

Hendrickx, K., Megner, L., Gumbel, J., Siskind, D. E., Orsolini, Y. J., Tyssøy, H. N., & Hervig, M. (2015). Observation of 27 days solar cycles in the production and mesospheric descent of EPP-produced NO. *Journal of Geophysical Research: Atmospheres*, *120*(10), 8978–8988. https://doi.org/10.1002/2015JA021441

Horne, R. B., Thorne, R. M., Glauert, S. A., Albert, J. M., Meredith, N. P., & Anderson, R. R. (2005). Timescale for radiation belt electron acceleration by whistler mode chorus waves. *Journal of Geophysical Research*, *110*(A3), A03225. https://doi.org/10.1029/2004JA010811

Jackman, C. H., DeLand, M. T., Labow, G. J., Fleming, E. L., Weisenstein, D. K., Ko, M. K. W., & Russell, J. M. (2005). Neutral atmospheric influences of the solar proton events in October–November 2003. *Journal of Geophysical Research*, *110*(A9). https://doi.org/10.1029/2004ja010888

Kataoka, R., & Miyoshi, Y. (2006). Flux enhancement of radiation belt electrons during geomagnetic storms driven by coronal mass ejections and corotating interaction regions. *Space Weather*, *4*(9). https://doi.org/10.1029/2005SW000211

Kennel, C. F., & Petschek, H. E. (1966). Limit on stably trapped particle fluxes. *Geophysical Research*, *71*, 1–28. https://doi.org/10.1029/JZ071i001p00001

Kidston, J., Scaife, A. A., Hardiman, S. C., Mitchell, D. M., Butchart, N., Baldwin, M. P., & Gray, L. J. (2015). Stratospheric influence on tropospheric jet streams, storm tracks, and surface weather. *Nature Geoscience*, *8*(6), 433–440. https://doi.org/10.1038/ngeo2424

Kilpua, E. K. J., Balogh, A., von Steiger, R., & Liu, Y. D. (2017). Geoeffective properties of solar transients and stream interaction regions. *Space Science Reviews*, *212*(3–4), 1271–1314. https://doi.org/10.1007/s11214-017-0411-3

Kilpua, E. K. J., Koskinen, H. E. J., & Pulkkinen, T. I. (2017). Coronal mass ejections and their sheath regions in interplanetary space. *Living Reviews in Solar Physics*, *14*(1), 5. https://doi.org/10.1007/s41116-017-0009-6

Koskinen, H. E. J., & Tanskanen, E. I. (2002). Magnetospheric energy budget and the epsilon parameter. *Journal of Geophysical Research: Space Physics*, *107*(A11), 1415. https://doi.org/10.1029/2002JA009283

Li, X., Baker, D. N., Temerin, M., Reeves, G., Friedel, R., & Shen, C. (2005). Energetic electrons, 50 keV to 6 MeV, at geosynchronous orbit: Their responses to solar wind variations. *Space Weather*, *3*(4). https://doi.org/10.1029/2004SW000105

Longden, N., Denton, M. H., & Honary, F. (2008). Particle precipitation during ICME-driven and CIR-driven geomagnetic storms. *Journal of Geophysical Research*, *113*(A6). https://doi.org/10.1029/2007JA012752

Maliniemi, V., Asikainen, T., & Mursula, K. (2016). Effect of geomagnetic activity on the northern annular mode: QBO dependence and the Holton-Tan relationship. *Journal of Geophysical Research: Atmospheres*, *121*(17), 10043–10055. https://doi.org/10.1002/2015JD024460

Maliniemi, V., Nesse Tyssøy, H., Smith-Johnsen, C., Arsenovic, P., & Marsh, D. R. (2021). Effects of enhanced downwelling of NO_x on Antarctic upper-stratospheric ozone in the 21st century. *Atmospheric Chemistry and Physics*, *21*(14), 11041–11052. https://doi.org/10.5194/acp-21-11041-2021

Marsh, D., Solomon, S., & Reynolds, A. (2004). Empirical model of nitric oxide in the lower thermosphere. *Journal of Geophysical Research*, *109*(A7), A07301. https://doi.org/10.1029/2003ja010199

Matthes, K., Funke, B., Andersson, M. E., Barnard, L., Beer, J., Charbonneau, P., et al. (2017). Solar forcing for CMIP6. *Geoscientific Model Development*, *10*(6), 2247–2302. https://doi.org/10.5194/gmd-10-2247-2017

Millan, R. M., & Thorne, R. M. (2007). Review of radiation belt relativistic electron losses. *Journal of Atmospheric and Solar-Terrestrial Physics*, *69*(3), 362–377. https://doi.org/10.1016/j.jastp.2006.06.019

Mironova, I. A., Artamonov, A. A., Bazilevskaya, G. A., Rozanov, E. V., Kovaltsov, G. A., Makhmutov, V. S., et al. (2019). Ionization of the polar atmosphere by energetic electron precipitation retrieved from balloon measurements. *Geophysical Research Letters*, *46*(2), 990–996. https://doi.org/10.1029/2018GL079421

Miyoshi, Y., Kataoka, R., Kasahara, Y., Kumamoto, A., Nagai, T., & Thomsen, M. F. (2013). High-speed solar wind with southward interplanetary magnetic field causes relativistic electron flux enhancement of the outer radiation belt via enhanced condition of whistler waves. *Geophysical Research Letters*, *40*(17), 4520–4525. https://doi.org/10.1002/grl.50916

Newell, P., Liou, K., Gjerloev, J., Sotirelis, T., Wing, S., & Mitchell, E. (2016). Substorm probabilities are best predicted from solar wind speed. *Journal of Atmospheric and Solar-Terrestrial Physics*, *146*, 28–37. https://doi.org/10.1016/j.jastp.2016.04.019

Ødegaard, L.-K. G., Tyssøy, H. N., Søraas, F., Stadsnes, J., & Sandanger, M. I. (2017). Energetic electron precipitation in weak to moderate corotating interaction region driven storms. *Journal of Geophysical Research: Space Physics*, *122*(3), 2900–2921. https://doi.org/10.1002/2016JA023096

Orlova, K., Shprits, Y., & Spasojevic, M. (2016). New global loss model of energetic and relativistic electrons based on Van Allen Probes measurements. *Journal of Geophysical Research: Space Physics*, *121*(2), 1308–1314. https://doi.org/10.1002/2015JA021878

Østgaard, N., Vondrak, R. R., Gjerloev, J. W., & Germany, G. (2002). A relation between the energy deposition by electron precipitation and geomagnetic indices during substorms. *Journal of Geophysical Research*, *107*(A9), 1246. https://doi.org/10.1029/2001JA002003

Partamies, N., Tesema, F., Bland, E., Heino, E., Nesse Tyssøy, H., & Kallelid, E. (2021). Electron precipitation characteristics during isolated, compound, and multi-night substorm events. *Annales Geophysicae*, *39*(1), 69–83. https://doi.org/10.5194/angeo-39-69-2021

Pettit, J., Randall, C., Peck, E., Marsh, D., van de Kamp, M., Fang, X., et al. (2019). Atmospheric effects of >30 keV energetic electron precipitation in the Southern Hemisphere winter during 2003. *Journal of Geophysical Research: Space Physics*, *124*(10), 8138–8153. https://doi.org/10.1029/2019JA026868

Richardson, I. G. (2018). Solar wind stream interaction regions throughout the heliosphere. *Living Reviews in Solar Physics*, *15*(1), 1. https://doi.org/10.1007/s41116-017-0011-z

Richardson, I. G., & Cane, H. V. (2012). Near-Earth solar wind flows and related geomagnetic activity during more than four solar cycles (1963–2011). *Journal of Space Weather and Space Climate*, *2*, A02. https://doi.org/10.1051/swsc/2012003

Rodger, C., Clilverd, M. A., Green, J. C., & Lam, M. M. (2010). Use of POES SEM-2 observations to examine radiation belt dynamics and energetic electron precipitation into the atmosphere. *Journal of Geophysical Research*, *115*(A4). https://doi.org/10.1029/2008JA014023

Schulz, M., & Lanzerotti, L. J. (1974). *Particle diffusion in the radiation belts*. Springer.

Seppälä, A., Randall, C. E., Clilverd, M. A., Rozanov, E., & Rodger, C. J. (2016). Geomagnetic activity and polar surface air temperature variability. *Journal of Geophysical Research*, *114*(A10). https://doi.org/10.1029/2008JA014029

Sinnhuber, M., Kazeminejad, S., & Wissing, J. M. (2011). Interannual variation of NO_y from the lower thermosphere to the upper stratosphere in the years 1991–2005. *Journal of Geophysical Research*, *116*(A2). https://doi.org/10.1029/2010ja015825

Sinnhuber, M., Nesse Tyssøy, H., Asikainen, T., Bender, S., Funke, B., Hendrickx, K., et al. (2022). Heppa III intercomparison experiment on electron precipitation impacts: 2. Model-measurement intercomparison of nitric oxide (NO) during a geomagnetic storm in April 2010. *Journal of Geophysical Research: Space Physics*, *127*(1). https://doi.org/10.1029/2021JA029466

Smith-Johnsen, C., Tyssøy, H. N., Hendrickx, K., Orsolini, Y., Kumar, G. K., Ødegaard, L.-K. G., et al. (2017). Direct and indirect electron precipitation effect on nitric oxide in the polar middle atmosphere, using a full-range energy spectrum. *Journal of Geophysical Research: Space Physics*, *122*(8), 8679–8693. https://doi.org/10.1002/2017JA024364

Solomon, S., Crutzen, P. J., & Roble, R. G. (1982). Photochemical coupling between the thermosphere and the lower atmosphere: 1. Odd nitrogen from 50 to 120 km. *Journal of Geophysical Research*, *87*(C9), 7206–7220. https://doi.org/10.1029/JC087iC09p07206

Theodoridis, G. C., & Paolini, F. R. (1967). Pitch angle diffusion of relativistic outer belt electrons. *Annales Geophysicae*, *23*, 375–381.

Turner, D. L., Shprits, Y., Hartinger, M., & Angelopoulos, V. (2012). Explaining sudden losses of outer radiation belt electrons during geomagnetic storms. *Nature Physics*, *8*(3), 208–212. https://doi.org/10.1038/nphys2185

Turner, N. E., Cramer, W. D., Earles, S. K., & Emery, A. B. (2009). Geoefficiency and energy partitioning in CIR-driven and CME-driven storms. *Journal of Atmospheric and Solar-Terrestrial Physics*, *71*(10–11), 1023–1031. https://doi.org/10.1016/j.jastp.2009.02.005

Turunen, E., Verronen, P. T., Seppälä, A., Rodger, C. J., Clilverd, M. A., Tamminen, J., et al. (2009). Impact of different energies of precipitating particles on NO_x generation in the middle and upper atmosphere during geomagnetic storms. *Journal of Atmospheric and Solar-Terrestrial Physics*, *71*(10–11), 1176–1189. https://doi.org/10.1016/j.jastp.2008.07.005

Tyssøy, H. N., Haderlein, A., Sandanger, M. I., & Stadsnes, J. (2019). Intercomparison of the POES/MEPED loss cone electron fluxes with the CMIP6 parametrization. *Journal of Geophysical Research: Space Physics*, *124*(1), 628–642. https://doi.org/10.1029/2018JA025745

Tyssøy, H. N., Partamies, N., Babu, E. M., Smith-Johnsen, C., & Salice, J. A. (2021). The predictive capabilities of the auroral electrojet index for medium energy electron precipitation. *Frontiers in Astronomy and Space Sciences*, *8*. https://doi.org/10.3389/fspas.2021.714146

Tyssøy, H. N., Sandanger, M. I., Ødegaard, L. G., Stadsnes, J., Aasnes, A., & Zawedde, A. E. (2016). Energetic electron precipitation into the middle atmosphere—Constructing the loss cone fluxes from MEPED POES. *Journal of Geophysical Research: Space Physics*, *121*(6), 5693–5707. https://doi.org/10.1002/2016JA022752

Tyssøy, H. N., Sinnhuber, M., Asikainen, T., Bender, S., Clilverd, M. A., Funke, B., et al. (2021). HEPPA III intercomparison experiment on electron precipitation impacts: 1. Estimated ionization rates during a geomagnetic active period in April 2010. *Journal of Geophysical Research: Space Physics*, *127*. https://doi.org/10.1029/2021JA029128

Tyssøy, H. N., & Stadsnes, J. (2015). Cutoff latitude variation during solar proton events: Causes and consequences. *Journal of Geophysical Research: Space Physics*, *120*(1), 553–563. https://doi.org/10.1002/2014JA020508

Tyssøy, H. N., Stadsnes, J., Søraas, F., & Sørbø, M. (2013). Variations in cutoff latitude during the January 2012 solar proton event and implication for the distribution of particle energy deposition. *Geophysical Research Letters*, *40*(16), 4149–4153. https://doi.org/10.1002/grl.50815

van de Kamp, M., Rodger, C. J., Seppälä, A., Clilverd, M. A., & Verronen, P. T. (2018). An updated model providing long-term data sets of energetic electron precipitation, including zonal dependence. *Journal of Geophysical Research: Atmospheres*, *123*(17), 9891–9915. https://doi.org/10.1029/2017JD028253

van de Kamp, M., Seppälä, A., Clilverd, M. A., Rodger, C. J., Verronen, P. T., & Whittaker, I. C. (2016). A model providing long-term data sets of energetic electron precipitation during geomagnetic storms. *Journal of Geophysical Research: Atmospheres*, *121*(20), 12520–12540. https://doi.org/10.1002/2015JD024212

Verronen, P. T., & Lehmann, R. (2013). Analysis and parameterization of ionic reactions affecting middle atmospheric HO_x and NO_y during solar proton events. *Annales Geophysicae*, *31*(5), 909–956. https://doi.org/10.5194/angeo-31-909-2013

Verronen, P. T., Seppälä, A., Kyrölä, E., Tamminen, J., Pickett, H. M., & Turunen, E. (2006). Production of odd hydrogen in the mesosphere during the January 2005 solar proton event. *Geophysical Research Letters*, *33*(24), L24811. https://doi.org/10.1029/2006GL028115

(WCRP), W. C. R. P. (2011). WCRP Coupled Model Intercomparison Project (CMIP). Retrieved from https://www.wcrp-climate.org/wgcm-cmip

Yando, K., Millan, R. M., Green, J. C., & Evans, D. S. (2011). A Monte Carlo simulation of the NOAA POES medium energy proton and electron detector instrument. *Journal of Geophysical Research: Space Physics*, *116*(A10). https://doi.org/10.1029/2011JA016671

Zawedde, A. E., Tyssøy, H. N., Stadsnes, J., & Sandanger, M. I. (2018). The impact of energetic particle precipitation on mesospheric OH—Variability of the sources and the background atmosphere. *Journal of Geophysical Research: Space Physics*, *123*(7), 5764–5789. https://doi.org/10.1029/2017JA025038

Zhang, J., Richardson, I. G., Webb, D. F., Gopalswamy, N., Huttunen, E., Kasper, J. C., et al. (2007). Solar and interplanetary sources of major geomagnetic storms (Dst ≤ −100 nT) during 1996–2005. *Journal of Geophysical Research*, *112*(A10). https://doi.org/10.1029/2007JA012321

Zhang, Y., & Paxton, L. (2008). An empirical *Kp*-dependent global auroral model based on TIMED/GUVI FUV data. *Journal of Atmospheric and Solar-Terrestrial Physics*, *70*(8–9), 1231–1242. https://doi.org/10.1016/j.jastp.2008.03.008

Zurbuchen, T. H., & Richardson, I. G. (2006). In-situ solar wind and magnetic field signatures of interplanetary coronal mass ejections. *Space Science Reviews*, *123*(1–3), 31–43. https://doi.org/10.1007/s11214-006-9010-4

Appendix A

Appendix

Table A.1: Day of Year (DOY) with ambiguous boundaries following the slot region filling events in the southern hemisphere.

2004	2005	2006	2007	2008	2010	2011	2012	2013	2014
1:37	1:32	27	2:6	7	95:96	46	15	146:159	71
42:49	38:41	78:81	18	33	99:105	61	59	166	230
60:62	50:54	97:114	30:31	61	124:127	78	71:80	170	244
70:81	57	118	46	70:76	151:155	156	117:120	181:201	295:298
88:90	65:74	124:129	113	87:90	216:219	159	145	228	301
94:103	78	132:133	120:121	99:100		190	158	240	343:344
115	96:110	158:161	147:149	115		219:222	164	278:281	357:358
122	120:123	176	219	120		244	169	288	363
128:129	130:180	205	277	123:125		271:274	184:186		
133:136	190:229	209	323	127		299:304	193:197		
153	238:270	232:240	327:329	133			200:203		
167	281:283	247		218			233		
191	308:311	261:262					251		
199:200	346	267					277:280		
205:227	362	342:362					284:286		
230:236							291:294		
245:252							329:330		
258:268									
278									
288:290									
295									
299									
313:343									
348:353									
356:358									
364:366									

Table A.2: Day of Year (DOY) with ambiguous boundaries following the slot region filling events in the northern hemisphere

2004	2005	2006	2007	2010	2011	2012	2013
1-31	8-25	95-113	29	95-105	76	68-80	145-160
42-48	38-43	127-128	143-149	150-156	149-153	114-122	180-202
70-77	49-51	158-161	184	215-219	156-158	164-166	
95-104	66-73	208-209	192		218-221	169-173	
167	95-110	232-236	344		252-260	191-205	
199	128-179	247-248			298-300	275-277	
200	191-229	334-336				282-295	
205-226	237-264	346-359					
259-268							
314-320							

Graphic design: Communication Division, UiB / Print: Skipnes Kommunikasjon AS

uib.no

ISBN: 9788230857908 (print)
9788230858158 (PDF)